SIMULATION OF UTERUS ACTIVE CONTRACTION AND FETUS DELIVERY IN LS-DYNA

By

Ru Tao

A DISSERTATION

Submitted to
Michigan State University
in partial fulfillment of the requirements
for the degree of

Mechanical Engineering – Doctor of Philosophy

2024

ABSTRACT

Vaginal childbirth, also known as delivery or labor, is the ending phase of pregnancy where one or more fetuses pass through the birth canal from the uterus, which is a biomechanical process. However, the risky process can cause significant injuries to both the fetus and the mother, such as brachial plexus injury, pelvic floor disorders, or even death. Due to technical and ethical reasons, experiments are difficult to conduct on laboring women and their fetuses. The use of computer modeling has become a very promising and rapidly growing way to perform research to improve our knowledge of the biomechanical processes of labor and delivery. The developed simulation models in this field have either focused on the uterine active contraction or the pelvic floor muscles, individually. In addition, there are many limitations existing in the current uterus models.

The goal of the project is to develop an integrated model system including the uterus, the fetus, the pelvic bones, and the pelvic muscle floor, which will allow advanced simulation and investigation within the field of biomechanics of fetal delivery. For the first step, a computational model in LS-DYNA simulating the active contraction behaviors of muscle tissue was developed, where the muscle tissue was composed of active contractile fibers using the Hill material model and the passive portion using elastic and hyperelastic material models. The model was further validated with experimental results, which demonstrated the accuracy and reliability of the modeling methodology to describe a muscle’s active contraction and relaxation behaviors. Second, a simulation model of a whole uterus during the second stage of labor was developed, which included active contractile fibers and a passive muscle tissue wall. The effects of the fiber distribution on uterine contraction behaviors were investigated and the delivery of a fetus moving through the uterus due to the contraction was simulated. The developed uterus model included several important uterine mechanical properties, such as the propagation of the contraction wave, the anisotropy of the fiber distribution, contraction intensity variation within the uterus, and the pushing effect on the fetus. Finally, an integrated model system of labor was established by incorporating the pelvic structures with the uterus and fetus models. The model system successfully delivered the fetus from the uterus and through the birth canal. The simulation results were validated based on available data and clinically observed phenomena, such as stress distribution within the uterus, values of Von Mises stress and principal stress of the pelvic floor muscles, rotation and movement of the fetus. Overall, a Finite Element Method model system simulating the labor process was developed in LS-DYNA, which will be used to investigate

disorders related to labor, such as neonatal brachial plexus injury and maternal pelvic floor muscle injuries.

ACKNOWLEDGEMENTS

First and foremost, I would like to express my gratitude to my supervisor, Prof. Michele Grimm. Academically, she supported and encouraged me a lot during the past few years, which brought me much confidence to overcome the difficulties of the courses and research. She always gave me the best advice and help when it was hard for me to make progress in research. She also gave me much freedom to conduct the research, for which I am grateful. She is always patient, serious, and strict with my writing so that my writing skills can be improved. Her great enthusiasm and motivation for researching to solve actual clinical problems using engineering methodologies with the purpose to benefit human health also inspired me a lot. In life, Dr. Michele is a great person. She is kind, modest, helpful, nice, and respectful to everyone. She takes care of me and other group members in many aspects. I am very fortunate to be a student of Dr. Michele.

I would like to thank my committee members, Dr. Bush, Dr. Roccabianca, and Dr. Arora for their great advice and support to my research project. Dr. Bush is very friendly and helpful. She always took care of us when we were attending conferences outside of Michigan. Dr. Roccabianca is also the instructor of my Linear Elasticity course. She made the derivation of equations for the mechanics of solids much easier to understand and learn. She was also very helpful and patient with questions from students.

I also want to thank my lab group members, Sheng Chen, Liz Pollack, Sarah Trapp, and Lily Craigmalich for their help all the time. Sheng Chen is like a big brother to me. He helped me a lot with the Madymo, Hypermesh, and other technique problems with FEM analysis. Sarah is always very helpful to me in life. Thank you, Sheng and Lily, for sharing the geometrical models of the pelvis structures and the fetus.

Finally, I want to thank my family, father Bangao Tao, mother Xiaohuan Zhang, and sister Dandan Tao. No words can express my gratitude to my great parents. I grew up with my sister and she helped me in many aspects. I also want to thank my best friends, Suwan Li and Jian Yang. They showed great friendship, love, and encouragement to me in my hard time. In the end, I am sincerely grateful to all the people who helped me in my past life's journey.

TABLE OF CONTENTS

CHAPTER 1: Introduction

1.1 Definition of Three Stages of a Labor

A normal labor or fetus delivery process involves three stages. The first stage (Fig 1.1) usually starts from the point of persistent uterine contractions -- which become more regular, stronger, and more frequent over time -- and proceeds to the point of full cervix dilation -- which is about 10 cm in diameter [1]. The typical symptom of the beginning of the first stage is crampy abdominal or back pain that occurs every 10 to 30 minutes and lasts around 30 seconds [2]. This stage can be further divided into the latent phase and the active phase [3]. The latent phase is the early part of the first stage, where the uterus contracts to make the cervix softer and thinner and opens up the cervix to 3 – 4 cm [3]. The active phase is defined as the period from the establishment of regular contractions by the uterus to the end of the first stage [4]. The second stage spans from the point of complete cervix dilation to full delivery of the fetus, when both the abdominal force generated by maternal pushing and the uterus' active contraction contribute to the movement of the fetus through the birth canal (Fig 1.1) [1]. The third stage is the delivery of placenta [1].

The second stage is the most stressful part of the labor process. A prolonged second stage of labor, which is longer than 2 or 3 hours, can lead to many complications -- such as shoulder dystocia, increased rate of maternal and fetal morbidities, operative vaginal delivery, postpartum hemorrhage, episiotomy, fetal skull fracture, facial nerve palsy, and brachial plexus injury [5]. The maternal positions during the second stage of labor play a vital role in managing such a process, and certain positions have been demonstrated to promote maternal and neonatal outcomes. The common maternal positions include lithotomy position, supine position, lateral position, sitting position, kneeling position, and squatting position [6]. Among these positions, the squatting position and sitting position may be associated with perineal trauma and great blood loss, while some have suggested that the lithotomy position and supine position be avoided during the second stage of labor due to the related increased risks of longer labor and severe perineal trauma [6] In contrast, the lateral position has been demonstrated to improve labor outcomes and reduce the rate of complications [6]. The second stage of labor is a complicated biomechanical process. Aside from the effect of the maternal positions, the fetal size and position, the pelvic structure and capacity, and the uterine contractility all affect the fetus delivery process significantly [7].

Computational modeling is a great tool to quantitatively investigate how each of the factors influences the fetus's movement through the birth canal to provide new insights or understandings of the childbirth process.

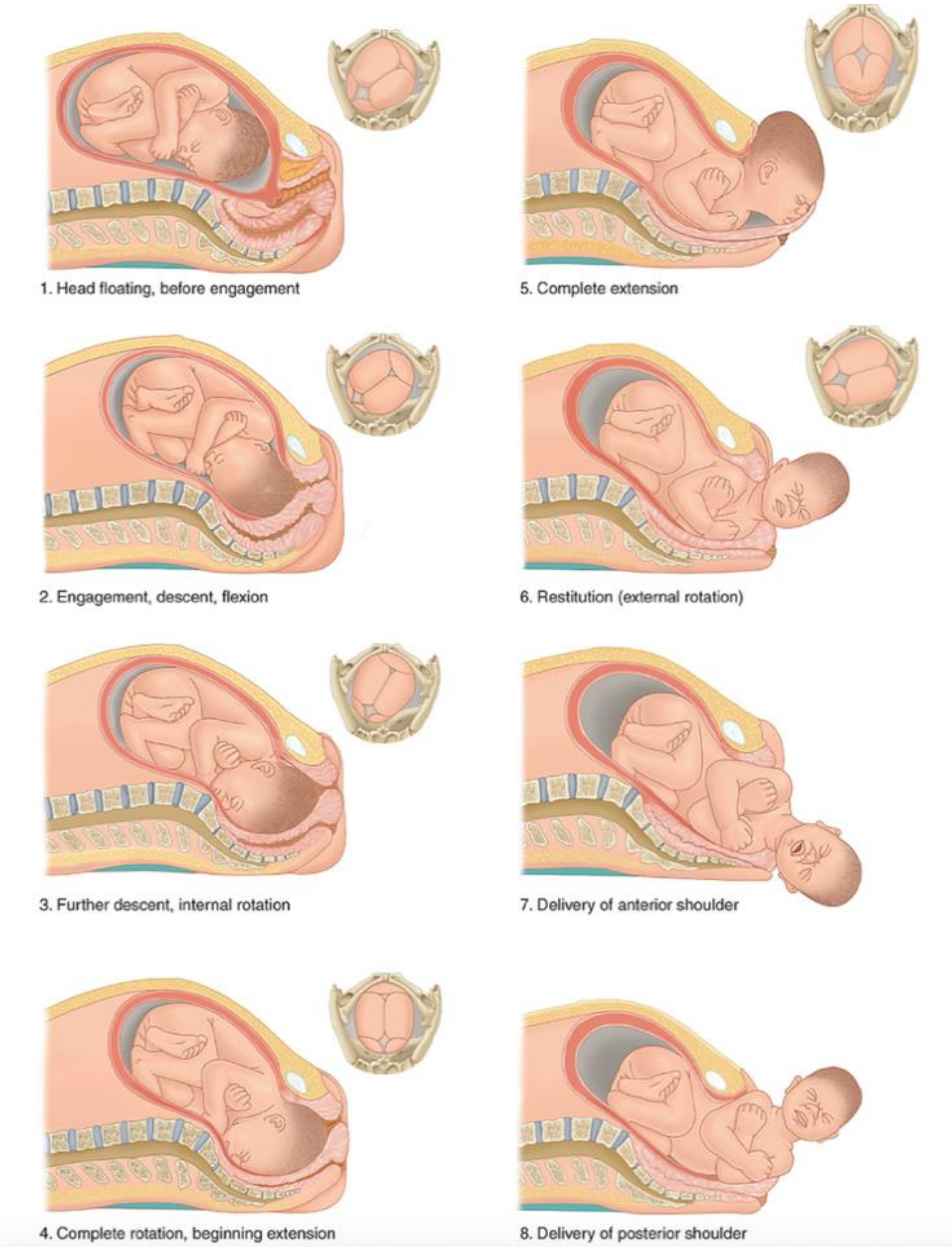

1. Head floating, before engagement

5. Complete extension

2. Engagement, descent, flexion

6. Restitution (external rotation)

3. Further descent, internal rotation

7. Delivery of anterior shoulder

4. Complete rotation, beginning extension

8. Delivery of posterior shoulder

Figure 1.1, Processes of the first and second stages of labor [1]. The first stage involves panels 1-4, while the second stage is represented by panels 5-8. This also depicts the cardinal movements of labor that occur as the infant interacts with the mother's pelvis.

1.2 The Uterus

The uterus is the major organ of the female reproductive system (Fig 1.2) [8]. The size of a human unpregnant uterus is about 7.5 cm long, 4.5 cm wide, and 2.5 cm thick [9]. The shape of the uterus is like an upside-down pear. However, the size and the shape of uterus change dramatically during pregnancy [3]. The position of the uterus is located between the bladder and rectouterine pouch. The lower end of the uterus is the cervix, which can be dilated greatly by uterine contractions during the fetus' delivery process. Inside the uterus is a cavity filled with fluid and surrounded by the uterine walls. The whole body of the uterus is called the corpus, and the top of the uterus is the fundus [9]. Between the cavity of the uterus and the vaginal canal is the cervical canal. During pregnancy, the size of the uterus will keep growing to accommodate itself to the growing fetus. At the end term of gestation, the human uterus is about 40-42 cm long, and 35-37 cm wide [3]. The total volume of the uterus can be on average 5 L, which is much bigger than that of the 10 mL size of the cavity in the non-pregnant state [10].

During the second stage of labor, the main function of the uterus is to contract and cause the fetus to move through the birth canal. Normal uterine activity is one of the most important factors for a successful labor. Abnormal or insufficient uterine contraction has been found to cause several labor difficulties and is believed to be the dominant reason for Cesarean section [11]. Therefore, it is always important to monitor uterine activity during labor, which can be helpful in solving clinical problems related to the labor. Various methods have been developed to monitor uterine activity, including maternal perception, manual palpation, external tocography, internal tocography, and uterine electromyography (EMG) [12]. Among these methods, internal tocography has been proposed as the best method due to its ability to not only provide objective information on uterine activity quantization but also obtain a good-quality trace in all patients. Parameters such as the duration of a contraction, contraction frequency, amplitude, uterine baseline tone, and relaxation time are commonly used to describe a contraction curve or shape. The abnormal labor process can be shown in the contraction shape. For example, the shortening of the relaxation time during uterine contractions was closely related to severe fetal asphyxia [12]. In another study, the ratio between the duration of returning from a contraction peak to the baseline and the duration of rising from the baseline to the contraction peak was recorded for 200 women during labor [13]. They found that the ratio was higher in the group that lacked labor progress, which demonstrated that the contraction shape of the uterus can be used to analyze and predict a labor’s progression.

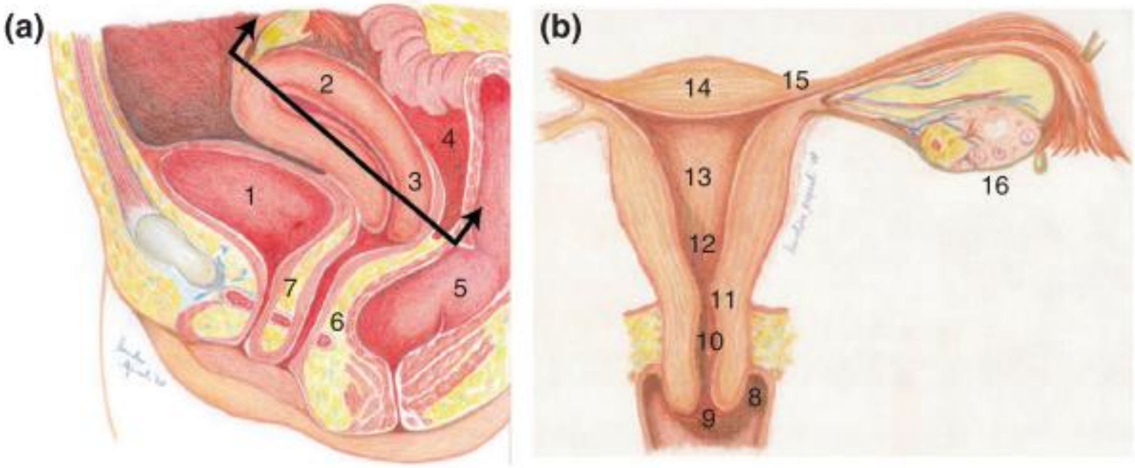

Figure 1.2, Uterine anatomy [8]. Side view (a): bladder (1), uterine body (corpus) (2), cervix (3), rectouterine pouch (4), rectum (5), rectovaginal septum (6), and vesicovaginal septum (7); and front view (b): formix vaginalis (8), external uterine os (9), cervical canal (10), internal uterine os (11), isthmus (12), body (13), and fundus (14) of the uterus, intramural segment of the uterine tube (15), and ovary (16).

1.2.1 Uterine Wall

The structure of the uterine wall was described by Myers [8] and consists of three different layers (Fig 1.3) [8]. The endometrium of the uterus is an inner mucosal layer composed of epithelial cells [8]. The middle layer, the thickest layer, of the uterus is the myometrium, which mainly consists of smooth muscle cells (SMC) (Fig 1.4a) [8]. Such SMCs are organized in different directions within fiber bundles, which provide the uterus’ contraction function [14]. A bundle is a cluster of SMCs having the same direction. The diameter of the cross-section of the bundle is about 300 μm [14]. Different bundles are connected to each other through a connective tissue sheath, which includes blood vessels, lymphatics, and nerves [15]. Many bundles together will form a fasciculus, which is 1-2 mm in diameter. Each fasciculus can be many centimeters long [15]. The fasciculus is then the structural element of the myometrium, contributing to the active contraction force generation in the uterus. The structure of the myometrium has been further studied by experimental techniques such as MRI [16,17]. It has been shown that there are three layers inside the myometrium: the stratum subvasculare, stratum vasculare, and stratum supravasculare [18]. In general, the fasciculus will be aligned in longitudinal, circumferential, and oblique directions inside the myometrium [17]. Clearer information about the 3D fiber direction and structure through the myometrium remains to be determined [19]. There is a small junction zone called the endometrium–myometrium interface (EMI) between the endometrium and the SMC layer [8]. The thin outside layer is the perimetrium, which consists of connective tissue [8].

The contraction of the fibers inside of the uterine wall contributes to the contraction of the whole uterus. The distribution of the fibers in the uterus significantly influences the mechanical behaviors of the uterus, and thus is a popular research field. The earliest studies can be traced back to the nineteenth century, in which the agreement point was that the longitudinal direction and circumferential direction were the two predominant directions inside of the uterine wall for both the non-pregnant and pregnant uterus [20,21]. With the advance of experimental techniques, more details of the fiber distribution were revealed. The fibers were found to be not perfectly parallel to the uterine wall surface but inclined with the wall, which means the fiber orientation are three-dimensional [19]. This is an important finding, because the existing simulation model in the literature that simulates the uterus's active contraction during the second stage of labor only considered the fibers in two-dimensions, with all fibers parallel to the muscle wall surface [22]. The accuracy of such a study is, therefore, in doubt. Another important finding is that both the fiber orientation and fiber content vary significantly in different regions of the uterus, which means the uterine fiber distribution showed strong anisotropic characteristics [23]. For example, the fiber content was higher in the fundus region than in the middle and lower part of the uterus, which, therefore, provides stronger contraction intensity in the fundus region [23]. In order to more accurately model the uterine active contraction and its effect on the fetus's movement through the birth canal during labor, it is important to take into account such anisotropy of the fiber distribution.

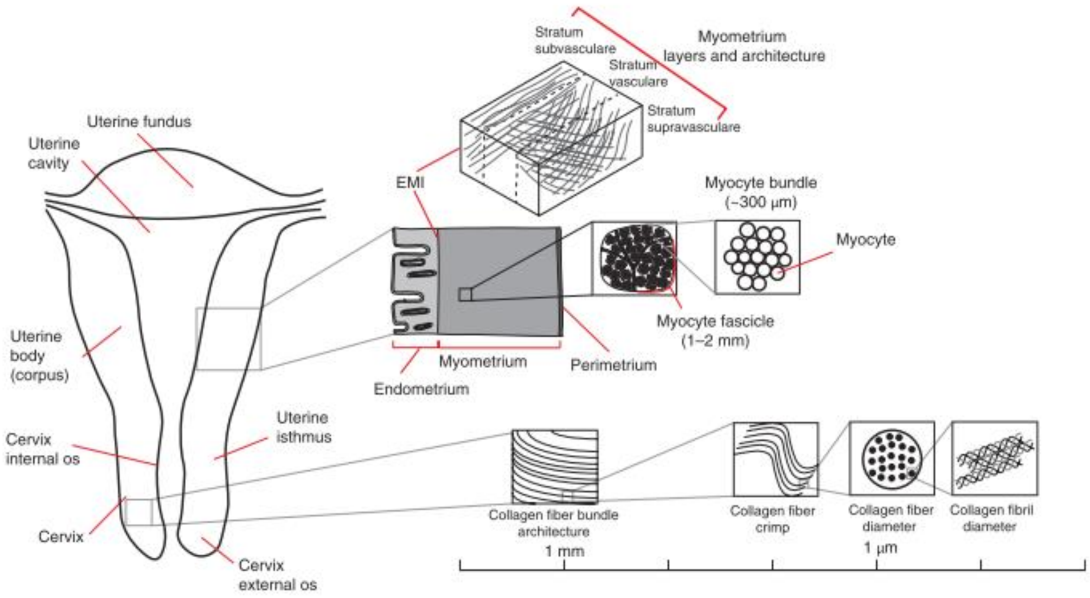

Figure 1.3, Structures of the uterus wall including perimetrium, myometrium, endometrium, and collagen fibers [8].

1.2.2 Uterine Smooth Muscle Cells

Smooth muscle cells are spindle-shaped structures, wide in the middle and thin in the ends, that can contract and relax [24]. The intermediate filaments, inside which actin filaments and myosin slide over each other (Fig 1.4b), cause the muscle fiber to contract (Fig 1.4a) [25]. Their contraction is involuntary, which means the contraction is not signaled by neurons in the head. The contractions are initiated by the spontaneous depolarization of the cell membrane, which leads to the influx of Ca^{2+} into the cell, while relaxation is typically caused by a reduction of the concentration of Ca^{2+} due to its removal from the cell [26]. Smooth muscle cell contraction can be influenced by many different factors, such as spontaneous electrical activity, chemical signals, or mechanical forces like stretch [26].

The contraction of the uterus is initiated by the contraction of the uterine smooth muscle cells. To understand the macro-scale contraction behaviors of the whole uterus, it is important to understand the mechanisms of contraction force generation at the cell level. Briefly, the current knowledge about the mechanisms for contraction of uterine smooth muscle cells is that entry of Ca^{2+} ions into the cell occurs due to the depolarization of the cell membrane. This increases the intracellular Ca^{2+} concentration, which leads to a chain of biochemical reactions, the formation of the cross-bridge between the actin and myosin filaments, sliding between these two filaments, and finally the cell contraction [27]. However, the middle biochemical chains or pathways for both contraction and relaxation inside of the uterine smooth muscle cells to generate an active stress are very complicated during pregnancy [28]. A few mathematical models have been developed to describe the contraction of the uterine smooth muscle cell. For instance, Charles *et al* modified the Hai-Murphy model, which has been widely applied to model smooth muscle cell contraction, by incorporating the cross-bridge position and contractile velocity to describe the specific uterine smooth muscle cell's contraction [29]. The model demonstrated 23% more accurate results than the Hai-Murphy model for isometric contractions, more accurate contraction behaviors in the initial stages, and the ability to predict nonisometric contraction as well. Both experimental research and computational models are still being used to improve the field's understanding of such cells' contraction.

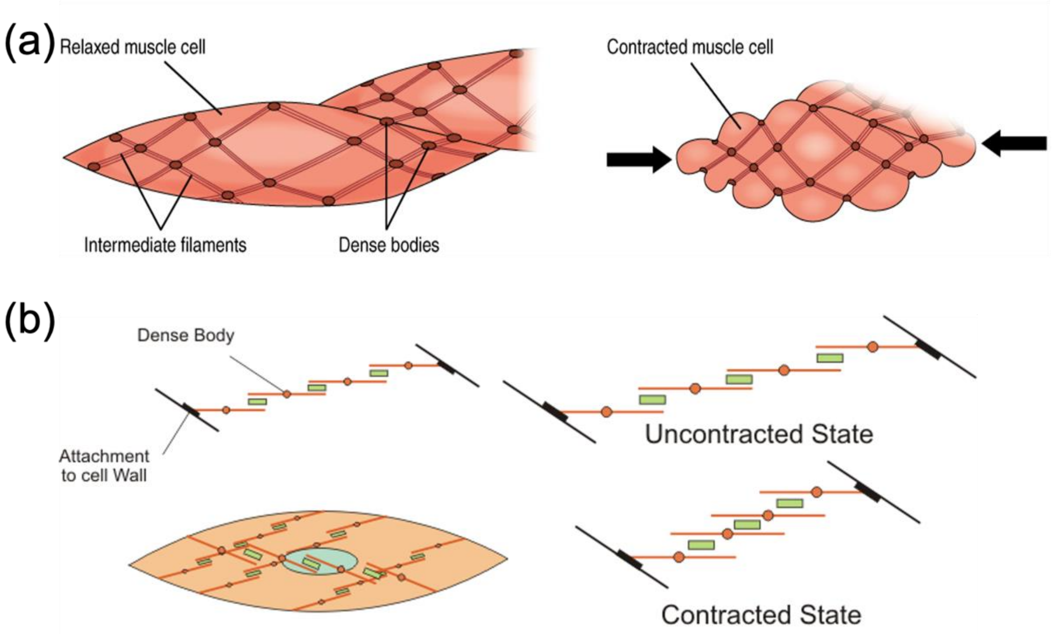

Figure 1.4, Uterus smooth muscle cell (a) and actin-myosin filaments (b) [25].

1.3 The Pelvis

The anatomical pelvis is commonly defined as the region that includes the bony pelvis (also called the pelvic girdle), the pelvis cavity (the area enclosed by the bony pelvis), and the pelvic floor [30]. The pelvis is in the lower part of the trunk, between the abdomen and thighs (Fig 1.5) [30]. The pelvic girdle (Fig 1.6) is posteriorly composed of the sacrum and the coccyx and laterally by the hip bones, which are further divided into the ilium, ischium, and pubis from back to front

[31]. The pelvic bones are attached firmly and are very rigid and strong [32]. The main function of the pelvic bones is to bear the body weight and transfer the weight to the lower skeleton [32].

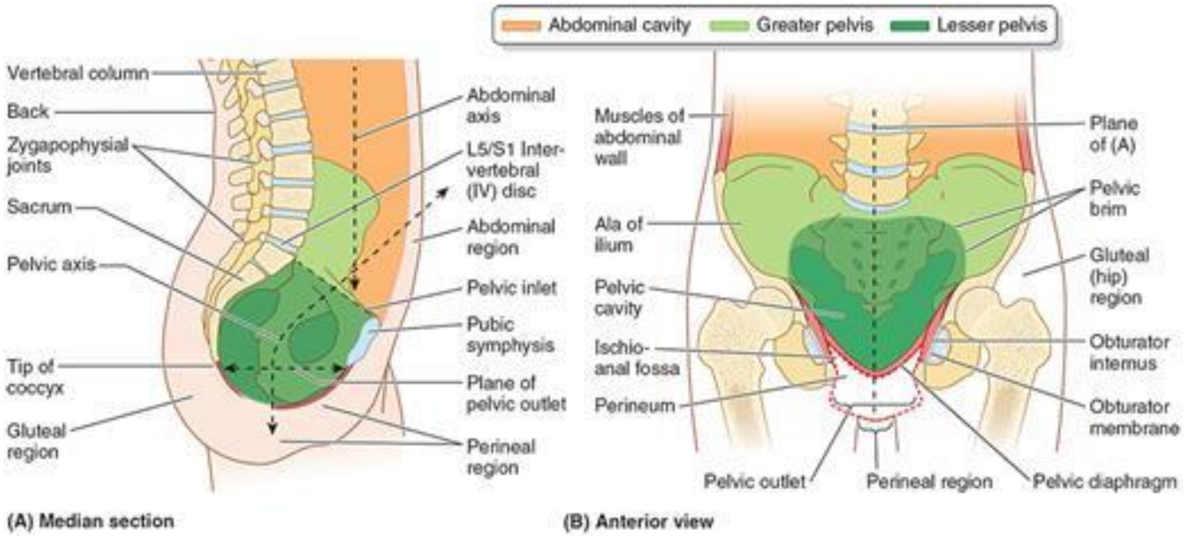

Figure 1.5, Position and structures of the pelvis [30].

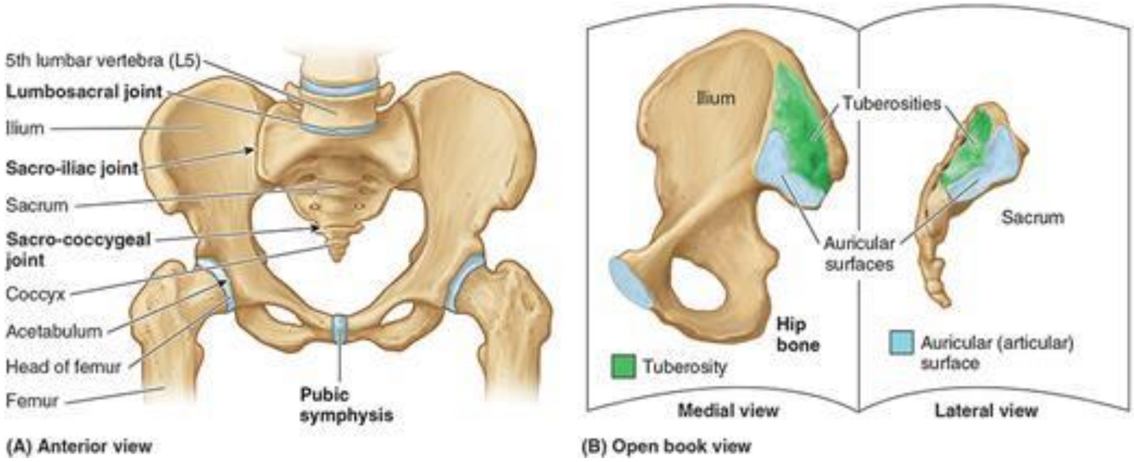

Figure 1.6, The pelvic girdle and the pelvic cavity from Anterior view [30].

The pelvic cavity (Fig 1.6) is the body cavity that is surrounded by the pelvic bones and contains the reproductive organs, the terminal parts of the urinary bladder, the ureters, blood vessels and nerves, and the rectum [31]. The pelvic cavity is further divided into the lesser part (below the pelvic brim) and the greater part (above the pelvic brim) (Fig 1.5) [30]. The curving shape of the walls of the cavity is an important factor for fetal passage through the pelvic canal [32].

The pelvic muscle floor (Fig 1.7), also known as the pelvic diaphragm, is composed of many muscles and connective tissues. The coccygeus and the levator ani are two of the most important components of the pelvic floor [33]. These arise between the ischial spine and the symphysis and cover the pelvic cavity. The coccygeus muscle is between the levator ani and the sacrospinous ligament in the pelvic floor, and it assists the levator ani and piriformis muscle to close the outlet of the pelvis and to support other pelvic components in women [20]. The levator ani is the main part of the pelvic floor, consisting of the iliococcygeus, the pubococcygeus, and the puborectalis [33]. The function of the levator ani is to support the abdominopelvic viscera and help to maintain urinary and fecal continence [32]. Also, it contracts actively during reactions such as vaginismus (spontaneous contraction of the vaginal muscles) and coughing [32].

The size and shape of the pelvic structures also play an important role in fetus delivery during the second stage of labor. The mismatch between the size of the pelvis and the size of the fetus can lead to the cephalopelvic disproportion (CPD) in labor [34]. The shape of the inlet of the pelvis is usually described as android (more triangular), gynaecoid (heart-shaped), platypelloid (oval with longer transverse diameter), and anthropoid (oval with longer anterior-posterior axis) [35]. The size of the inlet and outlet of the pelvic is described by the area or the circumference. In a study with 274 patients aiming to investigate the correlation of the pelvic dimension and fetus size to the risk of the cesarean section, the circumferences of the fetal head and the inlet and outlet of the pelvic were measured [36]. The mean dimension of the maternal pelvic inlet and outlet was about 401 mm and 360 mm, respectively, for the vaginal delivery group, and about 384 mm and 356 mm, respectively, for the cesarean section delivery group. The mean fetal head circumference was about 339 mm and 346 mm for vaginal deliveryies and cesarean section deliveries, respectively. The larger size of the pelvic structure and smaller size of the fetal head can make the fetus delivery process easier during the second stage of labor and thereby reduce the rate of the cesarean section. Another study measured the pelvic capacity in 50 pregnant women during the gestational weeks 20 to 32, in three birthing positions: kneeling squat, semi-lithotomy, and the supine [37]. They found that the pelvic capacity increased with the gestational week in all these three positions, and the supine position was beneficial in increasing the pelvic inlet size, while the semi-lithotomy and kneeling squat positions increased the mid- and outlet size.

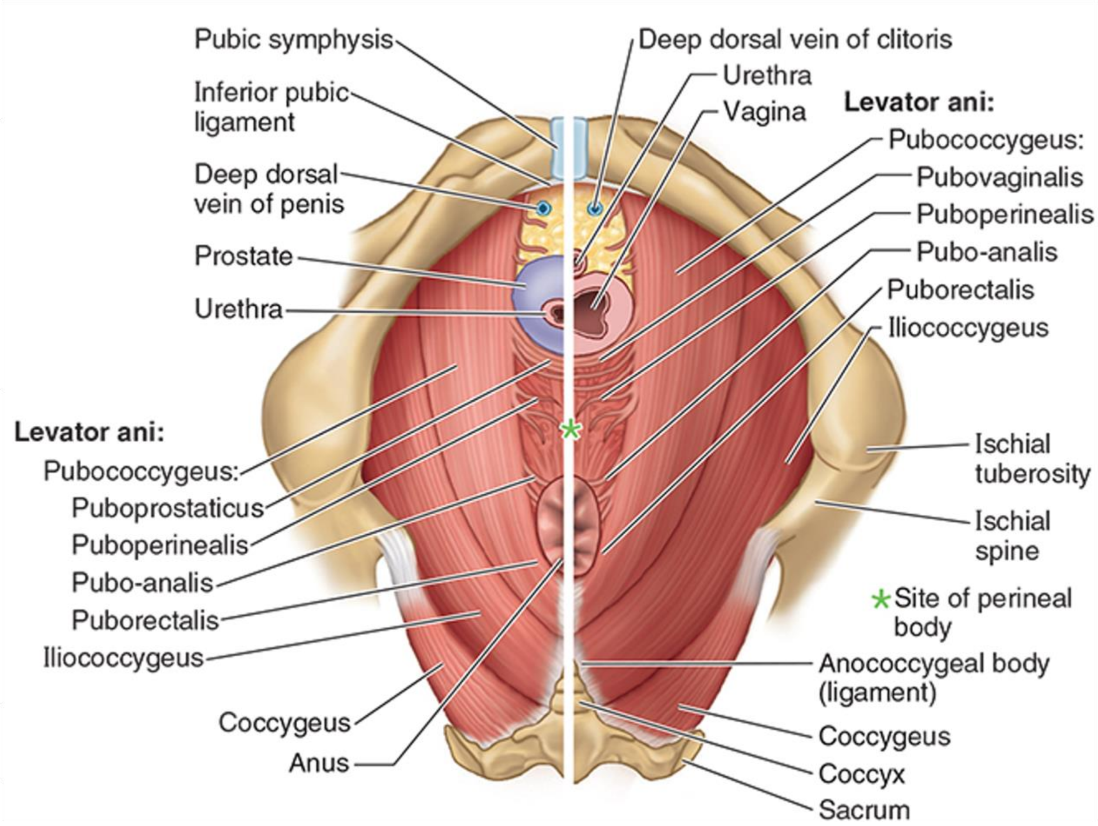

Figure 1.7, Pelvic muscle floor diaphragm [30].

1.4 The Forces Acting during Labor

The second stage of labor -- the delivery of the fetus through the mother’s body to the outside world -- is quite a biomechanical process. The successful movement of the fetus towards the outside of the birth canal from the maternal uterus is the win of the expulsive forces (uterine contraction and maternal pushing) by the mother and some help from the clinicians over the resistance forces caused by the interactions between the fetus and the biological structures in the birth canal. In contrast, an unsuccessful labor process is a failure of pushing efforts to overcome resistance factors, which subsequently results in a cesarean section delivery or even more serious outcomes, such as the morbidities to mothers and infants. Two of the most common injuries, neonatal brachial plexus injury and pelvic muscle disorder, occur during the second stage labor process and have been demonstrated to be closely associated with too-high stress or strain in the brachial plexus nerves or the pelvic floor muscles [38,39]. Therefore, it is important to figure out the most important forces during labor, including both the expulsive forces and the resistance forces, and how each of the forces affects the process. Briefly, during the passage of the fetus through the birth canal, the fetus undergoes two sets of opposite forces: the expulsive force caused by the maternal efforts and the resistance forces caused by the strong interaction between the pelvic muscle floor and the fetus' body. In 2021, Grimm published a review paper that summarized the forces experienced by the mother and fetus during the delivery process [40]. In the first stage of the labor, the expulsive forces include uterine active contraction and intrauterine pressure, while the resistance force is mainly the friction between the fetal head and the maternal cervix. In the second stage of the labor, there is one more expulsive force -- the abdominal pressure caused by the maternal pushing -- that contributes to the increase in the pressure inside of the uterus, while the resistance force is the friction between the fetus's body and the pelvic structures (bony pelvis and pelvis floor muscle) and the vagina canal. (Fig 1.8).

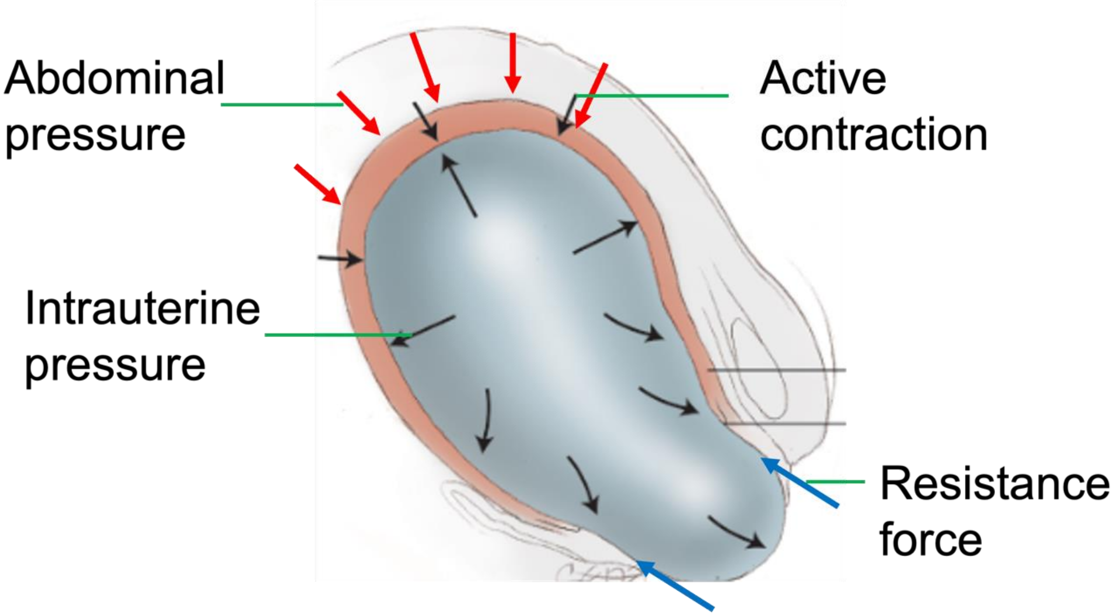

Figure 1.8, Forces acting in the second stage of a labor [41].

1.5 Overview of this Project

The labor or fetus delivery process is a very dangerous process. Approximately, twenty percent of labors are difficult or dysfunctional with an abnormally long delay in labor progression, called labor dystocia [42]. According to a one hospital's statistics in 2007, only fifty percent of 13,991 women progressed through spontaneous labor to the point of delivery, while the rest required Caesarean section, augmentation, or induction [41].

Labor dystocia can lead to a high risk of injuries to both the infant and the mother resulting from the stress, strain, and stretch of the biological tissues or anatomical structures of the fetus and the mother during the delivery process [43]. For the fetus, any part of the body – such as the intra-abdominal organs, spinal cord, head, peripheral nerves, and skeletal systems -- can be affected [44]. The common injuries include brachial plexus injury [45] and facial palsy [46]; as well as fractures, including clavicle, femur [47] and humerus fractures [48]. Regarding the mother, pelvic floor disorder caused by pelvic muscle floor damage is the most common injury due to the high stretch of the muscles that form the birth canal during fetus delivery [32,49,50]. Therefore, it is important to understand the mechanical process of labor and delivery so that mechanisms of injury can be more realistically investigated.

Computational modeling is a better tool to investigate the biomechanical processes of labor and delivery than experiments in this field for ethical reasons. Over the past few years, several models have been developed [49,51–56]. However, these studies either focused on uterine active contraction or the pelvic muscle floor, individually. Due to the separation of these components, both types of models are not biofidelic. For instance, without the pelvic muscle floor, there are no resistance forces for the uterus's active contraction models to work against. For the pelvic muscle floor models, due to the lack of the cyclic forces caused by uterine contraction and maternal pushing, the movement of the fetal head, which was set as a kinematic condition in the current studies, is also not realistic. As a result, the simulation results such as the stress and strain field and displacement are not accurate. In addition, there are still many limitations within the uterus active contraction models. These include: using boundary conditions to represent the contraction effect; not including a fetus model; simulating very small deformations; using a highly simplified geometry of the uterus; not simulating intrauterine pressure; and excluding many important uterine properties and responses, such as anisotropy of the fiber distribution, contraction wave propagation, and contraction intensity variation within the uterus. Therefore, it is important and necessary to improve the uterine active contraction model to better reflect the uterine mechanical behaviors, and then to put the uterus, the fetus, and the pelvic structures together to develop a more accurate and complete model for describing the mechanical behaviors of labor.

The first goal of our project is to model the active contraction behavior of the contractile fiber and 3D muscle tissue because they are the causes for the active contraction of the whole uterus. The second goal is to develop and validate a finite element model to simulate the active contraction behavior at the organ level that will be able to simulate many uterine mechanical behaviors. The target properties and behaviors include the contraction wave propagation, the fiber orientation and distribution anisotropy, and the pushing effect on the fetus. The final goal of the project is to develop an integrated model of the uterus, the fetus, the pelvic bones, and the pelvic muscle floor, which will allow advanced simulation and investigation within the field of biomechanics of fetal delivery.

CHAPTER 2: Simulation of Involuntary Muscle’s Active Contraction

2.1 Abstract

The macro-scale active contraction behavior of involuntary muscles, such as the uterine muscle wall, is vital to support the muscular organs’ functions. A 3D finite element model of generalized muscle tissue was established in LS-DYNA to simulate its active contraction behaviors. Truss elements with the Hill material model were used to represent the muscle’s active contractile fibers. Hexahedral elements were used to represent the muscle’s passive mechanical properties using two possible material models, elastic and hyperelastic. The simulation results showed that the muscle unit can contract and relax actively in a case where there were no externally applied loads. The muscle’s contraction capacity and speed were analyzed, and they were found to be significantly influenced by the maximum isometric stress (PIS) and the damping coefficient (DMP) in the Hill model, respectively. Finally, a finite element model of a strip of smooth muscle was created to compare with experimental results of tracheal smooth muscle’s active contraction and relaxation. The simulation results closely matched the experimental results. In conclusion, we demonstrated that the phenomenological three-element Hill constitutive model in LS-DYNA is well suited to the modeling of active contraction behavior for involuntary muscles. Based on this finding, it will now be possible to investigate the macro-scale biomechanics of involuntary muscular organs, such as the uterus.

2.2 Introduction

In vertebrate animals, muscle tissues are usually divided into three types: skeletal, smooth, and cardiac [57]. Skeletal muscle is attached to the bone by tendons [58]. The contraction of skeletal muscle is neurogenic, requiring signal input from the central nervous system, and is generally considered to be voluntary [[58]. Smooth muscles are found in the walls of hollow organs such as blood vessels, the uterus, and the bladder, while cardiac muscle is found in the heart [57]. Smooth muscle and cardiac muscle contractions are initiated by signals from the muscle cells themselves and are considered to be involuntary[59].

There are many cases when understanding the phenomenological effects of involuntary muscles can be investigated at the tissue level. This macro-scale, active contraction behavior of involuntary muscles, such as the uterus, is vital to support its functions, including the uterus' expulsive effect on the fetus as it passes through the birth canal [40]. The contraction speed and contraction capacity are two of the most important parameters to describe muscle tissue's active contraction behavior.

In order to simulate macro-scale biomechanical behaviors -- such as the childbirth process -- the active contraction behavior of the uterus must be accurately modeled. However, this is not as straightforward as it might appear. Several models of the uterus have failed to include the active contraction behavior. For instance, in 2017, Buttin *et al.* [60] established an FEM model of the female reproductive system containing the pelvis, uterus, and fetus to investigate how different forces influence the childbirth process. However, in these simulations, the uterus's active contraction was not simulated directly, but rather an external force was applied through the uterus to simulate what was assumed to be the contraction force. Therefore, the simulation results for these models are limited in the insight that they can provide.

Currently, the most common method to model the active contraction of involuntary muscle is to use a multi-scale, electrical-mechanical coupling model that builds from the cell's behavior (active contraction force generation and ion transmembrane movement) to tissue- and organ-level electrical signal propagation and mechanical deformation [61–63]. Cell-level electrical, chemical, and mechanical behaviors are the mechanisms that initiate the cells' active contraction, which subsequently causes the fiber, tissue, and organ contraction. Unlike for skeletal muscle, very limited constitutive models including the cellular or sub-cellular level biochemical behaviors contributing to the active contraction of smooth muscle cells have been developed. The four-state Hai–Murphy theoretical model [12], describing the kinetics of myosin phosphorylation and cross-bridge interactions with thin filaments, has been widely applied to model smooth muscle cells or tissue's active contraction. Bursztyn *et al.* [27] investigated the responses of the intracellular calcium concentration and the active stress generated inside of the cell to the depolarization of the cell membrane based on the Hai-Murphy model. Stalhand *et al.* [64] developed a three-dimensional mechanochemical continuum model for smooth muscle active contraction within the general thermodynamic framework, in which a free-energy function was proposed as a sum of a mechanical energy, a pure chemical kinetics energy, and a coupling between these two types of energy. The Hai-Murphy model was included for the chemical phase in the model. Liu [65] developed a constitutive model to describe the bio-chemo-mechanical behaviors of the smooth muscle cells, where the Hai-Murphy model was used for biochemical responses. The model was further extended to two-dimensional and three-dimensional structures under a continuum mechanics framework. Murtada *et al*. [66] developed a mechanochemical model coupling the Hai-Murphy model and the Hill model for active force generation to predict smooth muscle contractions. The model results agreed with the isometric and isotonic experiments for smooth muscle tissue in the study.

However, these kinds of models are usually mathematically complex, physiologically complicated, and require special algorithms as well as both high computational capability and computation time. While these sophisticated models can be used to investigate multi-scale responses within the tissue, they are more complex than is needed in the case where the macro-scale mechanical behaviors are of particular interest, such as when working to understand a large deformation within an organ or the solid-fluid interaction within the organ. In reality, due to their complexities, most developed multi-scale models are still far from being able to simulate the behavior at the whole organ level, such as the large deformation of the uterus and its interaction with amniotic fluid and the fetus. For example, in 2015, Cochran *et al*. [67] developed a 3D electro-mechanical coupling model of the uterus to calculate the mechanical and electrical properties and the peak uterine pressure. A similar model was developed by Yochum *et al*. [68] in 2016, where the mechanical and electrical behaviors were analyzed on multiple scales. However, the geometrical models of the uterus in these models were highly simplified to reduce the complexities of the models, and the calculated strain was too small to represent the large deformation of the uterus during parturition. Overall, these multi-scale models are in their infancy when it comes to simulating the uterus's overall behavior during childbirth.

The Hill muscle model is a popular constitutive model that was proposed by physiologist Archibald Vivian Hill in 1938 to describe muscle contractile behavior [69]. It includes both an active, contractile element and passive, elastic elements that provide both resistance to contraction and an ability to return the model to its original length. The basic version of the Hill model is shown in Figure 2.1. It can be modified to include additional elastic elements as well as visco-elastic elements to more completely describe the response of the tissue.

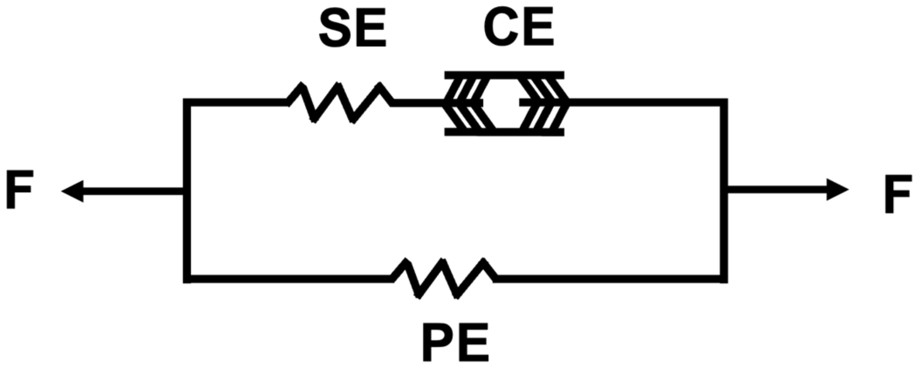

Figure 2.1, Basic mechanical representation of the Hill model, consisting of an active, contractile element (CE) as well as passive, elastic elements in series (SE) and in parallel (PE) with the contractile element based on [70].

This Hill muscle model has been widely used to investigate the effect of voluntary, skeletal muscle contraction on the mechanical function and response of other biological tissues under various external loading conditions [[71–73]. Many of these studies have investigated the role of skeletal muscle in transferring and dissipating loads that result from impacts on the body. In 2008, Hedenstierna *et al.* [72] investigated the effect of human neck muscles on head kinematics and vertebral rotation in rear-end, frontal, and lateral car crashes. In 2009, Iwamoto *et al.* [73] established a finite element model of a driver's arm to investigate how muscle activity influences stresses within the arm, and the resulting injury, during an impact. The skeletal muscle's active contraction was modeled with a 1D truss element whose behavior was characterized by the Hill model. They concluded that both the muscle's stiffness and elbow flexion resulting from contraction have a significant effect on stress distribution and the motion of the arm during a lateral impact. In 2018, Mo *et al.* [71] demonstrated through finite element modeling that both the muscle's active contraction and passive properties have a significant effect on the response of a driver's lower limb and pelvis during emergency braking.

While the Hill model has primarily been used to simulate skeletal muscle activity in computational models, it is still applicable to involuntary muscle simulation. This is because the Hill element is a phenomenological model that does not include the cellular or sub-cellular level mechanisms that produce the macro-scale active contraction behavior, and both skeletal muscle and involuntary muscles share the same phenomena that they can both contract actively and relax, even though the underlying mechanisms for their contractions are different. Therefore, this chapter hypothesizes that the bonding between the contractile fibers using the Hill material model and passive portion of a muscle tissue can be used to describe the active contraction force generated by the tissue that forms hollow organs and match the contraction capacity and contraction speed that has been measured experimentally. Once this behavior is confirmed, these tissue units can be assembled to produce the macro-scale biomechanical behavior of the whole organ.

This chapter steps through the process that was undertaken to develop and characterize a tissue-level unit of involuntary muscle, and then demonstrates how the parameters of the model can be selected in order to match experimentally measured behavior of tracheal smooth muscle.

2.3 Materials and Methods

A generalized structure of involuntary, smooth muscle was created within LS-DYNA. The passive portion of the muscle – representing the non-contractile components of the cells and extracellular connective structures – was modeled as a 100 x 10 x 10 mm solid for convenience in analysis (Fig 2.2 a). The active, contractile portion of the muscle was modeled using four truss element beams, each with a length of 100 mm and a cross-sectional area of 100 mm^2. Each of the four contractile elements was placed along one of the four long edges of the passive solid. The passive solid portion and the four active beams were coupled by sharing the nodes between the beam elements and the solid elements.

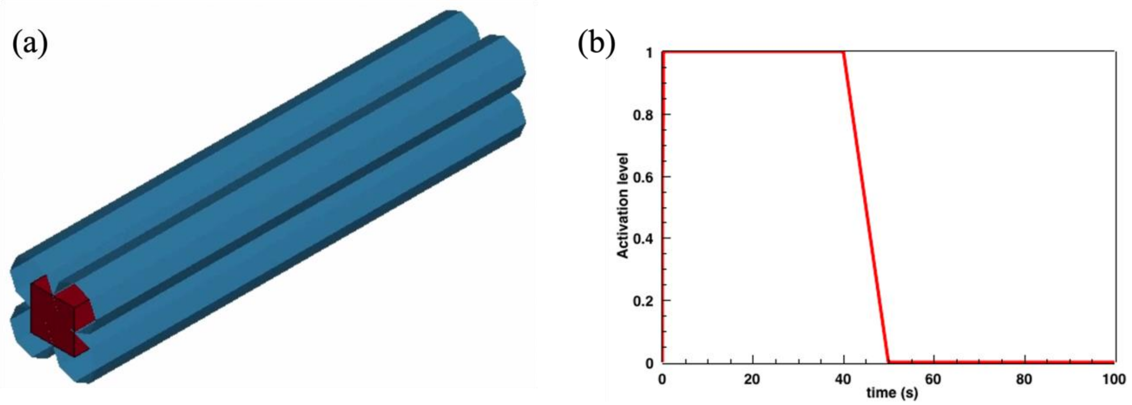

Figure 2.2, Geometrical model of the muscle tissue (a) and Activation level curves that drove the contractile behavior -- for versions of the model with both elastic and hyperelastic materials -- for the solid (passive response) portion of the phenomenological model of smooth muscle (b).

The Hill material model, which is MAT_156 in LS-DYNA, was used for the active beams. It is a one-dimensional model that includes a contractile element, a passive element, and a damping element. The active stress is described as:

$$\sigma_a = \sigma_{max} A(t) F(l) F(v) \tag{1}$$

where: σ_{max} is the maximum isometric stress; $A(t)$ is muscle's activation level, whose value is between zero and one; $F(l)$ is the normalized force-length curve; and $F(v)$ is the normalized force-velocity curve. The normalized force-length curve (SVS) and force-velocity curve (SVR) (Fig 2.3), which describe fundamental responses of muscle and have previously been shown to be appropriate to describe smooth muscle's behavior [74,75], were obtained from the literature [76].

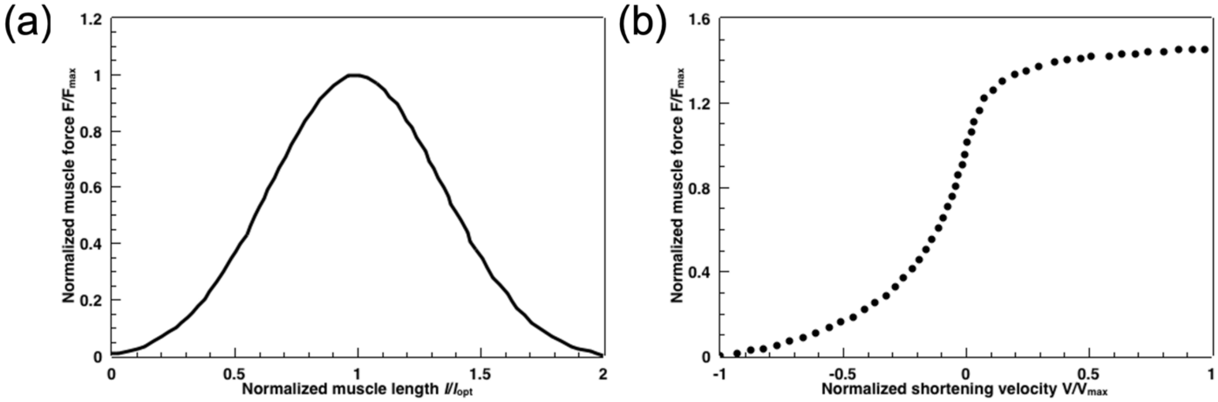

Figure 2.3, Generic active muscle force-length (a) and force-velocity curves (b) that inform the Hill muscle model based on [76].

The passive element stress, σ_p, is determined by the passive mechanical properties of the muscle. Two material models were investigated for the solid portion to represent the muscle's passive behavior. One was an isotropic elastic material, with a Young's modulus (E) of 2 kPa and a Poisson's ratio (u) of 0.495 [77]. The stress-strain relationship is:

$$\boldsymbol{\sigma}_{\mathrm{p}} = (\lambda tr\boldsymbol{\varepsilon})\boldsymbol{I} + 2\mu\boldsymbol{\varepsilon} \tag{2}$$

where λ is the Lame's constant and μ is the shear modulus – both of which can be expressed in terms of the Young's modulus and Poisson's ratio. The second was a hyperelastic material described by the incompressible Mooney-Rivlin model and defined by the equation:

$$W = C_1(\bar{I}_1 - 3) + C_2(\bar{I}_2 - 3) \tag{3}$$

where W is the strain energy density, C_1 and C_2 are material constants, and $\bar{I}_1$ and $\bar{I}_2$ and are the first and second invariants of the left Cauchy-Green deformation tensor (**B)**. The passive stress in this case is defined by:

$$\boldsymbol{\sigma}_{\mathrm{p}}= 2(C_1 + \bar{I}_1 C_2)\boldsymbol{B} - 2C_2\boldsymbol{B}\cdot\boldsymbol{B} - \tfrac{2}{3}(C_1\bar{I}_1 + 2C_2\bar{I}_2)\boldsymbol{I} \tag{4}$$

Experimental data for the stress-strain behavior for smooth muscle was obtained from Pearsall's work [78] and was used to determine the Mooney-Rivlin model parameters for the hyperelastic material (LS-DYNA material model MAT_77 Hyperelastic_Rubber). The material constants were set to values of 1.67 kPa (C_1) and -1.39 kPa (C_2).

In LS-DYNA, the Hill constitutive model has a third element, the damping element. The damping element stress is

$$\sigma_d = \mathrm{DMP}\frac{l}{l_{orig}}\dot{\varepsilon} \tag{5}$$

where DMP is the damping coefficient, l is the length of the muscle at a specific time, l_{orig} is the original length of the muscle, and $\dot{\varepsilon}$ is the strain rate. The total stress is then given by:

$$\sigma = \sigma_a + \sigma_p + \sigma_d \tag{6}$$

The three-dimensional model is realized by coupling the beam and 3D solid components by sharing the nodes between the adjacent elements. The activation level curves, with a range of 0 – 1, used for the contractile beams for both the elastic and hyperelastic solids are shown in Figure 2.2 b. The time at which the activation began to decrease was established based on the point where the composite model (contractile + solid elements) reached its contraction capacity, as explained in the Results section.

The maximum isometric stress (PIS) was initially set at 50 Pa, which was a trial value to generate a relatively small deformation based on the Young's modulus of the muscle tissue, and the damping coefficient (DMP) was 0.001, which was close to 0.004 used previously in the literature for muscle modeling [76]. Such a set of parameters was not selected to represent a specific muscle tissue. There were two purposes to modeling such a generalized muscle tissue. The first was to verify whether the bonding of the active contractile fibers -- using the Hill model -- and a passive portion of the solid elements would work to simulate a muscle's active contraction and relaxation behaviors. The second was to investigate and understand how each of the parameters affects the muscle tissue's mechanical behaviors (such as the contraction velocity, contraction capacity, etc.) quantitively and qualitatively. Therefore, a parametric analysis was also conducted. The range for the parameters is provided in Table 2.1. The Young's modulus values selected of 2, 20, and 40 kPa were within the normal range of values for muscle tissue. However, the range of values for DMP and PIS for muscle tissues, especially smooth muscle tissues, were unavailable from the literature. As such, a range was assumed as shown in Table 2.1.

Table 2.1, Range of parameters investigated for generalized muscle tissue.

Parameter	Range
Young's modulus (E)	2, 20, 40 kPa
Isometric maximum stress (PIS)	5E-5, 5E-4, 5E-3, 5E-2 MPa
Damping coefficient (DMP)	1E-4, 1E-3, 1E-2

The modeling process involved a stepwise approach in order to fully understand the LS-DYNA Hill model parameters and how they interacted with the solid, passive portion of the muscle model. For ease of construction, analysis, and visualization, the initial length of the model element was set at 100 mm.

2.4 Results

2.4.1 Muscle Shortening Response

The initial model version included only the simulation of the contractile beams with truss elements composed of the Hill material. No loading or boundary conditions were applied to the beams. The beginning of the simulation began in an undeformed state (Fig 2.4a). Once the simulation was initiated and the activation reached an instantaneous value of one, the beams started to contract actively from the two ends toward the middle. At t = 25 s, the muscle model had shortened by 27.26 mm (13.63 mm from each end – an overall strain of 27.3%) (Fig 2.4b). At t = 50 s, the beams reached their maximum strain of 41.6 % (Fig 2.4c). Even though the activation started to decrease at t = 40 s, the beams continued to contract until the activation level returned to zero. In addition, the beams remained in this shortened configuration as there was no passive component with an elastic response to return the model to its original length, even though the activation level was zero from 50 seconds to the end of the simulation at 100 seconds (Fig 2.4d).

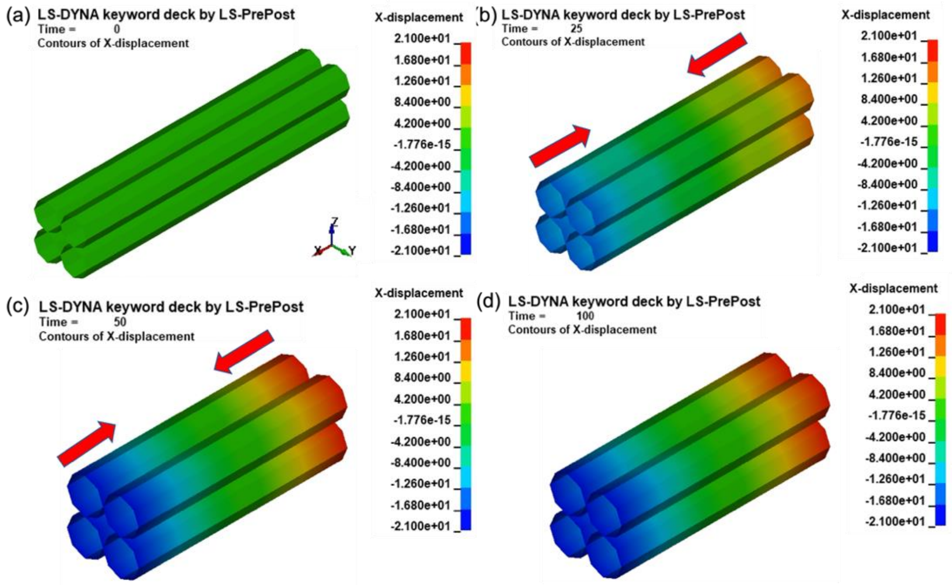

Figure 2.4, Representation of the deformation of the contractile beams under active contraction for times equal to 0 s (a), 25 s (b), 50 s (c) and 100 s (d). (PIS = 50 Pa, DMP = 0.001).

Figure 2.5 shows the deformation of the muscle tissue, which combined the contractile elements and the elastic passive tissue components. There were still no loading or boundary conditions applied to the model. The solid started to contract from the two ends towards the middle once the model was activated. At t = 2 s, the muscle model had shortened by 5.74 mm (Fig 2.5b). At t = 40 s, the solid reached its contraction capacity with a change in length of 8.09 mm (Fig 2.5c). When the activation level began to decrease (t = 40 s), the elastic solid started to return the overall muscle unit to its original state. At t = 100 s, the total x-displacement had dropped substantially to 6.16E-3 mm (Fig 2.5d). The maximum strain generated within the solid was much smaller than when the contractile beams were activated in isolation (8.1% vs 41.6%, respectively). This can be seen by comparing Figure 2.4 and Figure 2.5, and this phenomenon occurs because the solid’s passive mechanical property prevents further contraction. The maximum deformation is determined by the Young’s modulus of the solid in combination with the total force generated by the four contractile beams. In addition, the elastic behavior of the solid supports the restoration of the original state of deformation after the force is removed. This is in comparison to the lack of unloading response for the beams-only model, which demonstrates how important the passive mechanical properties are in regulating the unloading response within muscle.

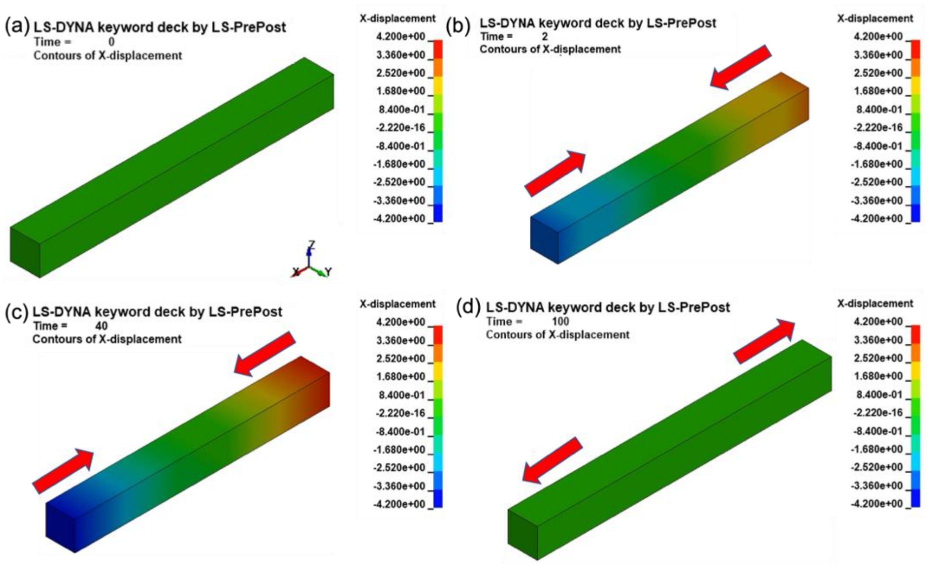

Figure 2.5, Representation of the deformation for the elastic solid and contractile elements under active contraction at times of 0 s (a), 2 s (b), 40 s (c) and 100 s (d). (Hill: PIS = 50 Pa, DMP = 0.001; Passive tissue: E = 2 kPa).

The stress and strain relation for biological tissues, such as the uterus, is usually nonlinear -- especially when the deformation is large [78]. In this study, another FE model of muscle tissue was developed (Fig 2.6a) where the muscle's passive property was modeled as a hyperelastic material using Mooney-Rivlin model. The parameters for Mooney-Rivlin Model were obtained from experimental data [78]. The solid began to contract once the model was activated, and at t = 9 s, the total x-displacement was 10.54 mm (Fig 2.6b). At t = 14 s, the hyperelastic solid had already reached its contraction capacity, where the maximum shortening was 14.20 mm (Fig 2.6c). The solid began to return to its original state with the decrease in the activation level. At t = 39 s, the total x-displacement was 2.16E-3 mm (Fig 2.6d).

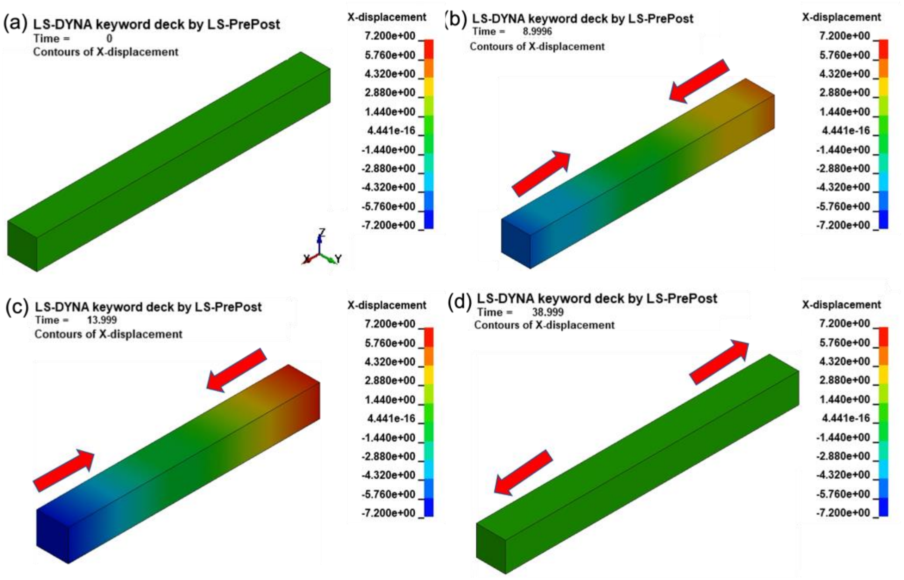

Figure 2.6, Representation of the deformation for the hyperelastic solid and contractile elements under active contraction at t = 0 s (a), 9 s (b), 14 s (c) and 39 s (d). (Hill: PIS = 50 Pa, DMP = 0.001; Passive tissue: $C_1$1.67 kPa and C_2: -1.39 kPa).

2.4.2 Contraction Capacity and Speed Analysis

Different muscle tissues have different contraction patterns, where the contraction capacity (the maximum contraction strain that the muscle structure can develop) and contraction speed are two of the most important variables.

The parameter of maximum isometric stress within the Hill model was found to significantly influence the contraction capacity – it represents the maximum amount of stress that the contractile element can develop. For all three Young's modulus values used to characterize the solid, passive portion of the elastic model (2, 20, and 40 kPa), the maximum strain produced within the solid increased with an increase in the maximum isometric stress (σ_{max} in Eq. 1, Fig 2.7a). As would be expected, lower Young's modulus values allowed more deformation during contraction for each level of maximum isometric stress.

Likewise, the contraction speed of the muscle can be tuned by adjusting the DMP value (Eq. 5). The contraction speed, which is the slope of the curves in Figure 2.7b, increases with a decrease in DMP. The maximum amount of displacement is still governed by the combination of Young's modulus and maximum isometric stress – which is demonstrated by the fact that the curves in Figure 2.7b for damping levels of 0.001 and 0.0001 both plateaued at a level of 4 mm. As the rate of contraction was much lower at the damping level of 0.01, the contraction that was reached was less than the maximum possible and was limited by the time of activation.

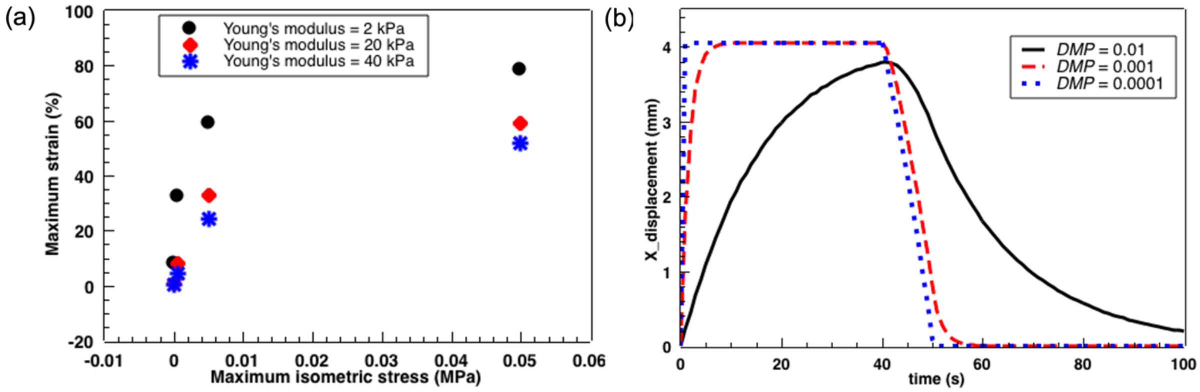

Figure 2.7, Relationship between the maximum strain and maximum isometric stress for an elastic solid component with Young's modulus values of 2 kPa, 20 kPa and 40 kPa (PIS = 50 Pa, DMP = 0.001) (a) and curves describing the deformation due to contraction as a function of time for DMP values of 0.01, 0.001 and 0.0001 (PIS = 50 Pa, E = 2 kPa) (b).

2.4.3 Comparison between the Simulation Results and Experimental Results

An FE model of smooth muscle tissue was established to compare with available experimental results. Despite the fact that our goal is to model the gravid uterus' active contraction, appropriate experimental data of uterine muscle tissue is not available yet to compare with. Therefore, experimental data of the mechanical behavior of tracheal smooth muscle measured by Seow *et al.* [79] was taken as an example. The tracheal smooth muscle's relative length changed during the active contraction and relaxation process. The size of the muscle sample in the experiment was 8 x 0.5 x 0.5 mm. One end of the muscle was fixed while the other end was free. A corresponding FE model was developed. The geometry of the model was 80 x 5 x 5 mm, which is ten times larger than that of the experimental protocol in order to maintain calculation efficiency. Comparisons were made of the strain in the experimental and model tissue, to eliminate size effects. The left end surface of the model was fixed in the x-direction while the right end surface was free. The cross-sectional area of each contractile beam was 6 mm^2. The FE model is shown in Figure 2.8a. The force-length and force-velocity curves are shown in Figure 2.3, which are the generic curves that have been applied to model different muscle structures [76,80]. For different muscle structures, the curves can be different, and experimentally determined curves for these relationships should be used. In this paper, the generic curves were used for the current model due to the lack of experimental data for this specific tracheal smooth muscle tissue. The maximum isometric stress was assumed as 0.085 MPa. The normal range of the isometric stress lies in the range of 0.2 to 1.0 MPa, as recommended by Winters [70]. However, this range is mostly for skeletal muscles in the human body, while the range for smooth muscles has not yet been addressed in the literature. The activation level curve is assumed as shown in Figure 2.8b. Elastic material was used for the passive portion of the muscle, with a Young's modulus of 10 kPa for the tracheal smooth muscle [81] and a Poisson ratio of 0.495. The simulation result of the smooth muscle's relative length during contraction and relaxation matched well with the experimental results, as shown in Figure 2.8c.

Therefore, coupling the contractile fibers using the Hill model and passive muscle portion in LS-DYNA was shown to be able to accurately simulate the contraction behavior of specific involuntary muscle tissue, which means that the Hill model can be appropriately applied to the simulation of hollow organs comprised of involuntary muscle (e.g., uterus) in order to investigate their macro-scale biomechanical behaviors.

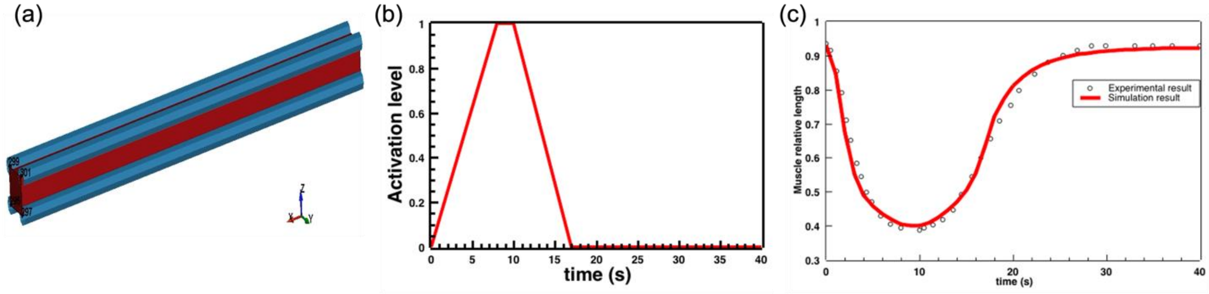

Figure 2.8, (a) FE model of tracheal smooth muscle strip; (b) Activation level; (c) Comparison between the experimental results from Seow *et al.* [79] on tracheal smooth muscle tissue and the simulation results of smooth muscle's relative length during contraction and relaxation. (Hill element: PIS = 0.085 MPa, DMP = 0.05; Passive tissue: E = 10 kPa).

2.5 Discussion

The overall goal of this project is to develop a simulation of uterine contraction that can be integrated into a 3D model of childbirth. Before a full organ model can be developed, it is imperative that the tissue-level model be characterized, and the effect of various parameters be investigated. Before initiating this effort, the current state of muscle models using computational and finite element techniques was investigated to determine if anything could be easily adapted. Modeling that includes the simulation of muscles' active contraction is a popular area of research. However, as is the case for all models, there are limitations associated with these studies. Thus, it is important to understand the goal of each simulation to determine what limitations and assumptions are reasonable and acceptable.

In the area of skeletal muscle effects, some studies have used 1D muscle elements to represent both the muscle's active and passive behavior [82]. Such models are useful when examining the motion of a body segment either due to voluntary contraction or as a result of an externally applied force that is partially resisted by internal muscle forces. However, with 1D models, the effect of the geometry of the muscle cannot be investigated. 3D models of muscle should be more accurate and able to produce more realistic simulations. Further discussions of this trade-off can be found in a review article by Dao [83].

3D, multi-scale, electro-mechanical coupling models of muscle behavior are more common in simulations of cardiac physiology. The strength of these types of models is that they can investigate how the sub-cellular or cellular behavior influences the whole cell or tissue-level behavior. However, such models are usually very large and computationally intensive, and therefore need an extremely large amount of computer memory and high computational time [84]. Moreover, with advances in biological techniques, more variables have been added to the models, which further increases the calculation cost and makes the issue of convergence and parameter sensitivity analysis more challenging as well [84]. Phenomenological models are typically developed based on the macro-level experimental data, which does not include the underlying biological or chemical mechanisms at the cellular or subcellular level. For instance, the components that form the involuntary muscle tissue unit model described in this paper were all derived from experimental data, such as the isometric stress of muscle tissue, the muscle force-length and force-velocity relationships, and the activation level for the active contraction element of the Hill model. The output of both the multi-scale, electrical-mechanical coupling model and a validated phenomenological model will be the active contraction force generated by muscle tissue. However, the phenomenological model is a much simpler and less computationally intensive way to realize that effect and may therefore be the most appropriate way to investigate a hollow organ's macro-scale biomechanical behaviors and their effects. If organs' macro-scale behaviors -- such as active contraction, large deformations, and solid-fluid interactions -- are more relevant to the research question, then this kind of model is a good option. As shown in this paper, coupling between one-dimensional contractile fibers and three-dimensional passive portions of the muscle using FEM techniques is another way to model the muscle's behavior. A significant benefit of the current approach is that it provides a mathematically and computationally simpler process, and it is also more convenient to apply when investigating the effects of anisotropy of both fiber content and orientation in different regions of muscular organs [85].

For hollow, smooth muscle-dominated organs, there has been significantly less research using mechanics-focused computational techniques than have been developed in skeletal or cardiac muscle. The effect of peristalsis has been modeled in digestive organs [[86] and in the female reproductive tract during egg transportation and implantation [87]. The effect of smooth muscle contraction within arteries has also been investigated using finite element techniques [88]. Research into the active contraction of the pregnant uterus is a relatively new research area. The amount of force produced by the uterus during labor and delivery is very different from that produced during peristalsis or vascular contraction. Therefore, the techniques used in other smooth muscle models may not be appropriate for this macro-scale contraction. Some results of simulations have been published; however, in these studies, the active uterine contractions could not be simulated directly, so external loading conditions were applied to represent the contraction effect within their models [60,89].

In order to accurately simulate the contraction of more complicated muscular structures – in particular whole organs – the arrangement of the contractile beams plays a vital role. This arrangement represents the orientation of the muscle cells within the tissue structure, and the variation of this orientation through the muscle thickness has a significant effect on organ behavior [90]. Therefore, the accuracy and biofidelity of any models that include these smooth muscle structures will be greatly improved if they can integrate data from high resolution images of the variation in orientation of the cellular and connective tissue structures within various types of muscle tissue.

2.6 Conclusion

In conclusion, we have established a FEM muscle model and simulated its active contraction and relaxation behaviors successfully by bonding the contractile fibers using the Hill material model and passive muscle tissue using elastic and hyperelastic materials in LS-DYNA. Through the parameter analysis, it was found that a muscle tissue's contraction capacity and contraction speed were mainly determined by the PIS and DMP in the Hill model, respectively. The comparison between the simulation results and experimental results of the tracheal smooth muscle tissue demonstrated that this method is an appropriate option for modeling involuntary muscle's active contraction behavior. The properties of the contractile and solid portions of the composite model can be tuned to match experimentally measured contraction responses, allowing variations in the inherently controlled contraction to be implemented into larger-scale models. This model can now be assembled into hollow organ models, including the uterus, to simulate phenomenological contraction so that their macro-scale biomechanical behaviors can be more accurately investigated in a way that more readily supports parametric assessment due to the reasonable computational requirements.

CHAPTER 3: Simulation of Uterus Active Contraction

3.1 Abstract

Vaginal childbirth is the final phase of pregnancy when one or more fetuses pass through the birth canal from the uterus, and it is a biomechanical process. The uterine active contraction, causing the expulsive force on the fetus, plays a vital role in regulating the fetus's delivery process. In this chapter, a Finite Element Method (FEM) model to simulate the uterine cyclic active contraction and delivery of a fetus was developed in LS-DYNA. The active contraction was driven through contractile fibers modeled as 1D truss elements, with the Hill material model governing their response. Fibers were assembled in the longitudinal, circumferential, and normal (transverse) directions to correspond to tissue microstructure, and they were divided into seven regions to represent the strong heterogeneity of the fiber distribution and activity within the uterus. The effects of each direction of fiber and the combination of different directions of fibers on the contraction pattern of the uterus were investigated. The passive portion of the uterine tissue was modeled with a Neo Hookean hyperelastic material model. Three active contraction cycles were modeled. The cyclic uterine active contraction behaviors were analyzed. Finally, the fetus's delivery through the uterus was simulated. The model of the uterine active contraction presented in this paper modeled the contractile fibers in three dimensions, considered the heterogeneity and anisotropy of the fiber distribution, provided the uterine cyclic active contraction and propagation of the contraction waves, performed a large deformation, and caused the pushing effect on the fetus. This model will be combined with a model of pelvic structures so that a complete system simulating the second stage of the delivery process of a fetus can be established.

3.2 Introduction

The uterus is one of the most important organs for women and a major part of the female reproductive tract. The evolution of uterine mechanical properties caused by hormonal changes, the progression through pregnancy (measured by weeks of gestation), and the number of pregnancies for an individual, contributes to the high complexity of the uterus. All of these modifications lead to the uterus changing even for the same woman during the life. Due to its complexity, the current understanding of uterine mechanical and physiological behaviors is not sufficient. The normal biomechanical function and regulation of the uterus is vital for childbirth. Poor quality uterine contractions contribute to many labor problems, including labor dystocia, which has been proven to be a significant reason for the rising Cesarean section rate [11]. Therefore, it is important to model uterine contraction behavior during the delivery process in order to better understand the pathomechanics of childbirth.

The myometrium, the thickest layer of the uterine wall and the one that contributes to uterine contraction, is also generally divided into three layers: stratum subvasculare for the internal layer, stratum vasculare for the middle layer, and stratum supravasculare for the external layer [91]. The distribution of the smooth muscle fibers in the uterus has been investigated since the nineteenth century. The common point of view was that the fibers in the external layer were mainly in the longitudinal direction [20] [92]. For the inner and middle layers, it was, however, controversial. Wetzstein *et al*. concluded that fibers in the inner layer were predominantly in the circumferential direction and that, in the middle layer, the fibers were like a network running in all directions without preferential direction [20]. In contrast, V. Dubrauszky *et al.* concluded that fibers were like interweaving clusters with no coordinated direction in the inner layer and were in the circumferential direction in the middle layer [92]. The architecture of the fibers was not found to vary significantly between non-pregnant and pregnant samples [92].

For the past two decades, with the advancement of experimental techniques, the investigations of fiber distribution of the human uterus have become popular again. Multiple layers of the fibers with changing orientation through the uterus wall thickness were found [93]. However, the circumferential and longitudinal fibers in the internal layer and external layer, respectively, were still the predominant two kinds of fibers within the uterus [16] [94], which agrees with previous findings. Strong anisotropy of the orientation was found in different regions (the fundus and the body) and through the thickness [51]. More recently, in 2020, Mclean *et al.* used optical coherence tomography (OCT) and developed a pixel-wise fiber orientation tracking method to measure the uterus's fiber orientation in three dimensions for both nonpregnant and pregnant patients. The results showed that there were not only fibers aligning within the tissue surface but also fibers with incline angles with respect to the tissue thickness [19], and that the incline angles were mostly within 10 degrees with respect to the tissue surface for both nonpregnant and pregnant patients

[19]. In addition, more longitudinal direction fibers were found in the uteri of pregnant patients than those of the nonpregnant patients [19]. In 2021, the group further concluded that for the anterior and posterior parts of the uterus, the majority orientation for fibers in the non-pregnant case was at around $\pi/4$ and $3\pi/4$ (45 and 135 degrees), while for the fibers of the pregnant case, the dominant orientation was $\pi/2$ (longitudinal – 90 degrees) [95]. The orientation of the fibers in the fundus area had no predominant direction for both the non-pregnant and pregnant uterus [95]. Previous models just considered the two-dimensional situation, assuming the fibers are all parallel to the tissue surface and evenly distributed within the uterus [96]. It is not clear how important the incline angle of the fiber is to regulate uterine contraction behavior, which means a three-dimensional model of the fiber is needed for such an investigation.

Aside from the strong anisotropy of the fiber orientation within the whole uterus, the content of the fibers, especially the fiber number, length, and density, also varies significantly in different regions of the uterus. Due to the higher thickness and stronger contraction intensity of the fundus area of the uterus, the fiber content in this area is believed to be higher than that of the middle and lower parts of the uterus [23]. Recently, more quantitative studies were conducted. In 2012, Fiocchi *et al.* [94] used 3T-MR DTI (diffusion tensor imaging) with a 3D tractography approach to investigate the fiber number and density for different regions of the uterus. They found that the number and density of the fibers were significantly different for different regions (posterior uterine wall, anterior uterine wall, and anterior isthmus segments). The content of the fibers not only varies in different regions, but also varies through the thickness of the uterine wall. In 2020, Zhang *et al*. [97] investigated the fiber density, fiber length, fractional anisotropy (FA), and apparent diffusion coefficient (ADC), which can be used to reflect the continuity and spatial distribution of fibers in 3D visualization, of the human uterus for both non-pregnant and pregnant patients. In each group, the fiber length, fiber density, FA, and ADC were also significantly different between the outer myometrium and the junctional zone of the uterus. Similar results were also obtained by He *et al* [98], with conclusions that FA values of the junctional zone were significantly higher than that of the myometrium and endometrium, while FA values of the myometrium were significantly higher than that of the endometrium. In 2013, Fujimoto *et al* [17] found that fibers were longest in the outer myometrium (42.0 mm), followed by the junctional zone (34.2 mm) and endometrium (20.0 mm). The number of the fibers was highest in the outer myometrium and much more than that of the junction zone area. The number of fibers in the endometrium area is very small.

Pregnancy was also demonstrated to affect the fiber content of the uterus. The outer myometrium and junction zone of the pregnant uterus showed a decrease in fiber density and FA value along with an increase in fiber length and ADC value compared to the nonpregnant uterus [97]. Due to the importance of the fibers to the contraction behavior of the uterus, it is necessary to develop a model that includes the strong anisotropy and heterogeneity of the fiber orientation and content. While the published simulation models rarely consider such effects on uterine contraction, the ability to analyze these effects were integrated into our model.

The contraction behaviors of the uterus are summarized in Grimm's review [40]. The typical contraction pattern of the uterus resembles a bell-like curve [99], which takes an average of 60 seconds for one cycle [100]. The active contraction is a force wave that is initiated from the fundus and then propagates to the lower part of the uterus, which takes 10 to 20 seconds [23]. While the contraction in different regions starts at different times, the peak force occurs almost at the same time and then relaxation occurs synchronously [23]. In addition, the contraction intensity is higher in the fundus area than in the middle and lower parts of the uterus [23].

Due to ethical issues, human experiments during labor and delivery are difficult to conduct. Computational modeling has become a promising way to investigate the childbirth process. For example, Myers has done several projects focused on the characterization of mechanical properties of maternal tissues [101–103], constitutive modeling [104,105], and finite element analysis of the pre-birth process [106,107]. Oyen developed FEM models to investigate the rupture of the uterus [108] and fibrous tissue during labor [109,110]. There are also some other publications that simulate the movement of the fetus through the pelvis structures without the uterus [52,111]. However, simulation of uterine contraction is still a relatively new research area. In 2017, Buttin *et al*. [60] established a FEM model of the female reproductive system containing the pelvis, uterus, and fetus to investigate how the different forces influence the fetus delivery process. However, in these simulations, the uterus's active contraction was not simulated directly, but rather an external force was applied through the uterus to the rigid fetal model to simulate what was assumed to be the resulting force. In 2015, Cochran *et al*. [67] developed a 3D electro-mechanical coupling model of the uterus to calculate the mechanical and electrical properties and the peak uterine pressure. A similar model was developed by Yochum *et al*. [112] in 2016, where the mechanical and electrical behaviors were analyzed on multiple scales. However, the geometries were highly simplified, and the strain was too small to represent the large deformation of the uterus during delivery. In 2019, Pouca, *et al*. [96] developed a chemo-mechanical coupling model to simulate uterine contraction and fetal delivery. However, the fibers were only two-dimensional and evenly distributed within the uterus. Overall, the existing models in this area still include many significant limitations.

In this chapter, an FEM uterus model was developed in LS-DYNA to simulate uterine active contraction, where the contraction forces were driven by contractile fibers. Multiple mechanical contraction properties of the uterus were included in this model. The fetus delivery caused by the uterine pushing was simulated in the end.

3.3 Materials and Methods

The geometrical models of the uterus and the fetus, shown in Figure 3.1, were designed based on experimental data obtained from real-time magnetic resonance imaging of the uterus and fetus during the second stage of labor [113]. The geometry of the uterus was created in NX software as shown in Figure 3.1b. First, multiple nodes were inserted in a section plane around the fetus model. Then, a curve was generated and adjusted based on the inserted nodes to envelop the fetus model with a shape similar to the outline of the uterus based on the experimental data. Thirdly, three circles in the front, middle, and back position of the fetus were created with two ending points on the curve with varying diameters. According to the curve and circles, three curved surfaces were then generated to form the whole inner surface of the uterus. Finally, the thickness of the surface was set to 1.0 cm (Fig 3.1c). The length and maximum width of the uterus are 34.9 cm and 15.6 cm (Fig 3.1d), and the inner diameter of the cervix is 10 cm (Fig 3.1c). The fetus model includes the fetal head, neck, and body. The fetal head was a sphere with a diameter of 8 cm in our initial model analysis, and the length of the whole fetus (with arms and legs tucked against the body) was about 33 cm. All dimensions were representative of values that might be observed at 40 weeks of gestation.

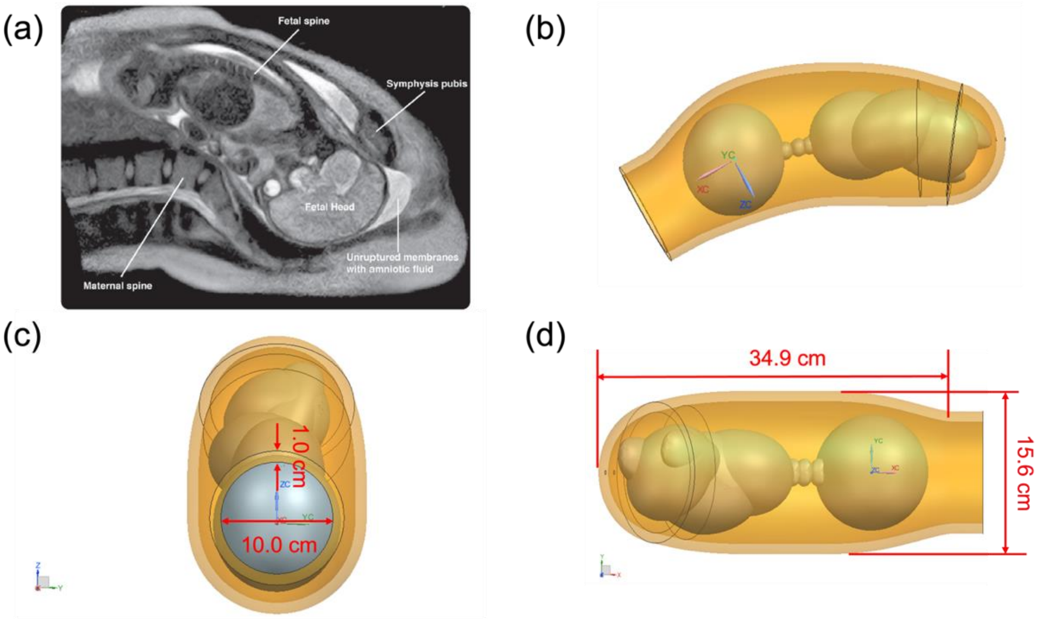

Figure 3.1, MR image of a fetus [113] and fetus geometric model (90th percentile infant) within the uterine model.

The geometric models of the uterus and fetus were then exported to Hypermesh software to generate the mesh. Firstly, the geometry of the uterus was trimmed into two parts with one part of the top half sphere (Fig 3.2a) of the fundus area and the other part of the rest of the uterus so that the mesh of the uterus can maintain the geometrical shape of the uterus and, at the same time, have a good mesh quality. The mesh of each part was finished individually with all hexahedral elements (Fig 3.2b), and the mesh of the interface between the two parts is the same. For the top part of the uterus, the number of the nodes along the circle line of the interface was adjusted within Hypermesh to ensure that there were only hexahedral elements (Fig 3.2c). There are 44 elements for each interface, 5435 nodes, and 6949 elements for the uterus structure in total (Fig 3.2d). Tetrahedral elements were used for the mesh of the fetus with 16736 nodes and 33034 elements in total (Fig 3.3). The mesh for these two structures was then exported to LS-DYNA to assign material properties and boundary conditions and to perform the analysis. The contact between the uterus and the fetus was defined as surface-to-surface contact.

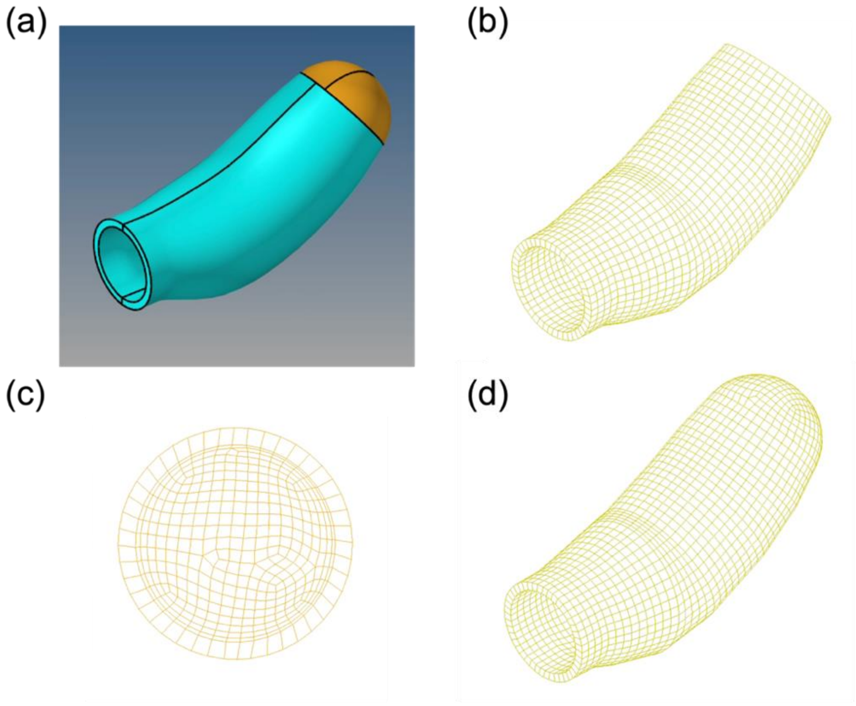

Figure 3.2, The mesh of the uterus model.

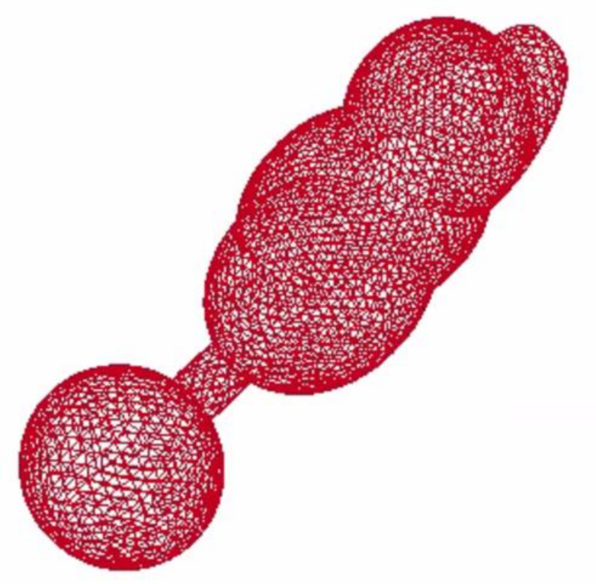

Figure 3.3, The mesh of the fetus.

According to the latest research findings about the orientation and distribution of the fibers inside the uterus for both non-pregnant and pregnant women, the fibers are not perfectly parallel to the tissue surface but are inclined within the uterus wall (Fig 3.4a) [19], which is quite different from the previous research [16,20,92–94,97,98,114]. Therefore, to better understand how fiber orientation affects uterus contraction behavior, it is necessary to model three-dimensional fibers, not only two-dimensional as was done in some previous studies [22]. According to the mechanical perspective, any direction of force can be divided into three basic forces along the x, y, and z coordinate axes. So, three types of fibers in the longitudinal, circumferential, and normal directions, respectively, were generated.

For the longitudinal and circumferential fibers, created the truss beam elements were created along the solid element edges by using the beam generation with edges function in LS-DYNA, and these were as one part (Fig 3.4 b and c). For the normal direction fibers, two different methods were used for the fundus area and the body of the uterus. For the middle and lower parts of the uterus, the node identity number of the edges was collected for both the outer and inner surfaces of each solid element, and every two nodes on both sides were matched with each other. The node identity information was exported to MATLAB software, where a code generated a matrix containing information for every beam element, such as the beam element number, the numbers of the two ending nodes, the part ID, and so on. Then, the matrix was saved as a .txt file using the MATLAB command *csvwrite and was pasted it to the k file of LS-DYNA. For modeling the beam elements of the fundus area of the uterus, the middle and lower parts of the uterus structure were deleted first, leaving only the fundus area, and then the beam elements were created by beam generation with two node sets through the LS-DYNA interface. After combining the beam element information for both the fundus area and the remaining part of the uterus, a final k file was formed that was eventually imported into LS-DYNA to generate the beam elements for the whole uterus in the normal direction (Fig 3.4d). In this case, it was assumed that all of the fibers for each direction are distributed evenly within the uterus. The effects of each direction of fiber on the uterus' contraction pattern were investigated as a first step.

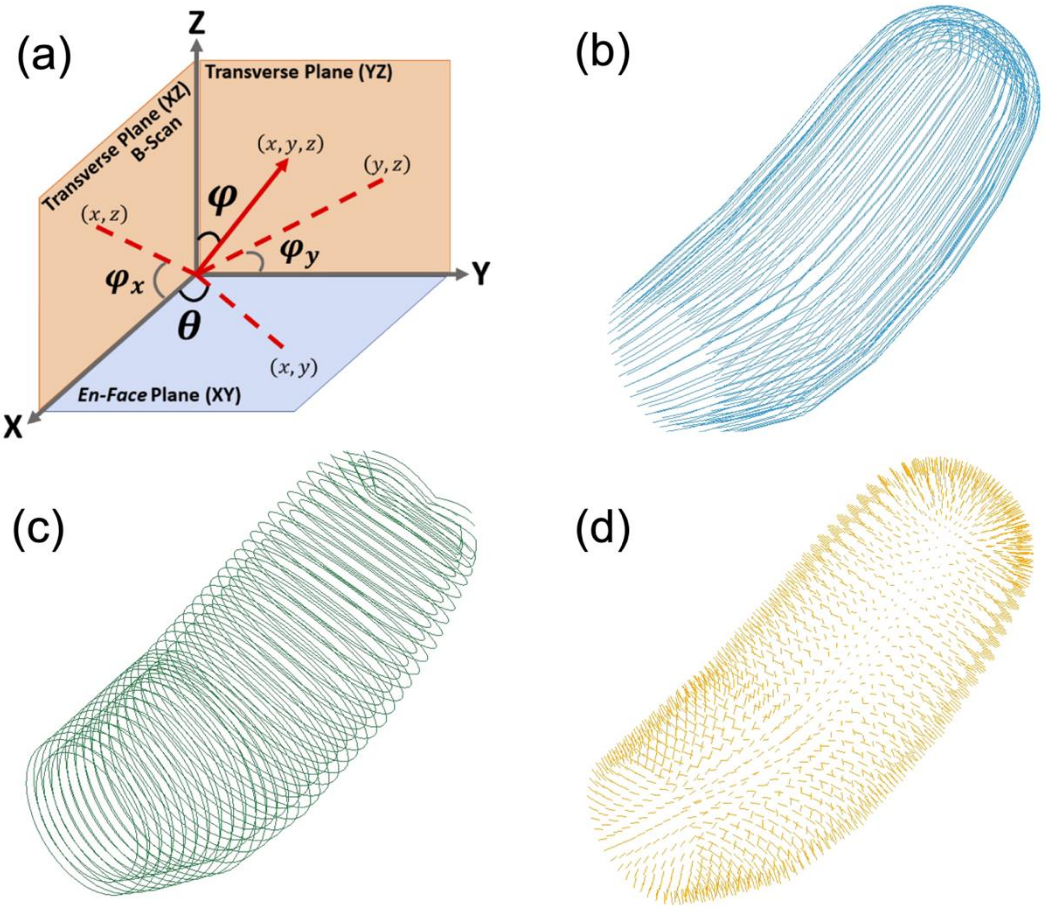

Figure 3.4, Fiber orientation inside of the uterine wall: (a) diagram of a fiber in a random direction [19], (b) fibers in longitudinal, (c) circumferential, and (d) normal directions.

Aside from investigating how each direction of fiber influences uterine contraction pattern, the effects of the combination of the fiber models (i.e., longitudinal + circumferential; circumferential + normal; and normal + longitudinal) on the contraction pattern of the uterus were also studied. Since every individual k file for each type of fiber orientation was created previously, we formed the main k file for combination cases by using the *INCLUDE command. The duplicated information for these three individual k files, such as node number, defined curves, and so on, were deleted automatically by LS-DYNA once the main k file was imported into LS-DYNA. The combined fiber models generated are shown in Figure 3.5: the longitudinal fibers and normal fibers (Fig 3.5a), circumferential fibers and normal fibers (Fig 3.5b), longitudinal fibers and circumferential fibers (Fig 3.5c), and all three types of fibers together (Fig 3.5d).

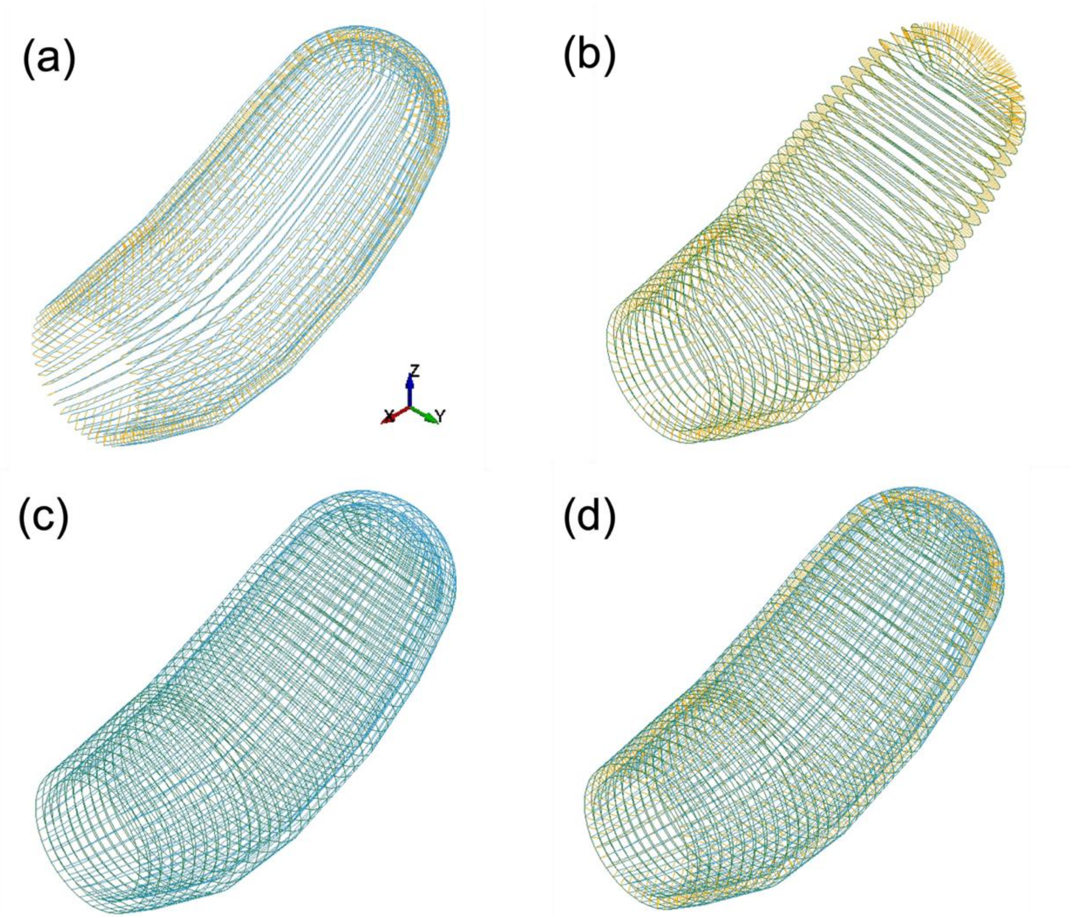

Figure 3.5, Combinations of the fiber models: (a) longitudinal and normal, (b) circumferential and normal, (c) longitudinal and circumferential, and (d) all three directions.

According to the latest experimental findings, the number of fibers with different θ and ϕ angles (Fig 3.4 a) for one segment of the uterus was counted as shown in Figure 3.6 [19]. The red boxes are used to calculate the area in order to estimate the total number of fibers. The number of the θ fibers and ϕ fibers is about 265 x 10^6 and 240 x 10^6, respectively. Further, we estimated the average angle of the ϕ fibers to be 10 degrees based on Figure 3.6b. If it assumed that the fiber cross-sectional area is the same for all of the fibers, then the fiber contraction intensity is only dependent on the fiber number. Considering the incline angle, the intensity ratio between the fibers in the tissue surface and the fibers in the normal direction is about 6:1.

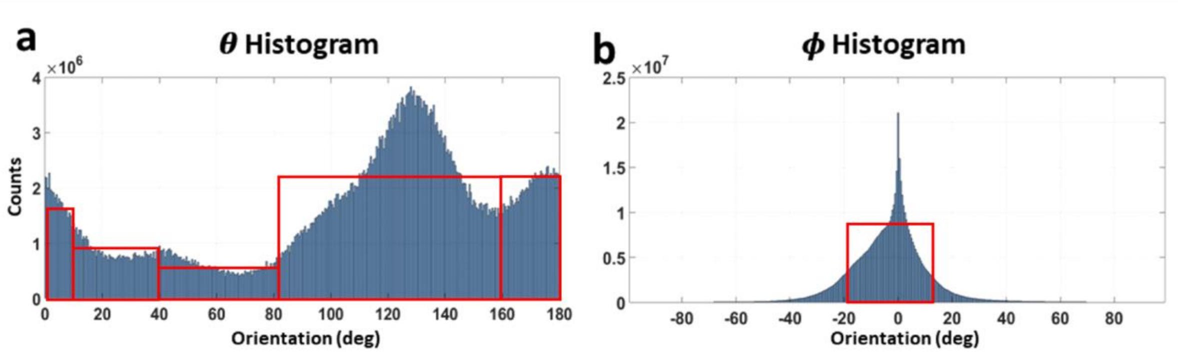

Figure 3.6, Number of fibers in one segment of the uterus [19].

Truss elements are used for such contractile fibers. All beams are bonded with the solid elements that represent the passive portion of the uterus. For the results described in Section 3.4.1, the Hill material model [69] (MAT_156 in LS-DYNA) was used for all the fibers. The PIS (maximum isometric stress) was set at 10 kPa. The activation level of such fibers starts to increase linearly from time = 0 s to time = 28 s, maintains the fully activated status until time = 35 s, and finally decreases to zero at time = 50 s. The solid portion of the model, representing the non-contractile portions of the tissue, has a Young's modulus of 15 kPa and a Poisson's ratio of 0.495 [115]. For the boundary conditions, the nodes on the cervix were fixed in the x, y, and z translation directions. No external loads were applied.

After understanding of effects of fiber orientation on uterine active contraction patterns, the simulations of uterine active contraction and delivery of the fetus through the uterus were conducted, with results discussed in Section 3.4.2. The materials and methods are different from Section 3.4.1, as mentioned in the following paragraphs. For the analysis in Section 3.4.1, the fibers were all evenly distributed within the uterus, had the same contraction intensity, and contracted simultaneously. However, experimental data has shown that both the orientation and distribution of the fibers changes dramatically in different regions of the uterus during pregnancy [85,94,97]. Also, the contraction of the uterus produces a force wave starting from the fundus area and propagating to the lower segments of the uterus, with a higher intensity in the fundus area [23]. Therefore, it was necessary to take such anisotropies and heterogeneities into account to better simulate the uterus' contraction behavior.

In Section 3.4.2, which focused on the uterine active contraction behaviors, these characteristics were considered. To realize this biofidelity, the previous single contractile region of fibers in the longitudinal, circumferential, and normal directions was divided into seven parts for each type of fiber, while the passive portion of the uterus was unchanged. All of the regions are independent from each other, and the three directions of fibers are also independent within each region. To accomplish this, the *ELEMENT information of each k file for the three-direction fibers model where all of the beam elements have the same pid (part identity number) was saved as a separate text file, which was then imported into MATLAB software. In MATLAB, seven different pids were assigned to the beam elements, then the one-part beams were divided into seven groups. Figure 3.7 shows the seven regions for the combination of longitudinal and normal direction fibers (Fig 3.7 a), the combination of circumferential and normal direction fibers (Fig 3.7 b), the combination of longitudinal and circumferential direction fibers (Fig 3.7 c), and the combination of all three directions of fibers (Fig 3.7 d).

The seven independent regions result in a model in which it is possible to adjust the fiber distribution by changing the cross-sectional area in different regions individually while not influencing the fibers in other regions. In addition, in each region, the three directions of fibers were also independent of each other, which means that adjusting the cross-sectional area for one direction of fiber will not affect the fibers in other directions in the same region. This will impact the resultant direction of force generated by the contraction of each muscle element. The model thus has great flexibility to adjust the distribution of the three orientations of fibers within the different regions. The seven different colors for each direction of fiber (Fig 3.7 a, b, & c), were used to differentiate the fibers of the seven different regions. The seven regions were arranged from the top to the bottom of the uterus. At the interfaces between every two regions, they share the same element nodes.

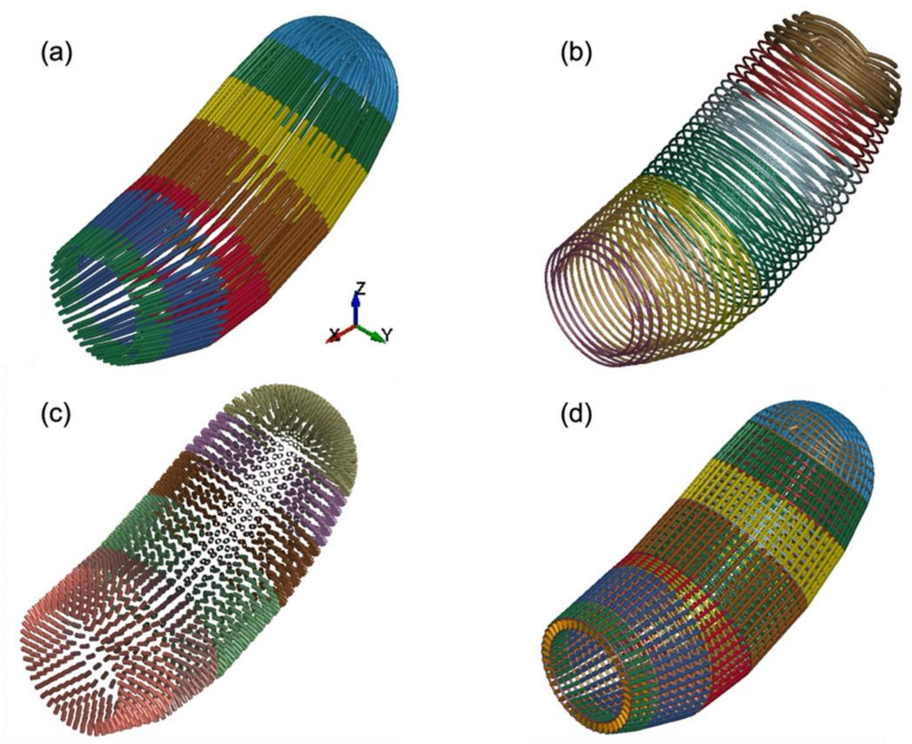

Figure 3.7, Contractile fibers inside of the uterine wall: (a) longitudinal, (b) circumferential, (c) normal, and (d) the combination of these three directions of fibers. The numbering of the regions goes from the top to the bottom of the uterus. Specifically, region 1 is the fundus (the top region) area, region 7 is the lowest region, and region 2 – 6 are the regions in the middle.

The distribution of the fiber content varies significantly in different regions of the uterus. For example, the fiber content has been found to be higher in the fundus region of the uterus than in the mid-regions [23]. Also, the longitudinal direction fibers are the dominant fibers in the mid-corpus of the uterus [19]. In this uterine simulation model, the average size of a solid element was around 10 mm x 10 mm x 10 mm (Fig 3.8) – with a cross-sectional area of 100 mm^2. For each solid element, there are twelve edges that are all bonded with fibers: four in the longitudinal direction; four in the circumferential direction; and four in the normal direction. The cross-sectional area for each longitudinal fiber was 20 mm^2, while each longitudinally oriented edge of a solid element was shared by two elements. As a result, the contribution of each longitudinal fiber for a single solid element would be 10 mm^2. The total cross-sectional area from these four associated longitudinal fibers is thus 40 mm^2; therefore, the content of longitudinal fibers would be approximately 40% for a random solid element. The reason for the approximation is that the complex shape of the uterus results in some variation in the element shape from a perfect cube.

Similarly, the contribution of the four 20 mm^2 circumferential fibers to each element was around 40% of the cross-sectional area in the fundus region. The cross-sectional area of each normal fiber was set as 6 mm^2 in the model, in order to represent the fact that the fibers within the uterine wall are not perfectly parallel to the uterine wall surface but are inclined with small angles [19]. Each edge on which a normal fiber was located is shared with four surrounding solid elements, so the contribution of the four normal fibers was 6% of the cross-sectional area of the element. As a result, the volume content of all the fibers in total was about 86%, which is close to the experimental finding that -- in a fundal region of a pregnant uterus' myometrium -- smooth muscle cells that equate to the fibers account for approximately 80% of the total tissue volume [19]. Also, in the mid-corpus of the uterus, the longitudinal direction fibers were the dominant ones [85]. Therefore, in this model, the cross-sectional area of the circumferential fibers was set as 6 mm^2 in the mid-corpus, with the other two directions of fibers unchanged. As a result, the total fiber content in the mid-corpus was 58%, which was also comparable to the range of fiber content measured in the mid-corpus for the pregnant and unpregnant uterus of 40% and 63%, respectively [116].

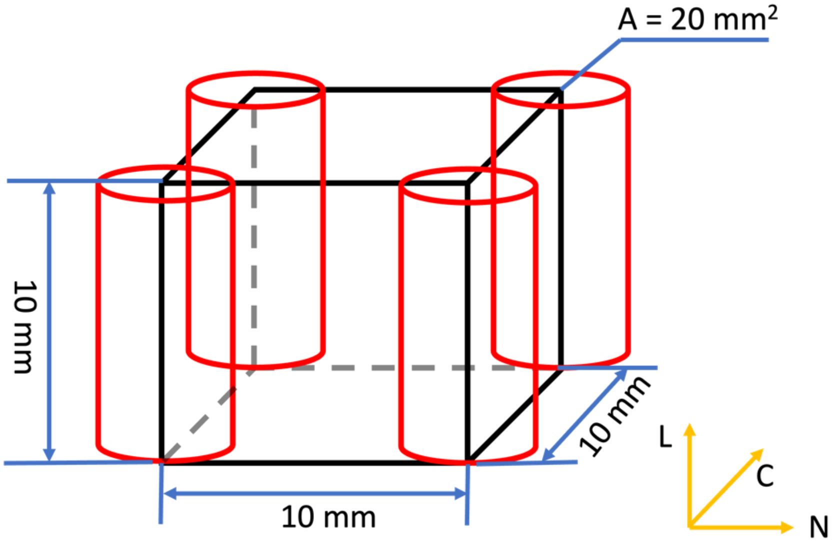

Figure 3.8, A random element showing the muscle tissue volume and four fibers in the longitudinal direction. L, C and N represent the longitudinal, circumferential, and normal directions, respectively.

The SVS and SVR in the Hill material model within the uterus were the same as the values used for modeling the isolated muscle tissue, as described in Chapter 2 [76]. Values were set at a PIS of 1.0 MPa and a DMP of 100. The parameters of PIS and DMP for the Hill model were assumed based on the degree of tissue contraction that is needed to push the fetus from the uterus with an overall delivery time that aligns with clinical observation. For PIS, which again is the maximum isometric stress that can be developed by the tissue, the selected value of 1 MPa is comparable to values of 0.5 – 1 MPa used in prior muscle modeling described in the literature [117]. Clinically, delivery time can vary significantly, from 2 minutes to 200 minutes [118]. In this simulation, it was assumed that the fetus would be delivered within 3 minutes. The activation level curves for the seven regions were assumed as shown in Figure 3.9, where the starting time for region one was at time 0 s. Each of the subsequent regions began contracting 2 seconds later than the previous region to simulate the propagation of the contraction wave. The propagation of a contraction wave initiated from the fundal region to the middle and then the lowest region of the uterus takes about 10-20 seconds to finish, according to experimental findings [23] and has been modeled as 12 seconds in previous simulations [67,68]. In this model, the uterus was divided into seven regions, and the delay for each region was 2 seconds so that the time period for the propagation was 12 seconds in total. All of the regions reached a fully activated status and then began to relax synchronously, which was based on the physiologic behavior of the uterus [23]. Three contraction cycles were modeled in this study.

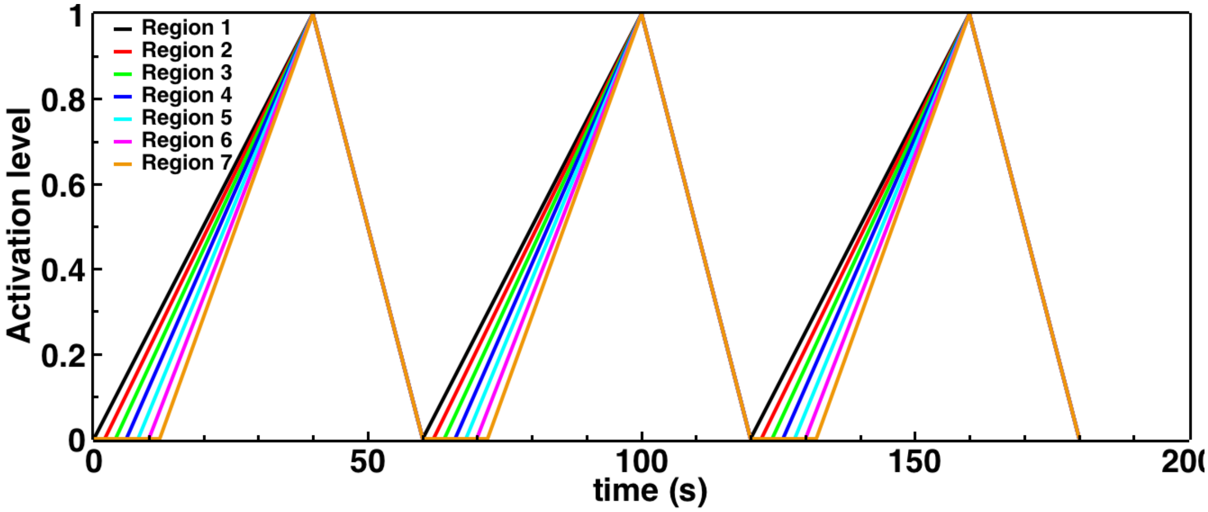

Figure 3.9, Activation level curves for seven regions of the contractile fibers.

The passive portion of the uterus, representing the non-contractile portions of the tissue, was modeled as a hyperelastic material with a Neo Hookean model (C1= 0.03 MPa) [60]. The fetus was modeled as a rigid body. The solid hexahedral elements for the uterus were coupled with the truss elements for the contractile fibers by sharing the nodes. The cervix was fixed in the space as the boundary condition. No external loads were applied.

3.4 Results

3.4.1 Effects of Fiber Orientation on Uterine Active Contraction

3.4.1.1 Longitudinal-Only Fiber Model

The simulation results for the longitudinal-only fibers model are shown in Figure 3.10. The maximum principal strain of the solid elements was recorded. At t = 0 s, there was no deformation (Fig 3.10a). After that, the whole uterus started to contract simultaneously. By t = 3 s, the largest maximum principal strain among the solid elements of the whole uterus was 5.1% (Fig 3.10b). The lowest maximum principal strain was about 1.0%. The fundus and the cervix area had bigger strain values, while in the middle range of the uterus, the strain distribution was quite uniform. The fundus area moved slightly downwards. By t = 11 s, the largest maximum principal strain was 15.7% (Fig 3.10c). The fundus area moved more towards the cervix, which caused the uterus to shorten in the longitudinal direction while expanding slightly in the transverse direction. The strain in the middle part of the uterus was still very uniform and relatively small compared to the fundus and cervix area. By t =18 s, the largest strain was 22.8% (Fig 3.13d). By t =23 s, the largest strain was 26.9% (Fig 3.10e). The uterine structure further shortened in the longitudinal direction and expanded more in the transverse plane. The entire uterus continued to contract until about 32 seconds, where the largest stain was 31.7% (Fig 3.13f). The uterus became much shorter and wider. From 35 seconds, with the decrease of the activation level, the uterus started to relax due to the elastic response of the non-contractile tissue. At t = 50 s, the uterus almost returned to its initial state, and the largest strain was 3.8%.

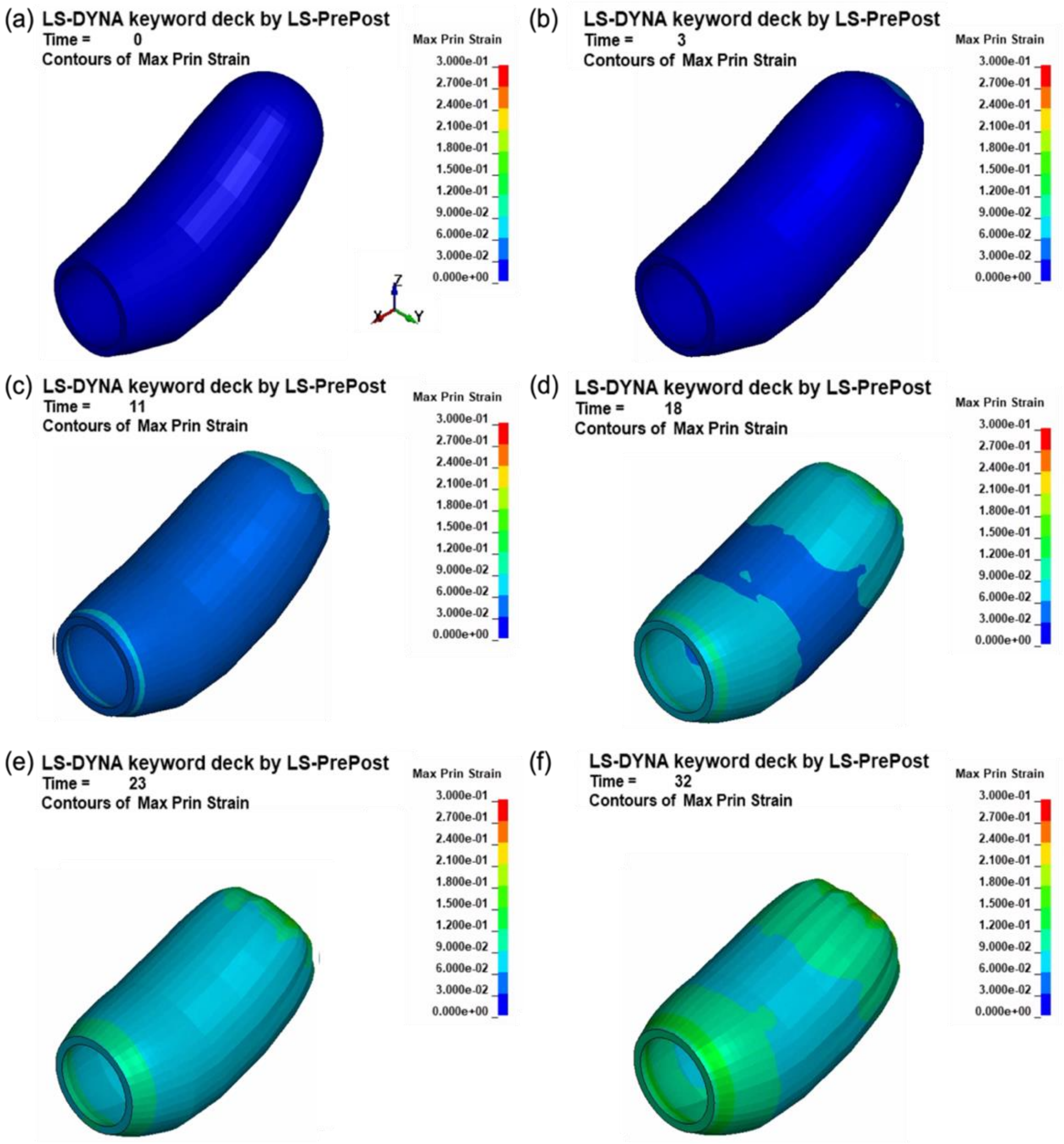

Figure 3.10, Simulation results of maximum principal strain with time for the longitudinal-only fiber model.

3.4.1.2 Circumferential-Only Fiber Model

The simulation results for the circumferential-only fibers model are shown in Figure 3.11. Again, the maximum principal strain of the solid elements was recorded. At t = 0 s, there was no deformation, so the maximum principal strains were all zero (Fig 3.11a). By t = 3 s, the largest maximum principal strain among the solid elements of the whole uterus was 6.3% (Fig 3.11b). The area of the fundus and the anterior part had bigger strain values, while in the middle posterior part of the uterus, the strain distribution was uniform, and the value was smaller. The fundus area moved slightly upwards. By t = 11 s, the largest maximum principal strain was 16.0% (Fig 3.11c). The fundus area moved further upwards, which caused the uterus to be extended in the longitudinal direction while it contracted slightly in the transverse direction. The strain in the middle, posterior part of the uterus was still very uniform and relatively small compared to the fundus and anterior area. By t =18 s, the largest strain was 22.5% (Fig 3.11d). By t =23 s, the largest strain was 26.5% (Fig 3.11e). The uterine structure further extended in the longitudinal direction and contracted more in the transverse plane. The entire uterus continued to contract until about 32 seconds, where the largest stain was 31.2% (Fig 3.11f). The uterus became much longer and thinner.

By comparing these results with those of the longitudinal-only fibers model where the longitudinal fibers contributed to the contraction in the longitudinal direction and expansion in the transverse direction, it can be seen that the circumferential fibers had the opposite effect -- as the uterus extended in the longitudinal direction and contracted in the transverse direction. For the circumferential-only fiber model, the strain was bigger in the anterior regions because stress concentrations occurred in that area due to the shape of the uterus model, which caused the structure to bend.

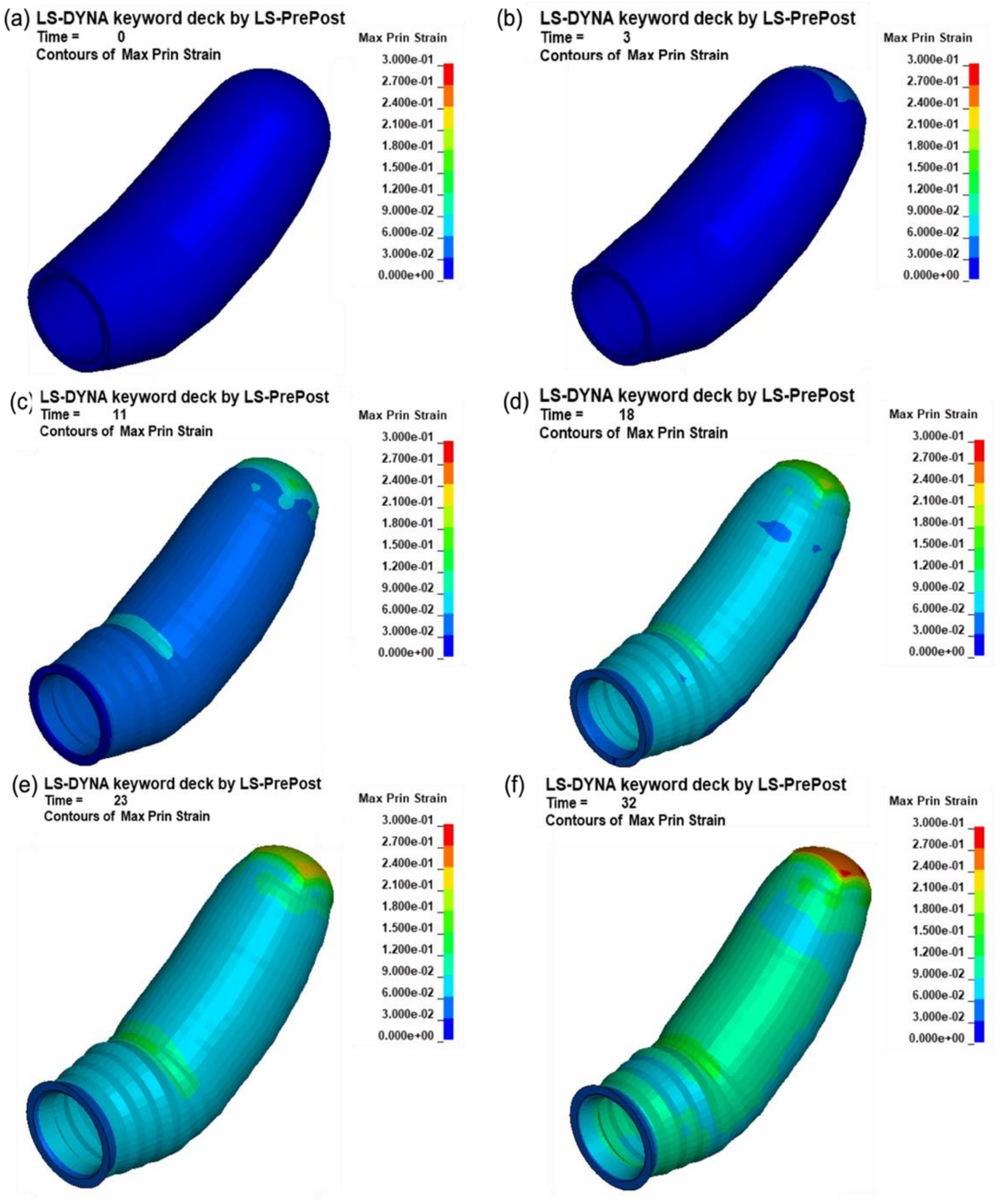

Figure 3.11, Simulation results of maximum principal strain with time for the circumferential-only fibers model.

3.4.1.3 Normal-Only Fiber Model

The simulation results for the normal-only fibers model are shown in Figure 3.12. At t = 0 s, no deformation occurred (Fig 3.12a). After that, the uterus started to deform. By t = 3 s, the largest maximum principal strain among the solid elements of the whole uterus was 2.2% (Fig 3.12b). The area of the fundus and the anterior region had larger strain values than the posterior region. The fundus area moved slightly upwards. By t = 11 s, the largest maximum principal strain was

6.3% (Fig 3.12c). The fundus area moved a little more upwards but not significantly, and there was no obvious deformation happening in either the longitudinal direction or the transverse direction. The strain in the posterior part of the uterus was still relatively small compared to the fundus and anterior area. By t =18 s, the largest strain was 8.7% (Fig 3.12d). By t =23 s, the largest strain was 10.3% (Fig 3.12e). The entire uterus continued to contract until about 32 seconds, where the largest stain was 12.2% (Fig 3.12f). Compared to the initial configuration, the uterus just very slightly extended in the longitudinal direction, which means that the normal direction fibers do not contribute much to the deformation of the uterus structure.

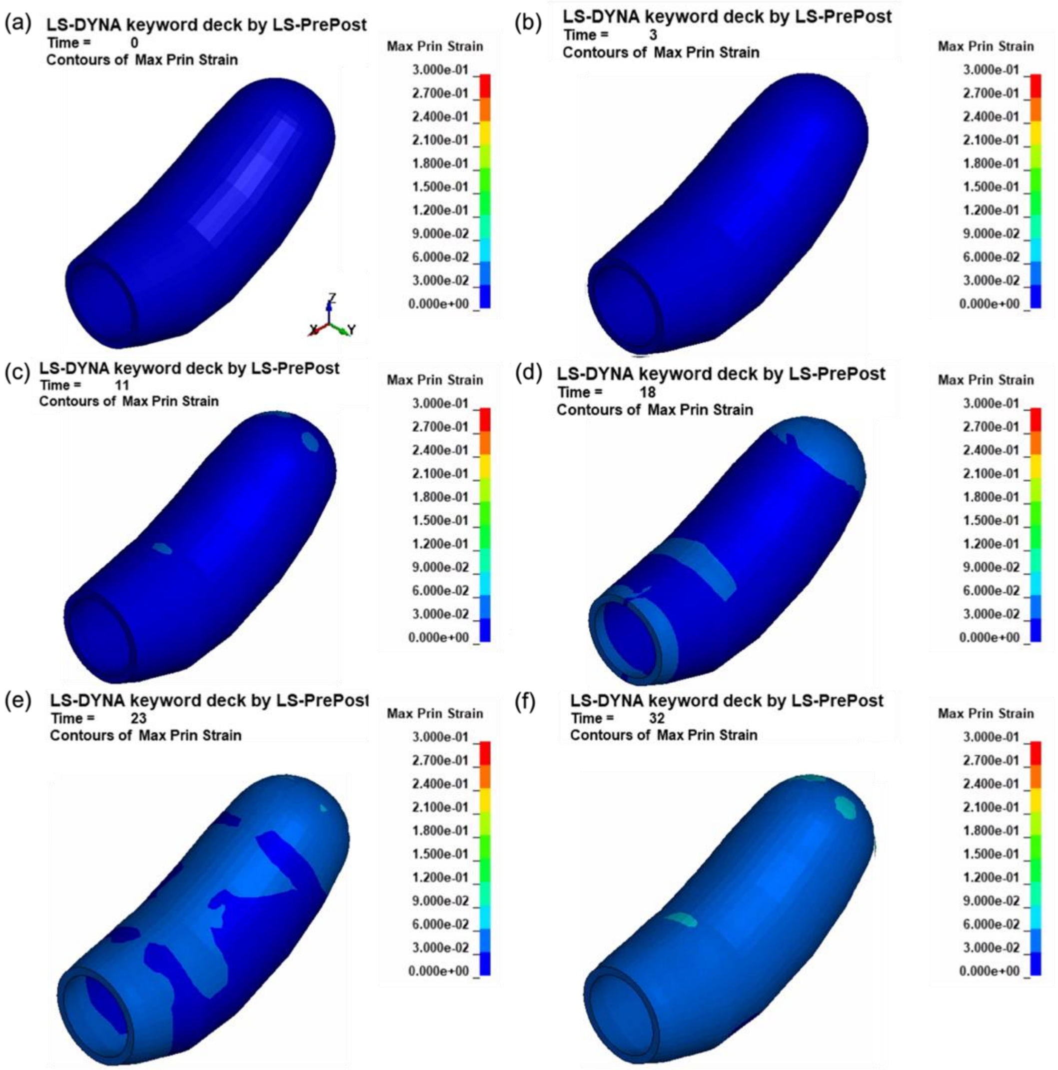

Figure 3.12, Simulation results of maximum principal strain with time for the normal-only fibers model.

3.4.1.4 Longitudinal + Normal Fiber Model

After analyzing how the three directions of fibers individually affect the uterus' contraction pattern, we further investigated the effect of a combination of these fibers on uterine contraction. The simulation results for the combination of longitudinal and normal fibers are shown in Figure 3.13. The uterus started to deform once it was activated at t = 0 s. By t = 3 s, the largest maximum principal strain among the solid elements of the whole uterus was 4.0% (Fig 3.13b). The fundus and the lower part had bigger strain values. The fundus area moved slightly downwards. By t = 11 s, the largest maximum principal strain was 12.0% (Fig 3.13c). Similar to the longitudinal-only fibers model, the fundus area moved further downwards, which caused the uterus to shorten in the longitudinal direction and expand slightly in the transverse direction. The strain in the middle part of the uterus was still very uniform and relatively small compared to the fundus and cervix area. By t =18 s, the largest strain was 16.7% (Fig 3.13d). By t =23 s, the largest strain was 19.3% (Fig 3.13e). The uterine structure further shortened in the longitudinal direction and expanded more in the transverse plane. The entire uterus continued to contract until about 32 seconds, where the largest stain was 22.1% (Fig 3.13f). The uterus became much shorter and wider. As seen in the previous simulations, the uterus started to relax once the activation level decreases.

Compared to the longitudinal-only fibers model, the final uterine configurations were very similar. Also, the x, y and z displacement with time of the same peak node for the longitudinal only fiber model and combination model were recorded as shown in Figure 3.14a. No big difference was found between these two curves, which demonstrated that the deformation among the whole uterus was not changed significantly. However, the maximum principal strain for each case was much smaller than that of the longitudinal-only fibers, and the distribution of the strain (the color map) was significantly changed. Also, the maximum principal stress of the same element in the fundus area for the two models showed a significant difference (Fig 3.14b). Therefore, even though the normal direction fibers do not play a large role in regulating the whole uterus deformation during contraction, they influence the stress and strain distribution within the uterine wall.

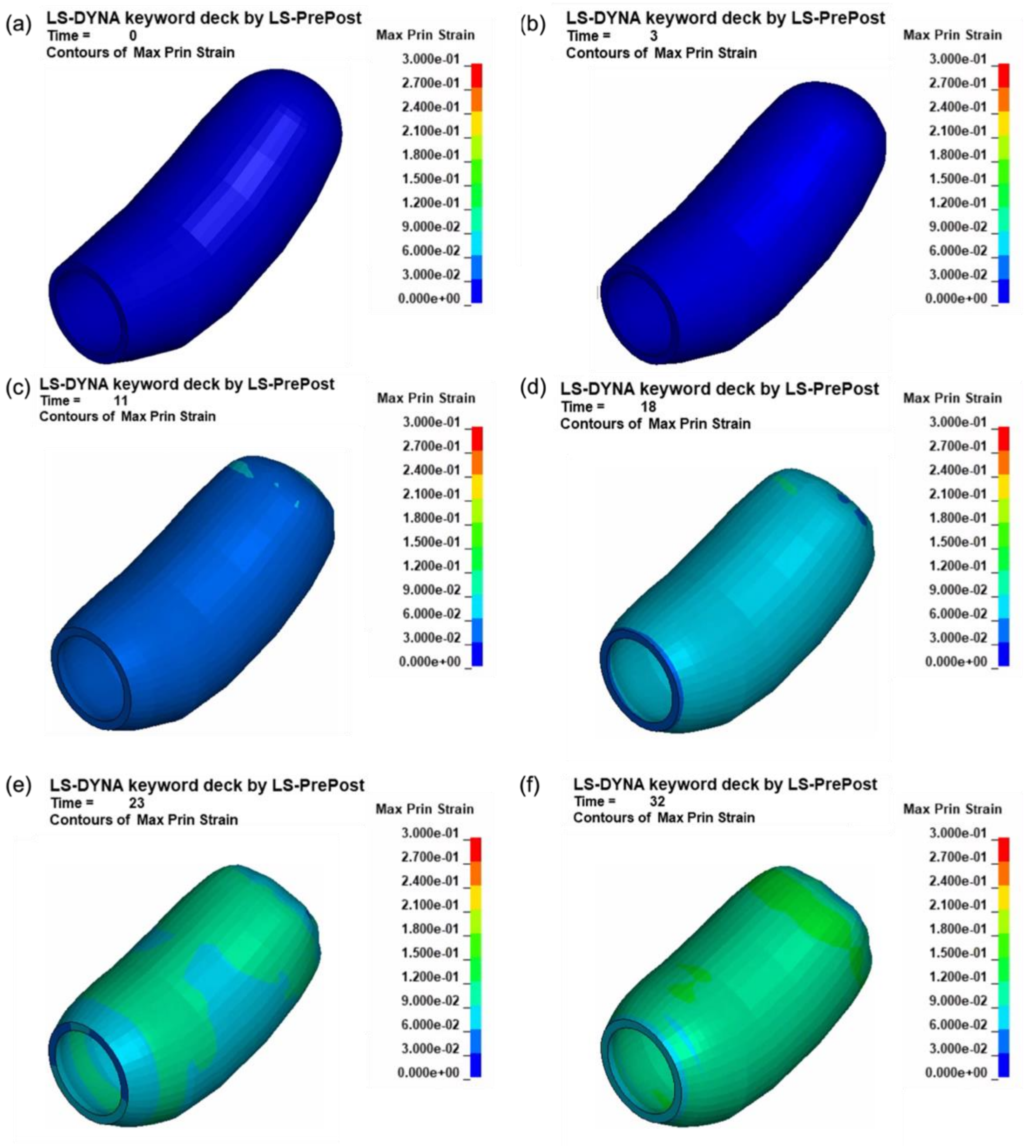

Figure 3.13, Simulation results of maximum principal strain with time for the longitudinal-normal fibers model.

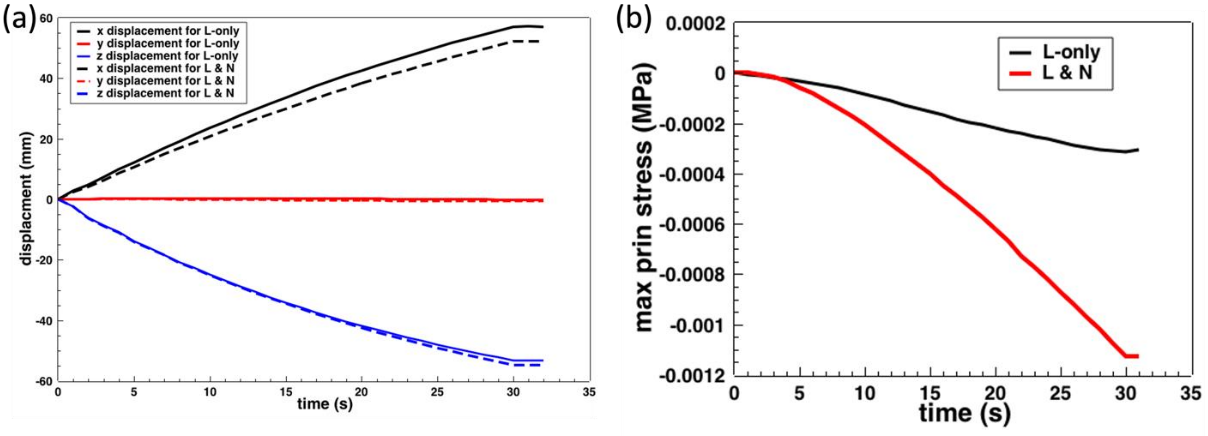

Figure 3.14, Comparison of the displacement of the peak node and maximum principal stress of the element in the fundus region between the longitudinal-only model and the longitudinal & normal model.

3.4.1.5 Circumferential + Normal Fiber Model

The model in which circumferential and normal fibers were combined was the next one to be analyzed, and the results are shown in Figure 3.15. By t = 3 s, the largest maximum principal strain among the solid elements of the whole uterus was 4.0% (Fig 3.15b). The area of the fundus and the anterior uterus had larger strain values. The fundus area moved slightly upwards, and -- by t = 11 s -- the largest maximum principal strain was 11.8% (Fig 3.15c). The fundus area moved further upwards, which caused the uterus to extend in the longitudinal direction while contracting slightly in the transverse direction. The strain in the posterior part of the uterus was still very uniform and relatively small compared to the fundus and anterior area. By t =18 s, the largest strain was 16.8% (Fig 3.15d). By t =23 s, the largest strain was 19.7% (Fig 3.15e). The uterine structure further extended in the longitudinal direction and contracted more in the transverse plane. The entire uterus continued to contract until about 32 seconds, where the largest stain was 23.3% (Fig 3.15f). Similar to the Circumferential-only fiber model, the uterus eventually became much longer and thinner.

Compared to the circumferential-only fibers model, the final configurations of this combination were very similar. In addition, there was very little difference for the y and z displacement of the same peak node for the two models, even though the x displacement showed a difference (Fig 3.16a). However, the maximum principal strain was much smaller than that of the circumferential-only fibers, and the stress and strain distribution changed dramatically due to addition of the normal direction fibers. The maximum principal stress of the same element in the fundus area for the two models showed large differences (Fig 3.16b), which also demonstrated that a 3D fiber model is necessary to develop a more accurate uterus contraction model. Even though the circumferential-only and normal-only fiber models both influence the extension in the longitudinal direction, when they act together, such effect was weakened.

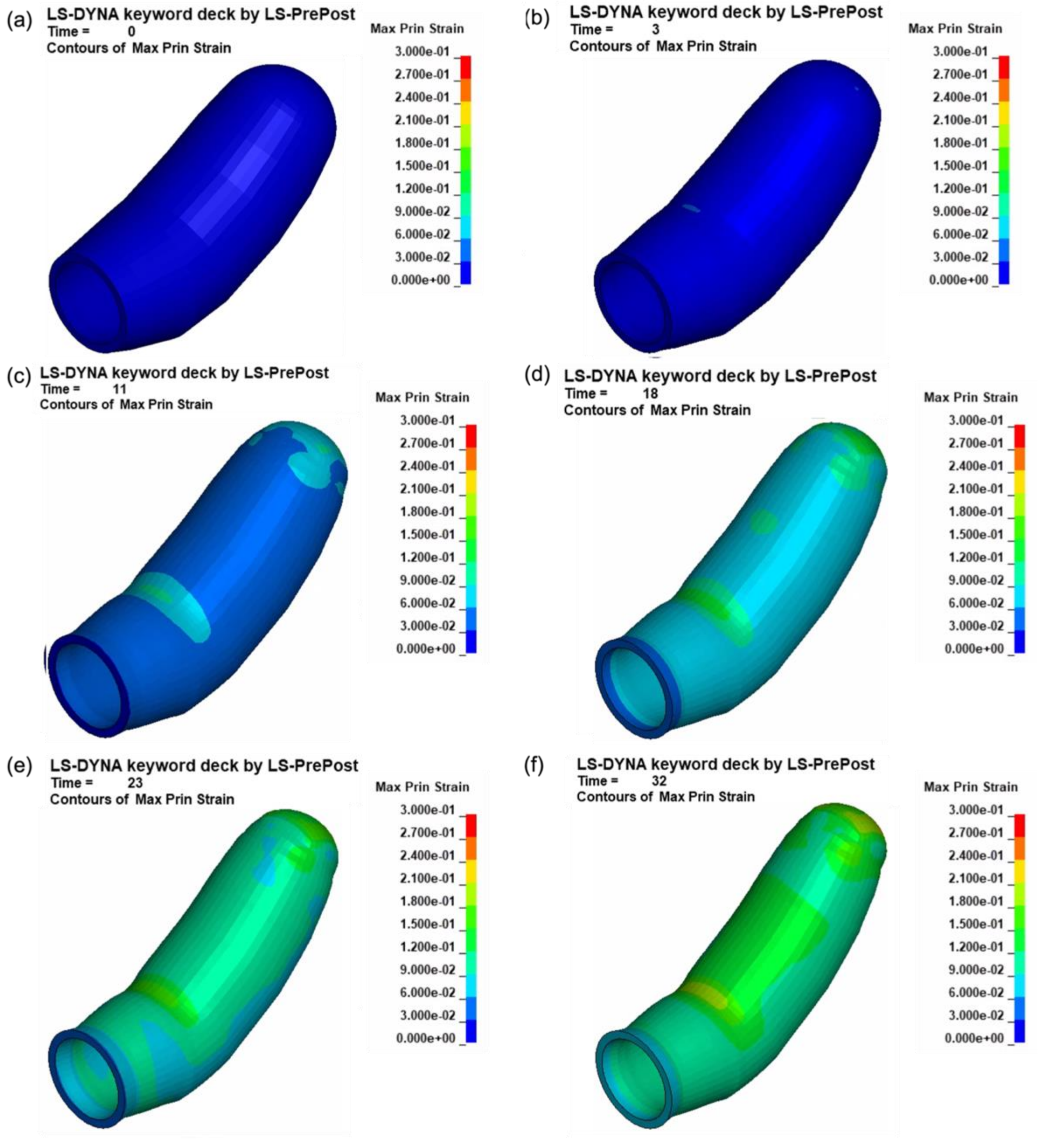

Figure 3.15, Simulation results of maximum principal strain with time for the circumferential-normal fibers model.

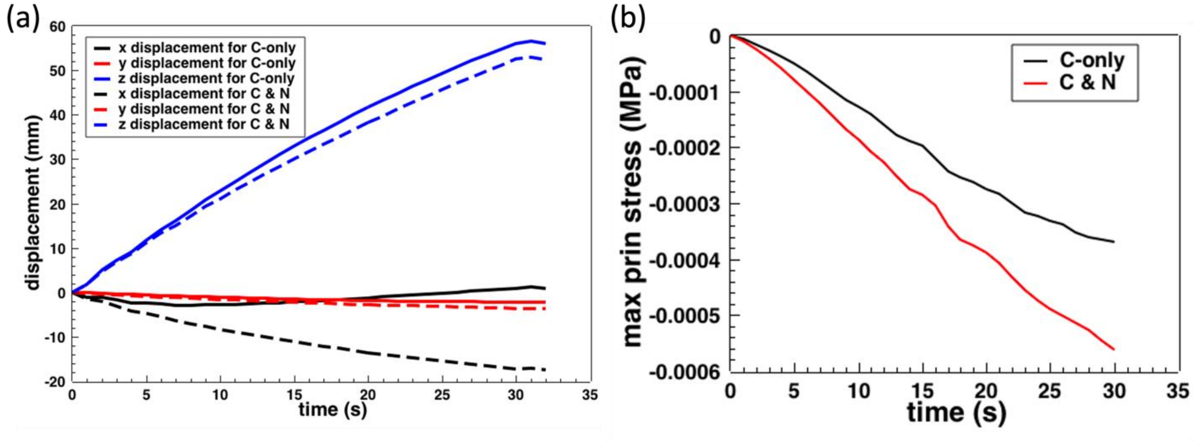

Figure 3.16, Comparison of the displacement of the peak node and maximum principal stress of the element in the fundus area between the circumferential-only model and the combined circumferential & normal model.

3.4.1.6 Longitudinal + Circumferential Fiber Model

As a final step towards understanding the role that the various fiber directions play, the combination of longitudinal and circumferential fibers was simulated, and its results are shown in Figure 3.17. The uterus started to contract at time = 0 s, and by t = 3 s, the largest maximum principal strain among the solid elements of the whole uterus was 1.6% (Fig 3.17b). The fundus and the anterior region had larger strain values than in the posterior region of the uterus, which was different from the longitudinal-only fiber model where the strain was very uniform in the middle region of the uterus. Also, the distribution of the strain was more uniform compared to the circumferential-only fiber model. The fundus area moved very slightly downwards. By t = 11 s, the largest maximum principal strain was 5.5% (Fig 3.17c). The strain in the posterior portion of the uterus was relatively small compared to the fundus and anterior area. By t =18 s, the largest strain was 8.5% (Fig 3.17d). By t =23 s, the largest strain was 10.5% (Fig 3.17e). The uterine structure further extended a little in the longitudinal direction and contracted in the transverse plane. The entire uterus continued to contract until about 32 seconds, where the largest stain was 13.2% (Fig 3.17f).

Compared to the longitudinal-only and circumferential-only fibers model, the final deformation of this model was very small. In addition, the maximum principal strain was much smaller than that of the longitudinal-only and circumferential-only fibers. Also, the distribution of the strain changed. Considering that the circumferential-only and longitudinal-only fibers have the opposite effect on the deformation of the uterus, both effects were significantly weakened when they act together. Also, in this model, both directions of fibers have the same intensity. Therefore, in order to simulate the uterus’ function to contract and push the fetus to deliver, the intensity of the longitudinal fibers must be much stronger than that of the circumferential fibers, which agrees with the experimental findings that, in the pregnant uterus, there are many more longitudinal fibers than in that of the non-pregnant uterus [19].

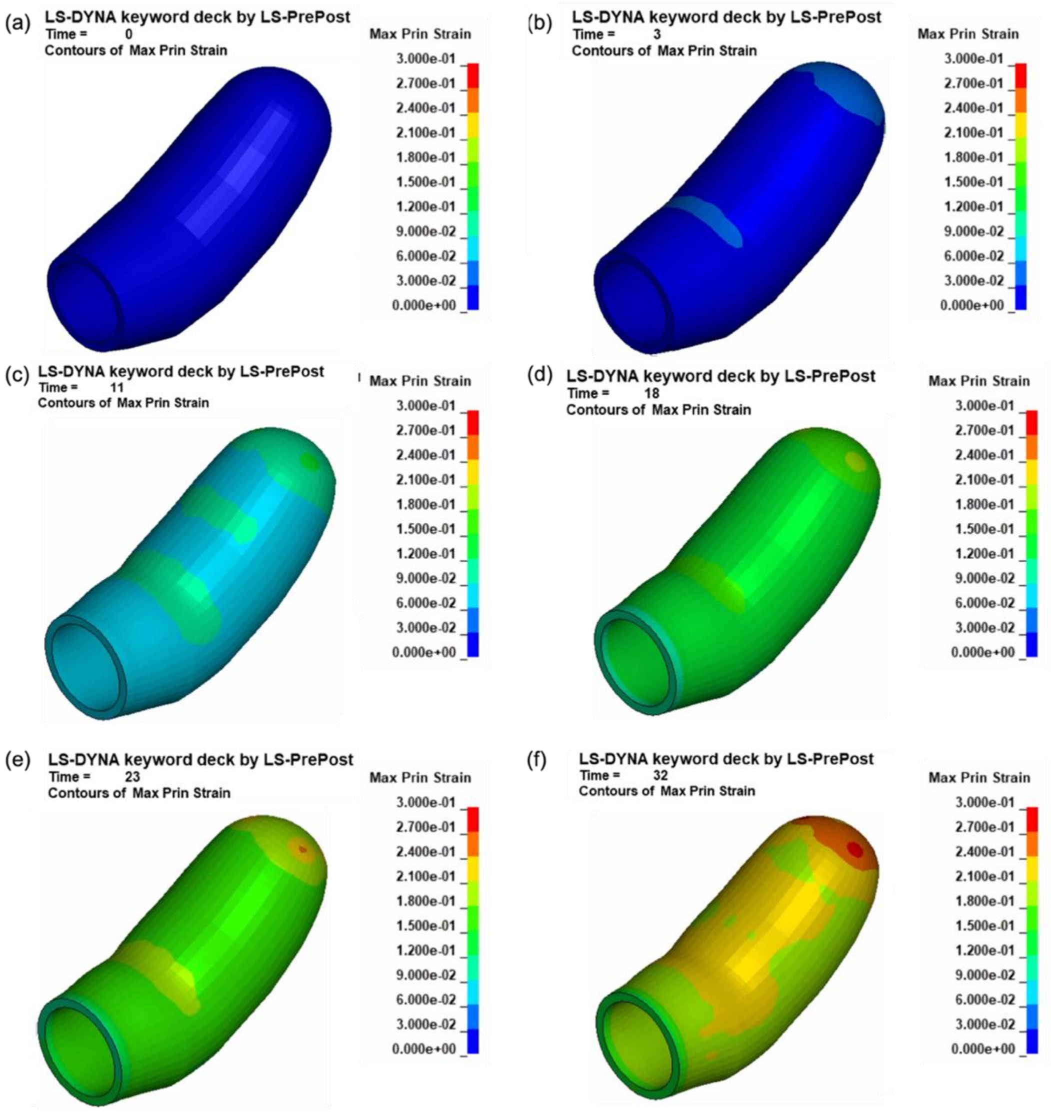

Figure 3.17, Simulation results of maximum principal strain with time for the longitudinal-Circumferential fibers model.

3.4.2 Active Contraction Behaviors of the Uterus and Fetus Delivery

3.4.2.1 Propagation of the Contraction Wave

The simulation results for the propagation of the contraction wave through the uterus are shown in Figure 3.18. Each row of images in Figure 3.18 represents a single contraction cycle in the model. For the first cycle (first row of Fig 3.18), there was no deformation at t = 0 s. After that, the uterus started to contract from the top of the fundus region and the contraction wave started to propagate to the lower portion of the uterus. By t = 2 s, the whole fundus region of the uterus had contracted. By t = 8 s, the first four regions had started to contract. By t =20 s, all of the seven regions within the uterus had contracted. Once the uterus reached the maximum deformation, the uterus started to relax due to the decrease of the activation level. The initial strain for the second and third contraction cycles was not zero because there was some deformation remaining from the previous cycle – the passive component of the tissue had not completely returned to its original state. Such a phenomenon occurred because the damping effect of the uterus (selected DMP value) required a longer time for the uterus to recover compared to the time before the beginning of the next contraction cycle. In each of the following cycles, a new contraction wave propagated to the lower part of the uterus. The overall strain on the uterus increased with the increase of the contraction cycles. The model successfully simulated the propagation phenomenon of the contraction wave within the uterus.

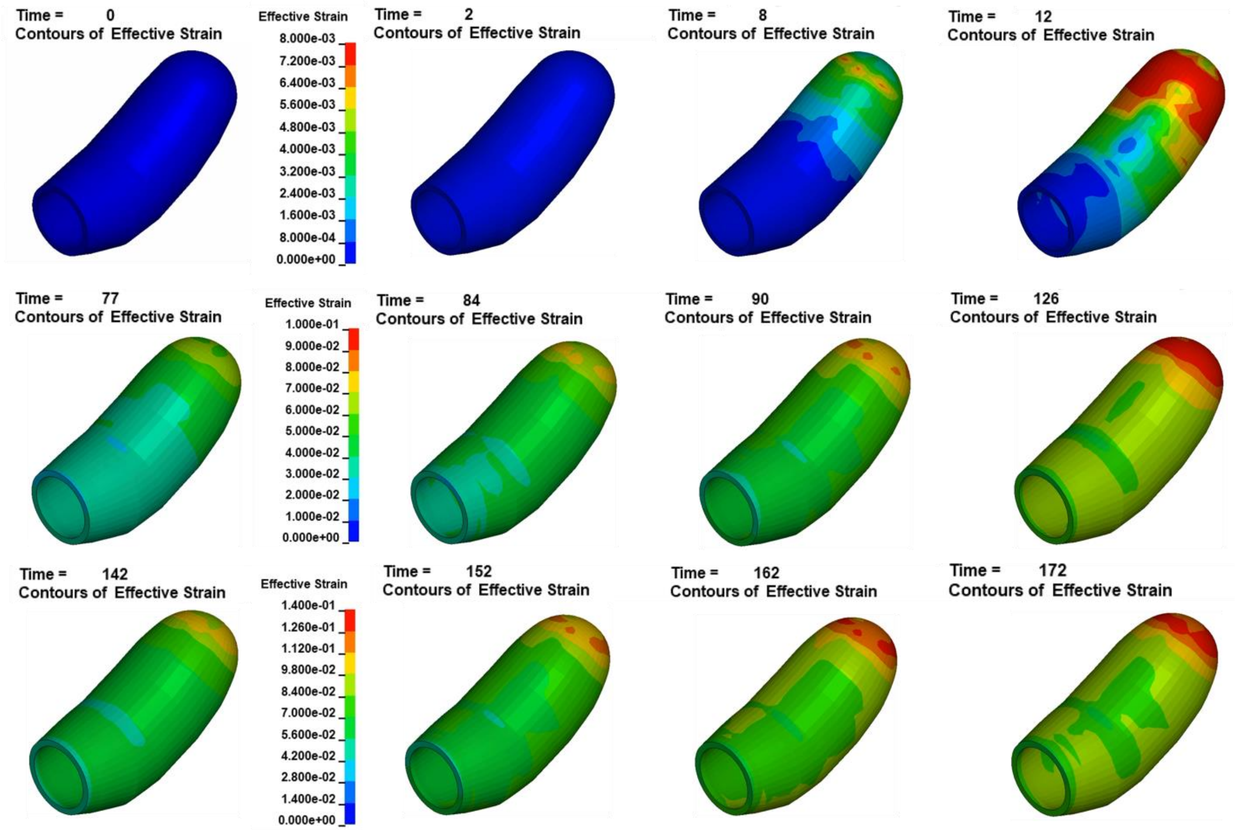

Figure 3.18, Propagation of the contraction wave for three contraction cycles.

3.4.2.2 The Element Stress and Stress Distribution within the Uterus

The stress within an element, picked in the fundus region of the uterus, and the distribution of the stress within the uterus through the three contraction cycles are shown in Figure 3.19. As the precise amount of stress cannot be validated against experimental data, the qualitative pattern of stress was the key result. The element stress increased significantly due to the rise of the activation level and decreased slightly due to the decline of the activation level within each cycle (Fig 3.19a). The element stress continued to increase with the number of contraction cycles (Fig 3.19a). For the distribution of the stress within the uterus, the stress was almost evenly distributed for the middle and lower parts of the uterus, while the largest stress occurred in the fundus region (Fig 3.19b).

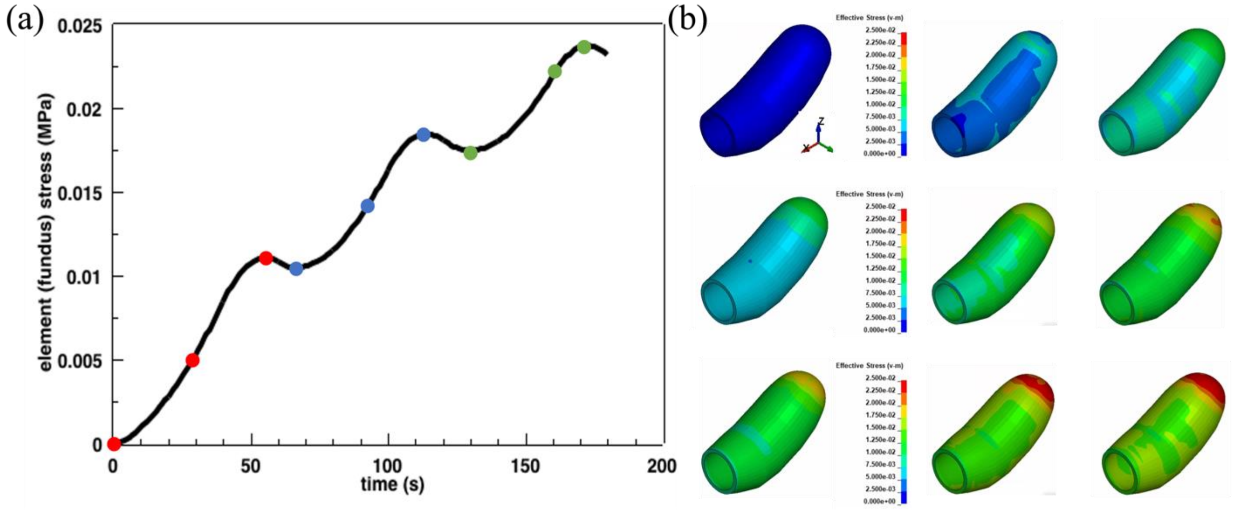

Figure 3.19, Stress for an element in the fundus region (a) and stress nephogram for the uterus (b), with a scale bar of 0 – 0.025 MPa. The three red points in (a) represented the three time points for the stress nephogram for the uterus for the first cycle (first row in (b)). The three blue and three green points were the time points picked for the second and third cycle, respectively.

3.4.2.3 Parametric Analysis

The mechanical responses of elements in different positions of the uterus during the simulation were investigated. Three elements, in the fundus, middle, and lower position of the uterus (Fig 3.20), were picked. The element in the fundus region had the largest displacement while the elements in the middle and lower positions had the second and smallest displacement during the contraction, respectively (Fig 3.21a). The element in the fundus region had much larger stress and strain compared to the elements in the middle and lower positions (Fig 3.21 b & c). The middle element had slightly larger stress and strain compared to the element in the lower position (Fig 3.21 b & c). In addition, there were phase delays for the three curves in each part of Figure 3.21 because the contraction happened first in the top region of the uterus and then propagated to the middle and lower parts.

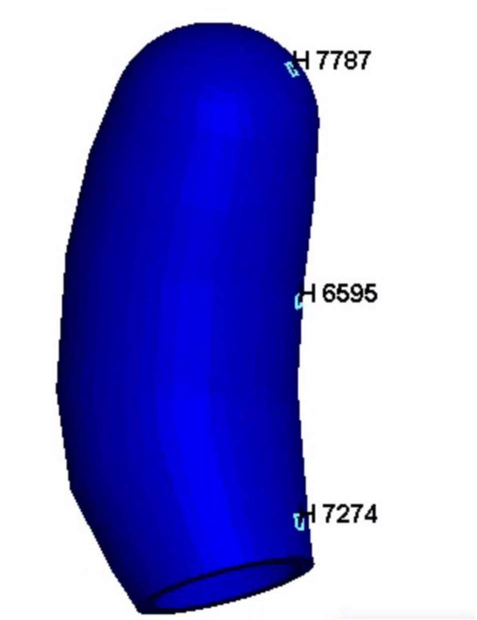

Figure 3.20, The chosen three elements in the fundus, middle and lower part of the uterus.

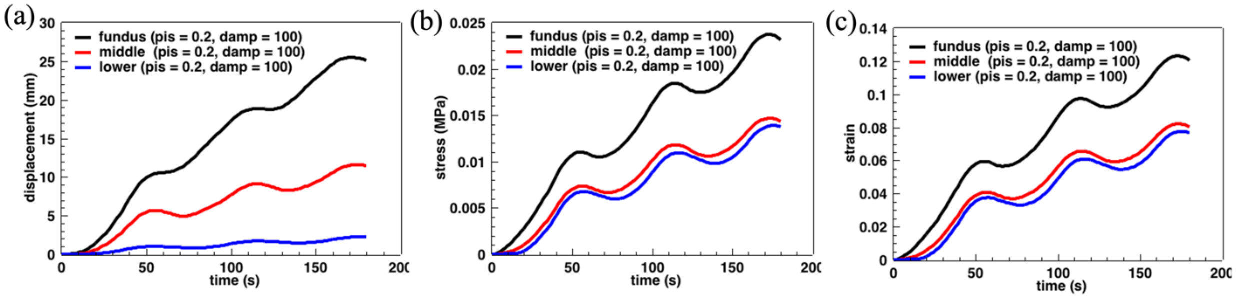

Figure 3.21, Curves of displacement (a), stress (b), and strain (c) for elements in fundus, middle, and lower positions of the uterus.

As in the previous assessment of the muscle contracting unit in Chapter Two, the PIS and DMP values in the Hill material model were found to significantly affect the contraction behaviors of the uterus. The results for the element in the fundus region were taken as an example. For the same PIS, the contraction velocity (the slope of the displacement vs time curve) decreased with an increase of the DMP value (Fig 3.22a). For the same DMP value, the largest displacement of the element in the fundus -- representing the contraction capacity or largest deformation of the uterus, the contraction velocity, and the element stress and strain increased significantly with an increase of PIS (Fig 3.22). The larger DMP was found to cause a longer time delay for the elements to reach their largest contraction responses for the same PIS. This can be demonstrated by the fact that the displacement, along with the element stress and strain, reached their maximum values quickly in the first contraction cycle for the smallest DMP, while they continued to increase in the second and third contraction cycles for larger DMP cases (Fig 3.22). The elements in the middle and lower positions had similar results (Fig 3.23).

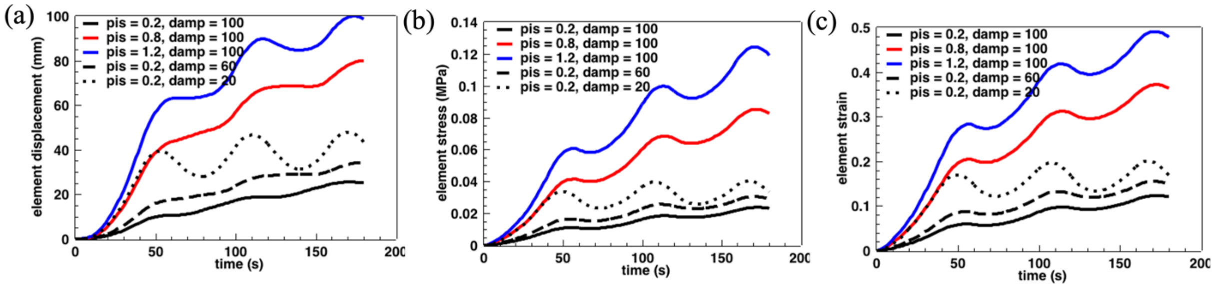

Figure 3.22, Effects of parameters (PIS & DMP) on element’s displacement (a), stress (b) and strain (c) for the element in fundus position.

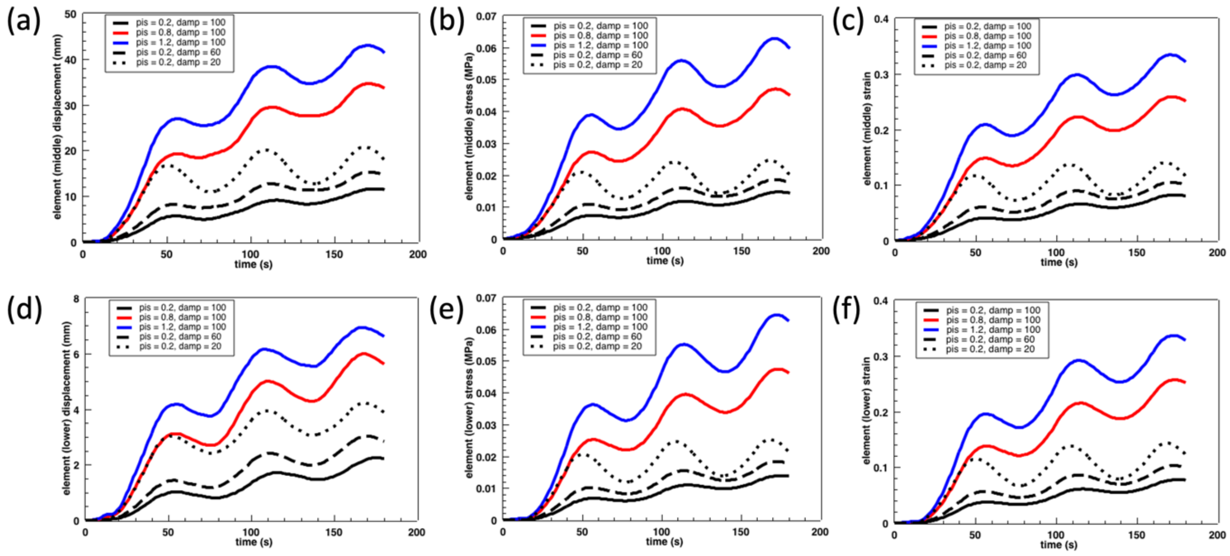

Figure 3.23, Effects of parameters (PIS & DMP) on element’s displacement, stress and strain for elements in middle (a, b & c), and lower position of the uterus (d, e & f).

In conclusion, the mechanical responses of the elements varied in different positions within the uterus. The elements in the fundus region had larger displacements along with larger stress and strain values than elements in the lower part of the uterus. There was a delay for such responses in the lower elements due to the propagation of the contraction wave that was initiated from the top region (fundus) of the uterus. In addition, the contraction capacity, or the largest deformation that a uterus can develop, was mainly controlled by the PIS parameter while the contraction speed was mainly controlled by the DMP parameter.

3.4.2.4 Delivery of the Fetus

The simulation results of the fetus delivery caused by the contraction of the uterus are shown in Figure 3.24. The uterus contracted significantly and relaxed slightly in each contraction cycle, but the overall uterine deformation increased with simulation time. In this version of the model, the fetal head was smaller than the outlet of the uterus – so no stretch to this region of uterine tissue occurred. In addition, the fetal model was simplified as a rigid body, so that no deformation occurred to any portion of the fetus. The contact between the uterus and the fetus was a surface-to-surface contact with no friction defined.

According to the mechanical process of labor, the movement of the fetus is mostly caused by the pushing force from the active contraction of the uterus with help from a maternal pushing force acting within the mother's abdomen[40]. The current model has not considered the effect of maternal pushing, which would add an effective outward force acting from the fundus. The sole source of the pushing force from the uterus in this simulation was the active contraction forces caused by the contractile fibers inside of the uterine wall. The contraction within the uterus did not happen in all regions simultaneously but resulted from a contraction wave that initiated from the top region and propagated to the lower part of the uterus, as represented in the model. The fetus started to move at t = 2 s when the inner surface of the uterus started to contact the fetal body. The contraction of the uterus and accumulated uterine deformation in the longitudinal direction through the three contraction cycles pushed the fetus to move downward through the uterus. At t = 180 s, the fetus' head and neck were delivered out of the uterus. The largest element stress and strain values were 0.13 MPa and 50.23% at the top of the fundus through the 3 cycles. The overall displacement of the fetus was around 175 mm at the end of the simulation.

The results of this model simulating the delivery of a fetus from a uterus by the uterine active contraction has demonstrated that bonding the three-dimensional contractile fibers with a solid portion of the uterine muscle wall can simulate the uterine active contraction successfully. In this case, the uterus contracts actively without the need for any external loading – which aligns with what is observed clinically. The model was able to produce a large enough deformation to push the fetus to move through the uterus.

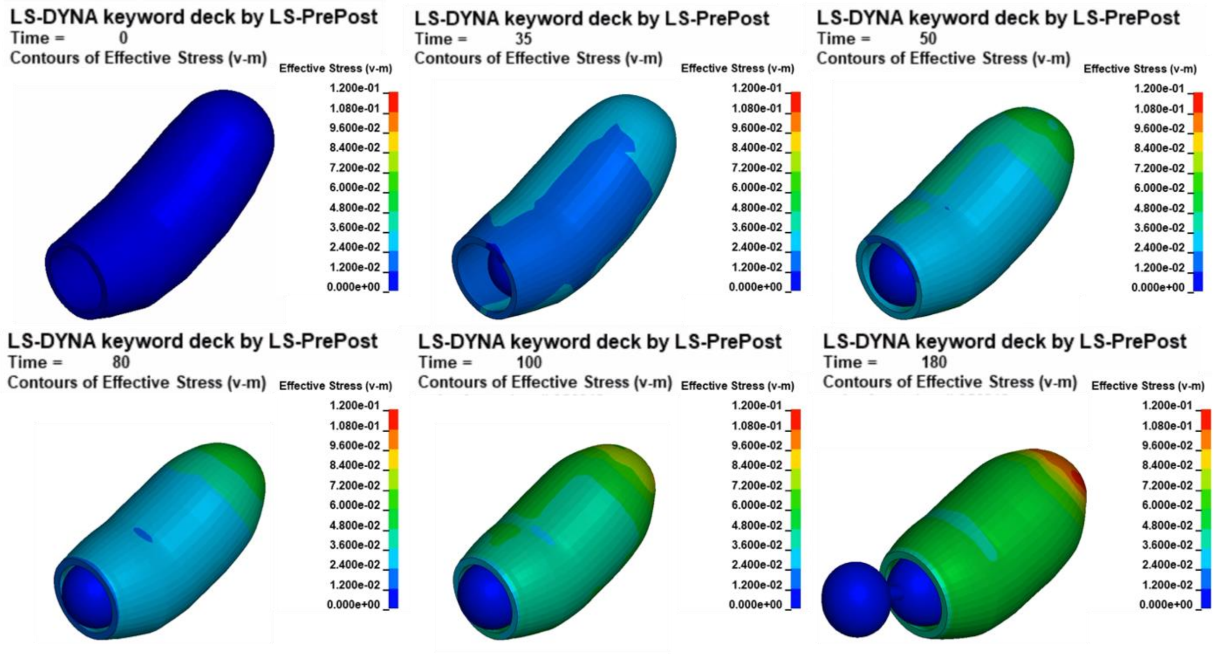

Figure 3.24, The delivery of the fetus through the uterus.

3.4.2.5 Validation of Uterine Model

As is typically true for models related to childbirth, direct validation of this model is difficult as the necessary parameters cannot be safely measured during childbirth. Thus, phenomenological validation and verification were used to confirm that the model is behaving in a manner that matches clinical observations. First, the value of the stress was higher in the fundus region as shown in Figure 3.24, which agrees with experimental findings that the intensity of the uterine contraction is stronger in the top region of the uterus [23]. Second, according to clinical data, the time period for the second stage of labor varies between 2 minutes and 200 minutes. In this model, the delivery time was 3 minutes. Finally, the propagation time of the contraction wave was 12 seconds (first row of Fig 3.18), which also agreed with experimental data [23] and previous simulation results [67,68].

3.5 Discussion

In this chapter, we developed a uterus FEM model with contractile fibers. Our model can simulate active uterine contraction directly rather than applying external loading conditions. Existing multi-scale electro-mechanical coupling models are usually mathematically complex, physiologically complicated, and computationally intensive [67], and therefore they would need an extremely large amount of computer memory and high computational speeds to predict macro-level mechanical behavior. Due to these challenges, these models have been implemented with highly simplified geometries and were not able to simulate large deformations that are necessary to deliver a fetus. In contrast, our model can perform large deformation simulation on a complicated geometry.

It is known that the variation of the fibers' orientation through the muscle thickness has a significant effect on uterine behavior [19]. The fibers inside of the uterus in the model were three-dimensional and divided into seven regions, therefore, it is very flexible in its ability to investigate the effects of the strong anisotropy and heterogeneity of fiber distribution on the mechanical behaviors of the uterus, which is better than the model with 2D evenly distributed fibers within the uterus [22]. Based on the simulation results of effects of combinations of fibers in different directions on the uterine contraction pattern, it was demonstrated that the normal direction fiber can affect the element stress and strain within the uterine wall significantly which means it is necessary to model the fibers in three dimensions. Also, the model can simulate the uterine contraction wave propagation from the fundus region to the lower parts of the uterus. In the simulation results, the fundus region had higher stress in the model, which matched with the experimental finding that the contraction intensity was higher in the fundus area than in the middle and lower part of the uterus [23]. The PIS and DMP parameters in the Hill model can significantly influence the mechanical behaviors of the uterus. Unlike many other simulation models in the literature where the movement of the fetus was imposed as a specific trajectory, the delivery of the fetus in this model was caused by the uterine active contractions without any prescribed curves for the fetus to move along.

3.6 Conclusion

In conclusion, a FEM model to simulate uterine cyclic active contraction driven by three-dimensional contractile fibers and capable of delivering a fetus was developed in LS-DYNA. In this model, the uterus was able to represent the anisotropy of the fiber distribution and perform the large deformation, cyclic active contraction, and propagation of the contraction wave needed to achieve fetal delivery. The ability to phenomenologically model the labor and delivery process will increase our understanding of how variations in anatomy or the characteristics of labor might impact injury risk to both the mother and the infant. While not biofidelic on a micro or cellular level, this will be able to demonstrate whether or not the uterus – with variations in its physiological response – can appropriately cause the descent of the fetus through the birth canal. Future work will incorporate a bony pelvis and pelvic floor muscles with the uterine model so that a complete model system can be established to simulate the childbirth process.

CHAPTER 4: Simulation of Fetus Delivery through the Pelvic Structures

4.1 Abstract

Childbirth or labor, as the final phase of a pregnancy, is a biomechanical process that delivers the fetus from the uterus. It mainly involves two important biological structures, the uterus -- generating the expulsive force on the fetus -- and the pelvis (bony pelvis and pelvic floor muscles) -- resisting the movement of the fetus. The existing computational models developed in this field that simulate the childbirth process have focused on either the uterine expulsion force or the resistive structures of the pelvis, not both. An FEM model including both structures as a system was developed in this chapter to simulate the fetus delivery process in LS-DYNA. The uterine active contraction was driven by contractile fiber elements using the Hill material model. The passive portion of the uterus and pelvic floor muscles were modeled with Neo Hookean and Mooney Rivlin materials, respectively. The bony pelvis was modeled as a rigid structure. The fetus was divided into three components: the head, neck, and body. Three uterine active contraction cycles were modeled. The model system was validated based on multiple outputs from the model, including the stress distribution within the uterus, the maximum Von Mises and principal stress on the pelvic floor muscles, the duration of the second stage of labor, and the movement of the fetus. The developed model system can be applied to investigate the effects of pathomechanics related to labor, such as pelvic floor disorders and brachial plexus injury.

4.2 Introduction

Childbirth is a mechanical process that involves pushing forces -- produced by the uterus' active contraction, intrauterine pressure, and Valsalva (pushing) induced abdominal pressure -- that act against a resistance force created by the pelvic structures as the fetus passes through the birth canal [40]. The strong interaction of the uterus, the fetus, and the maternal pelvis results in both the normal cardinal movements of labor and abnormalities of descent. The latter, which can include shoulder dystocia (delay in delivering the shoulders after the head delivers) [119], can lead to a range of injuries to both the infant and the mother [120,121]. According to a one hospital's statistics in 2007, only fifty percent of 13991 women progressed through spontaneous labor to the point of delivery, while the rest required Caesarean section, augmentation, or induction [41].

Pelvic floor disorders (PFDs), which are a group of pathologies that predominantly become symptomatic in middle-aged and elderly women, are closely related to the fetal delivery process. The typical symptoms of PFDs include urinary incontinence, fecal incontinence, pelvic organ prolapse, and pelvic pain [52]. It is estimated that about one-third of adult women are affected by these conditions to varying degrees [32]. Studies have shown that about 30% to 40% of women suffer from some degree of urinary incontinence during their lifetime [122], and 11% of women have required surgery because of pelvic organ prolapse or urinary incontinence [123]. Childbirth through vaginal delivery has been identified as the primary factor in the development of PFDs [52]. For example, Dimpflet *et al*. proposed that pelvic floor injuries during childbirth can significantly contribute to the development of PFD [124] because, during delivery of the fetus, the pelvic muscle floor experiences extreme stress and strain conditions that are believed to be the cause of the damage of these key structures. However, understanding of the mechanisms of damage to the pelvic floor is still limited [125].

Due to clinical, technical, and ethical reasons, *in vivo* investigation during pregnancy and delivery is limited. Computational models have been developed to simulate the process of childbirth [126] – but they generally have focused on either the uterine expulsion force or the resistive structures of the pelvis, not both.

For example, several simulation models have been developed to investigate the mechanical interactions of the fetal head and the pelvic muscle floor during the passage of the fetus through the vagina, with the purpose of exploring the mechanisms of PFD [52,127]. Stress and strain fields, reaction forces, and deformation have been calculated and analyzed in these simulations. The geometries commonly include the bones of the pelvis, the pelvic muscle floor, and the fetal head. For the fetal head, some studies used a sphere to represent the structure, while others used more realistic fetal skull geometry obtained from MRI data. The effect of variations in the material properties of the fetal head on the deformation of the pelvic muscle floor has been investigated. A rigid fetal head was found to cause higher stretch and reaction forces in the pelvic floor muscles than a deformable fetal head [128]. The geometries of these structures [51] and the material parameters of the constitutive models [50] for both the pelvic floor muscles and the fetal head have an impact on the calculated results in such simulations. In these models, one challenge is to consider – appropriately and accurately – all forces that act during the fetal delivery process, such as the expelling forces acting on the fetus caused by uterine active contraction. However, in these pelvic models, the uterus and uterine active contraction were not included in the simulations. Instead, the fetus's movement or trajectory through the pelvic structures were simulated by applying kinematic boundary conditions to the fetus.

The uterus-only models simulating uterine active contraction [54,96] have not to date considered the strong resistance force caused by the pelvic muscle floor and bony pelvis as the fetus passes through the birth canal during the second stage of labor. For this reason, the calculated deformation, stress and strain field, and other analysis of these uterus-only models are not accurate and reliable.

Therefore, to better understand the pathomechanics of the childbirth process and explore the mechanisms of injuries to both the infant and the mother, it is quite important and necessary to model both structures of the pelvis (bony pelvis and pelvic floor muscles) and the uterus as a system. The objective of this Chapter was to develop a model of maternal tissues that could provide realistic expulsion and resistance forces to govern the movement of an infant through the birth canal. Through this study, stresses throughout the maternal and fetal models can be investigated.

4.3 Materials and Methods

The geometric models of the pelvic bone and pelvic muscle floor were created based on the in vivo MR images of a 21-year-old woman at the gestational stage of 35 weeks and 6 days. The pelvic bone includes the sacrum, the pubic symphysis of the bony pelvis, and the innominate bones (Fig 4.1). The pelvic muscle floor includes the levator ani, coccygeus, and the superficial perineal muscles and perineal membrane [129,130]. Figure 4.2 shows the overview of the pelvic muscle floor.

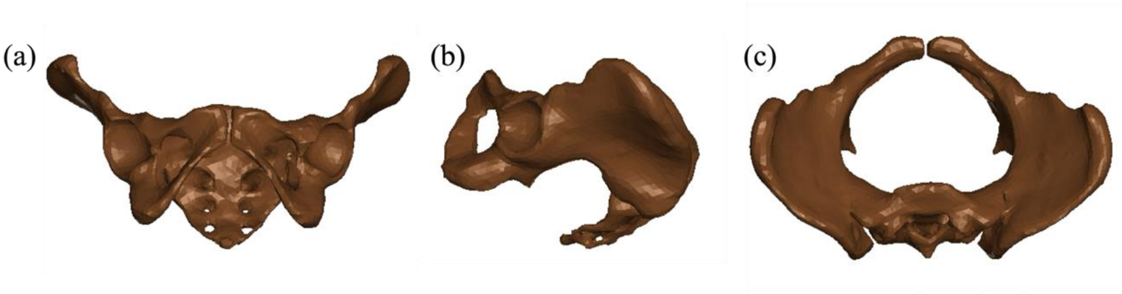

Figure 4.1, The geometric model of the pelvic bone from front view (a), side view (b), and top view (c).

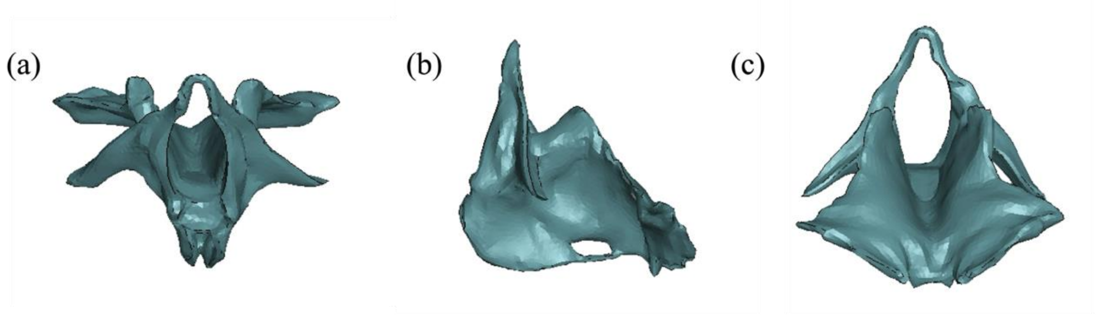

Figure 4.2, The geometric model of the pelvic muscle floor from front view (a), side view (b), and top view (c).

The geometries of the bony pelvis and the pelvic muscle floor were imported into Hypermesh for constructing the mesh. Triangular shell elements, with an average element size of 5 mm and a thickness of 1 mm were used for the maternal bony pelvis. Tetrahedral elements, with an average size of 4 mm, were used for the pelvic floor muscles. In total, the finite element mesh of the pelvic structures was composed of 15,077 triangular elements, and 14,130 nodes, as shown in Figure 4.3 and Figure 4.4. The bony pelvis was modeled as a rigid body. The pelvic muscle floor was modeled as a hyperelastic material with a Mooney Rivlin model (C1 = 0.016 MPa, and C2= 0.004 MPa) [127].

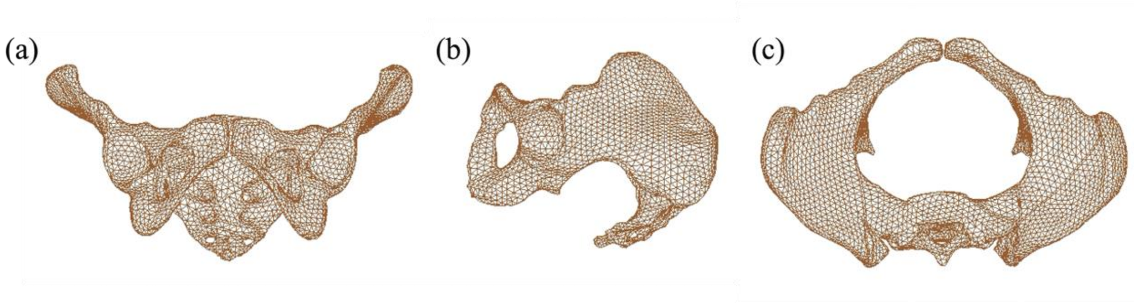

Figure 4.3, The mesh of the pelvic bone from front view (a), side view (b), and top view (c).

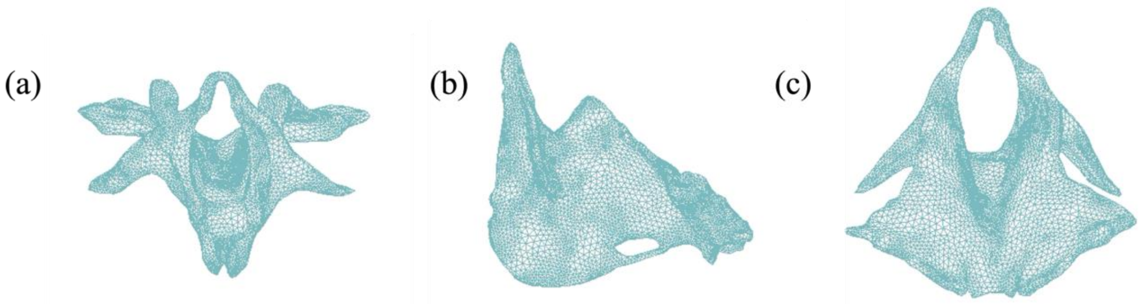

Figure 4.4, The mesh of the pelvic muscle floor from front view (a), side view (b), and top view (c).

The models of the bony pelvis and pelvis floor muscle were then incorporated with the uterus model and fetus model as developed in the previous Chapters. Figure 4.5 shows the combination of all these structures.

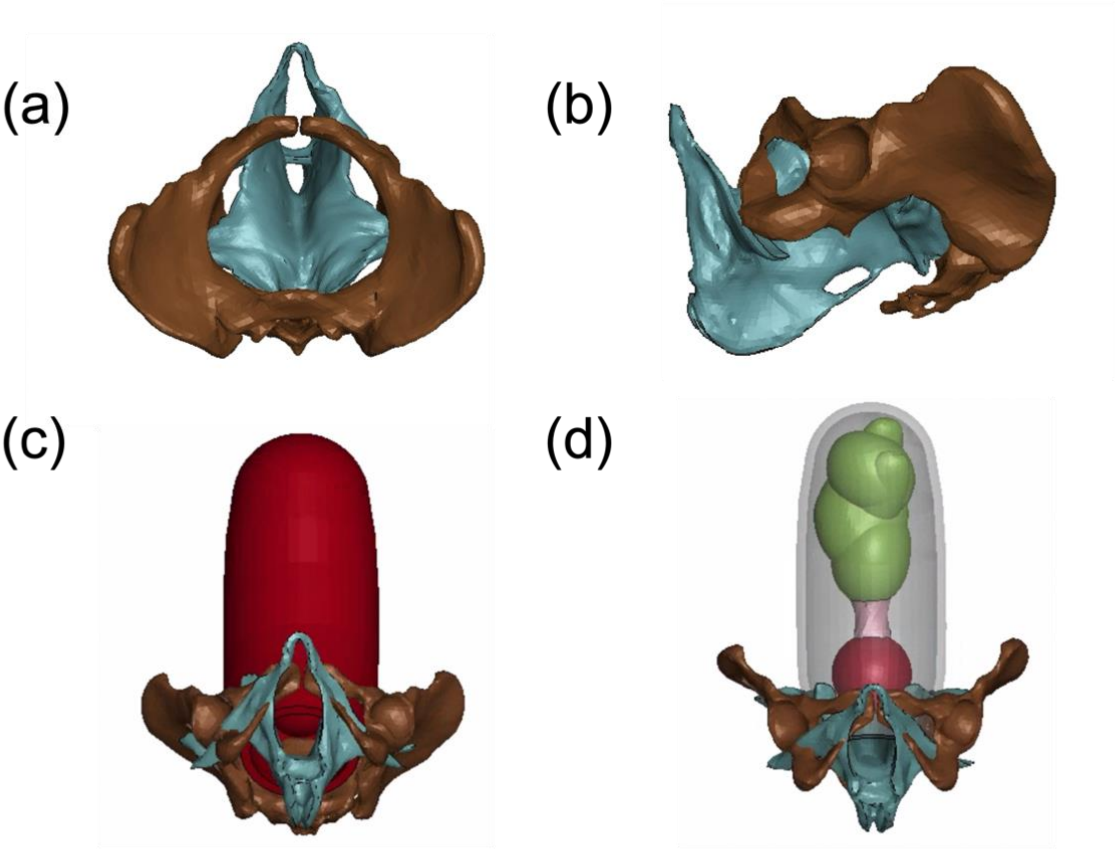

Figure 4.5, The geometries of the bony pelvis, pelvic muscle floor, fetus, and the uterus.

For the material properties, the fetus was modeled as three components – head, neck, and body – where the fetal head was a rigid body, the neck was elastic (E = 50 MPa, v = 0.49), and the body was Neo Hookean hyperelastic (C1 = 0.07 MPa [131]). The contact between the fetus and both the uterus and pelvic structures was modeled as a surface-to-surface contact. No external loads were applied. The material properties of the passive portion of the uterus, the fetus, and the pelvic structures are summarized in Table 4.1.

Table 4.1, Material properties for the uterus, fetus, and the pelvic structures.

Parts		Material Properties
Uterus (Passive Component)		Neo Hookean (C1= 0.03 MPa) [60]
Fetus	Head	Rigid body
	Neck	Elastic (E = 50 MPa)
	Body	Neo Hookean (C1 = 0.07 MPa) [131]
Pelvic Structures	Bony Pelvis	Rigid body
	Pelvic Floor Muscles	Mooney Rivlin (C1= 0.016 MPa C2= 0.004 MPa) [127]

For the boundary conditions, the cervix (Fig 4.6a) and bony pelvis were fixed in the x, y, and z translation directions in space. The nodes with colors on the pelvic floor muscles (Fig 4.6b) were fixed as well.

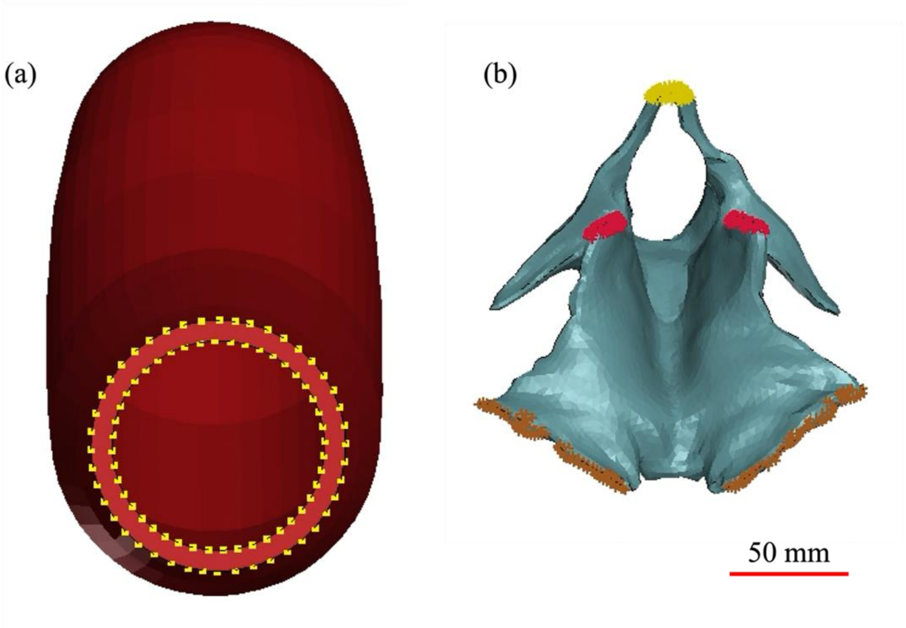

Figure 4.6, Boundary conditions of the cervix (a) and the pelvic floor muscles (b). A scale bar of 50 mm is provided.

The active contraction of the uterus was implemented, and the resulting movement of the fetal model through the pelvis was observed. In addition, the stress developed within the pelvic floor muscles and fetal neck and body were analyzed. The simulation results were reviewed to verify that the model was acting as expected. The model was then validated by comparing the simulation results with other childbirth modeling and experimental results in the literature, with details in the Results Section.

After validation of the model, the effects of the size of the fetal head on the mechanical behaviors (the Von Mises stress and maximum principal stress) of the uterus, fetal neck, and pelvic floor were investigated. Two fetal head sizes, 80 mm and 90 mm were used. Three elements -- in the uterine fundus, fetal neck, and pelvis floor muscles, respectively -- were chosen as key indicators of the response of the structures (Fig 4.7).

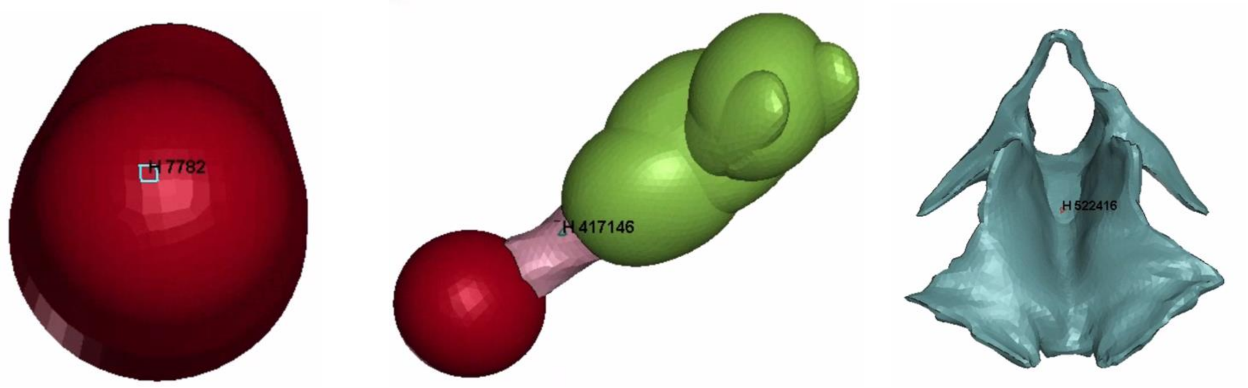

Figure 4.7, Three indicator elements within the fundus region of the uterus, the neck of the fetus, and the maternal pelvic floor muscles.

4.4 Results

4.4.1 Model Verification and Validation

Verification focused on two portions of the model: the uterus and the fetus. For the uterus, we examined whether the contractile behavior resembled normal physiology. For the fetus, we focused on whether the fetus would remain in a vertex presentation and descend through the maternal pelvis. Both of these expected behaviors were confirmed. The simulation results showing contraction of the uterus are provided in Figure 4.8. The uterus started to contract from the fundus region, and the contraction wave started to propagate to the lower part once the uterus was activated. By t = 30 s, all regions contracted, and the largest stress was 0.05 MPa at the top of the fundus area (Fig 4.8b). By t = 50 s, the stress for the different regions within the uterus each reached their maximum value (0.11 MPa) for the first contraction (Fig 4.8c), and then decreased slightly due to the decrease of the activation level in the first cycle – allowing relaxation of the uterus. After that, the stress increased again in the second contraction. The maximum stress for different regions within the uterus in the second cycle (0.14 MPa) (Fig 4.8d) was higher than that in the first cycle (Fig 4.8c). In this model, the largest stress within the uterus was always in the fundus region, which agreed with the experimental findings that the contraction intensity is higher in the fundus region [23].

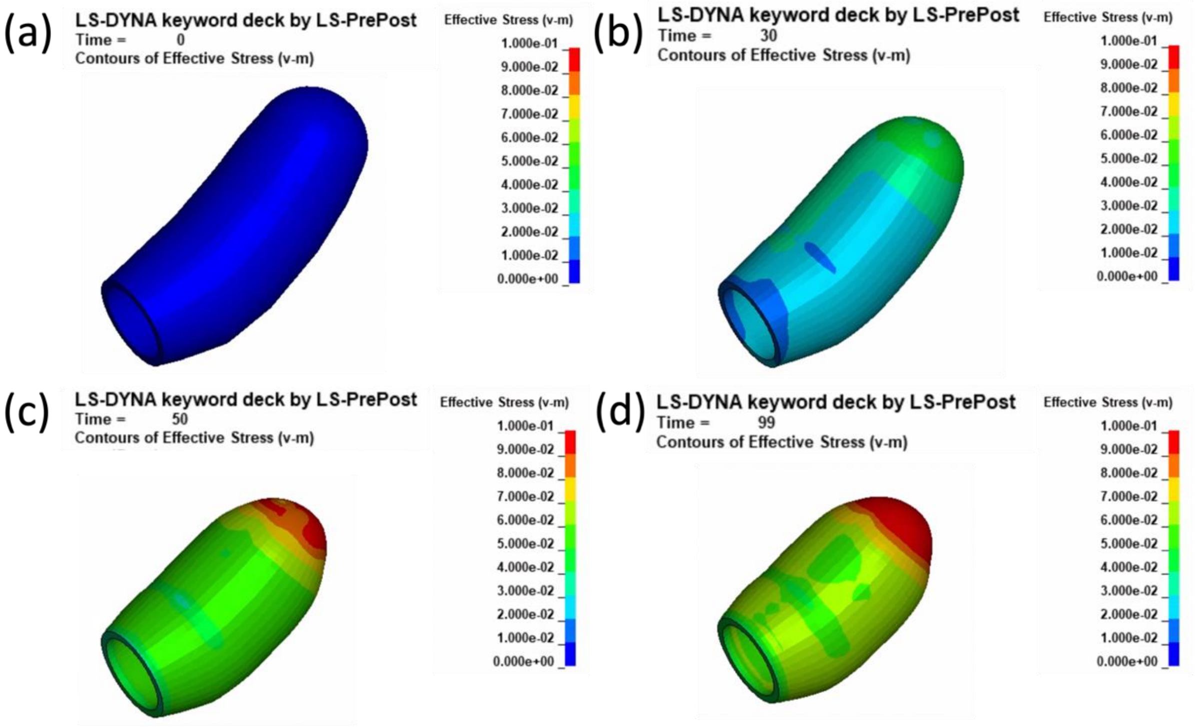

Figure 4.8, Representation of the deformation and stress for the uterus at times of 0 s (a), 30 s (b), 50 s (c), and 99 s (d). These were determined for the full model anatomy, including the pelvis and fetus.

The stain nephogram of the uterus is shown in Figure 4.9. The element strain of the uterus started to increase once the uterus was activated in the first contraction cycle. In parallel to the propagation of the stress wave, the strain within the uterus also propagated from the uterine fundus region to the lower part of the uterus. By t = 30 s, all regions contracted, and the largest strain was 25.3% at the top of the fundus area (Fig 4.9b). By t = 50 s, the strain for the different regions within the uterus each reached their maximum value (44.3%) for the first contraction (Fig 4.9c). The strain decreased then because of the decrease of the activation level in the first cycle, and increased again in the second contraction cycle. The maximum strain (54.5%) for different regions within the uterus in the second cycle (Fig 4.9d) was higher than that in the first cycle (Fig 4.9c). The largest strain within the uterus was always in the fundus region caused by the largest stress in the same region.

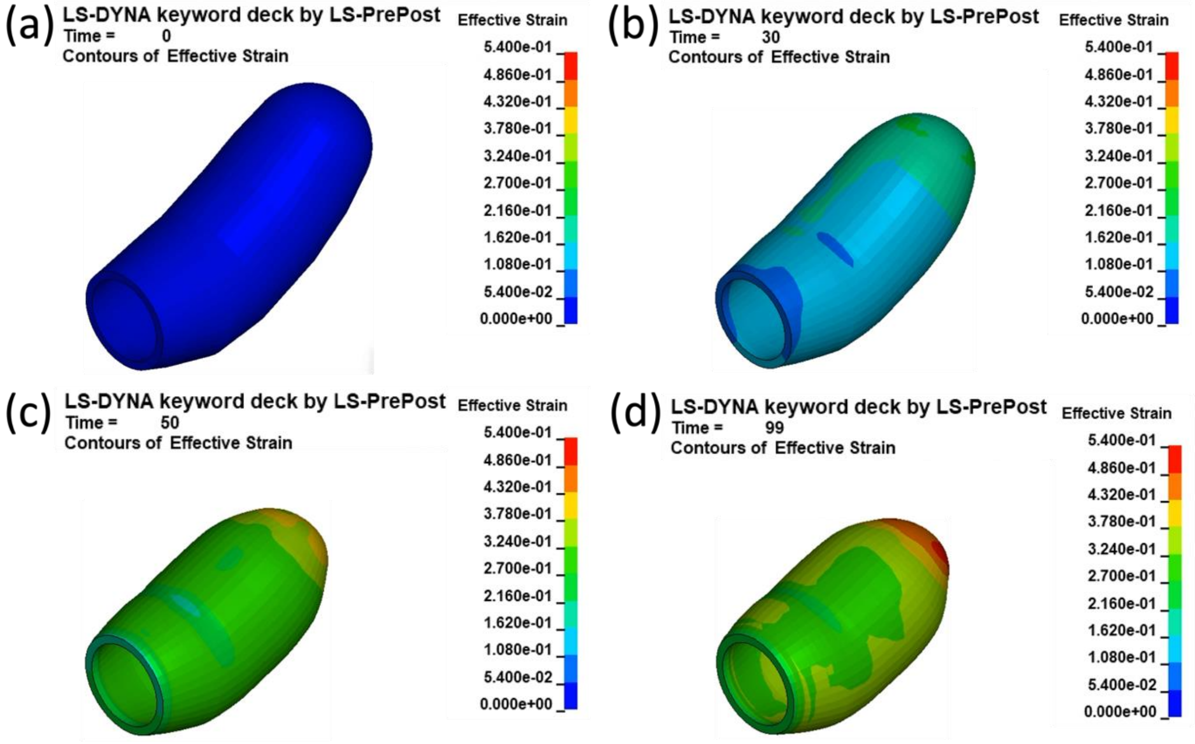

Figure 4.9, The strain nephogram for the uterus at times of 0 s (a), 30 s (b), 50 s (c), and 99 s (d).

The axial force of the fibers in the longitudinal direction is shown in Figure 4.10. The axial force was zero before the activation but started to increase from the fundus region and propagated to the middle and lower regions, which caused the propagation of the contraction wave within the uterus, after the initiation of the activation. The maximum axial force occurred at 50 s for the first contraction cycle, and the value was 12.57 N. The axial force decreased in the recovery phase for the first cycle until 70 s. The minimum value for the axial force was 1.02 N for the fibers at the lowest layer and the maximum value was 6.41 N for the fibers at the fundus region. The axial force continued to increase in the second contraction cycle until the delivery of the fetal head at 99 s. The maximum value was 17.67 N.

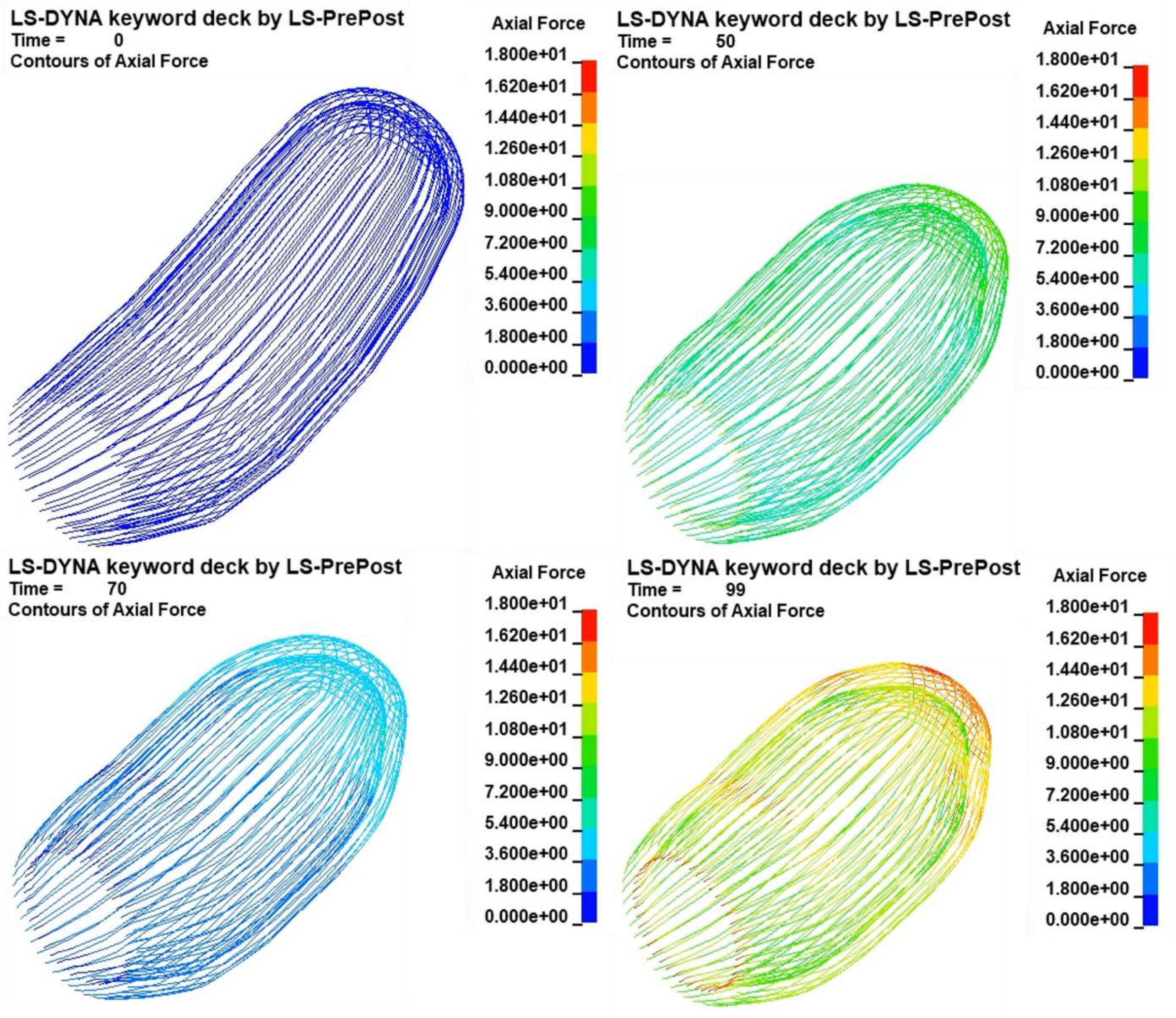

Figure 4.10, Axial force for the fibers in the longitudinal direction.

The axial force of the fibers in the circumferential direction is shown in Figure 4.11. Similar to the fibers in the longitudinal direction, there was also a propagation of the axial force from the top region to the lowest region. The maximum value of the axial force was 12.33 N at 50 s for the first contraction cycle for fibers in the fundus region. The axial force decreased in the recovery phase for the first cycle until 70 s. The maximum axial force was 20.55 N in the fundus region at 99 s in the second contraction cycle. The distribution of the axial force for the fibers in the circumferential direction was different from that of the fibers in the longitudinal direction. The axial force for the fibers in the circumferential direction was always larger in the fundus region during the first and second contraction cycles. This is because the percent fiber content for the fibers in the circumferential orientation was higher in the fundus region.

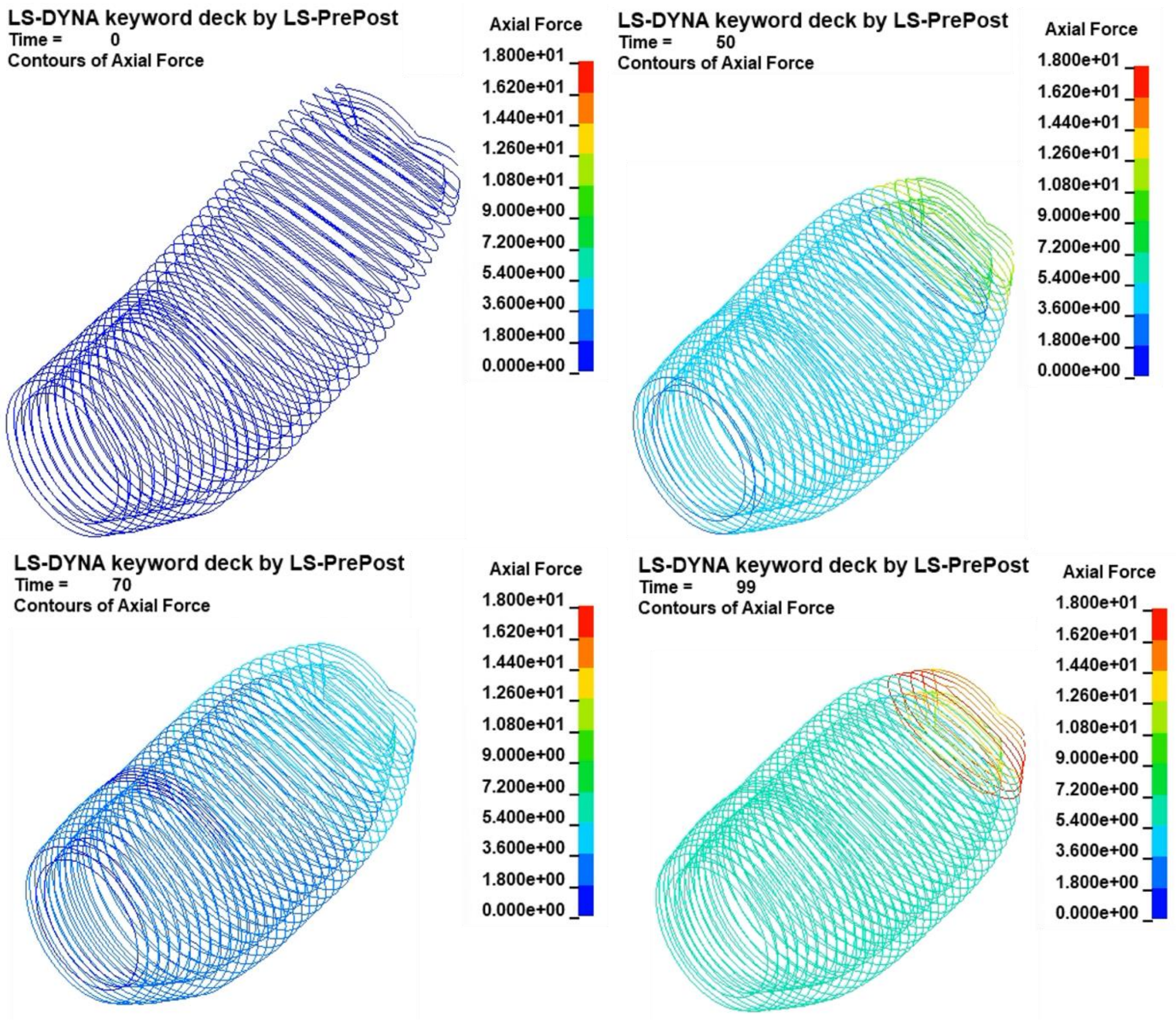

Figure 4.11, Axial force for the fibers in the circumferential direction.

The axial force of the fibers in the normal direction is shown in Figure 4.12. The maximum axial force was 6.03 N, and 1.42 N, 8.91 N at 50 s, 70 s, 99 s, respectively. Compared to the axial forces for the fibers in the longitudinal and circumferential directions, the maximum axial force for the fibers in the normal direction was much smaller because the fiber content of the normal direction fibers was smaller than that of the other two types of fibers. The distribution of the axial force for the normal fibers was almost the same as seen in the longitudinal fibers. This is because the fiber content for the normal fibers is the same among all regions of the uterus, which was also assumed for the longitudinal fibers.

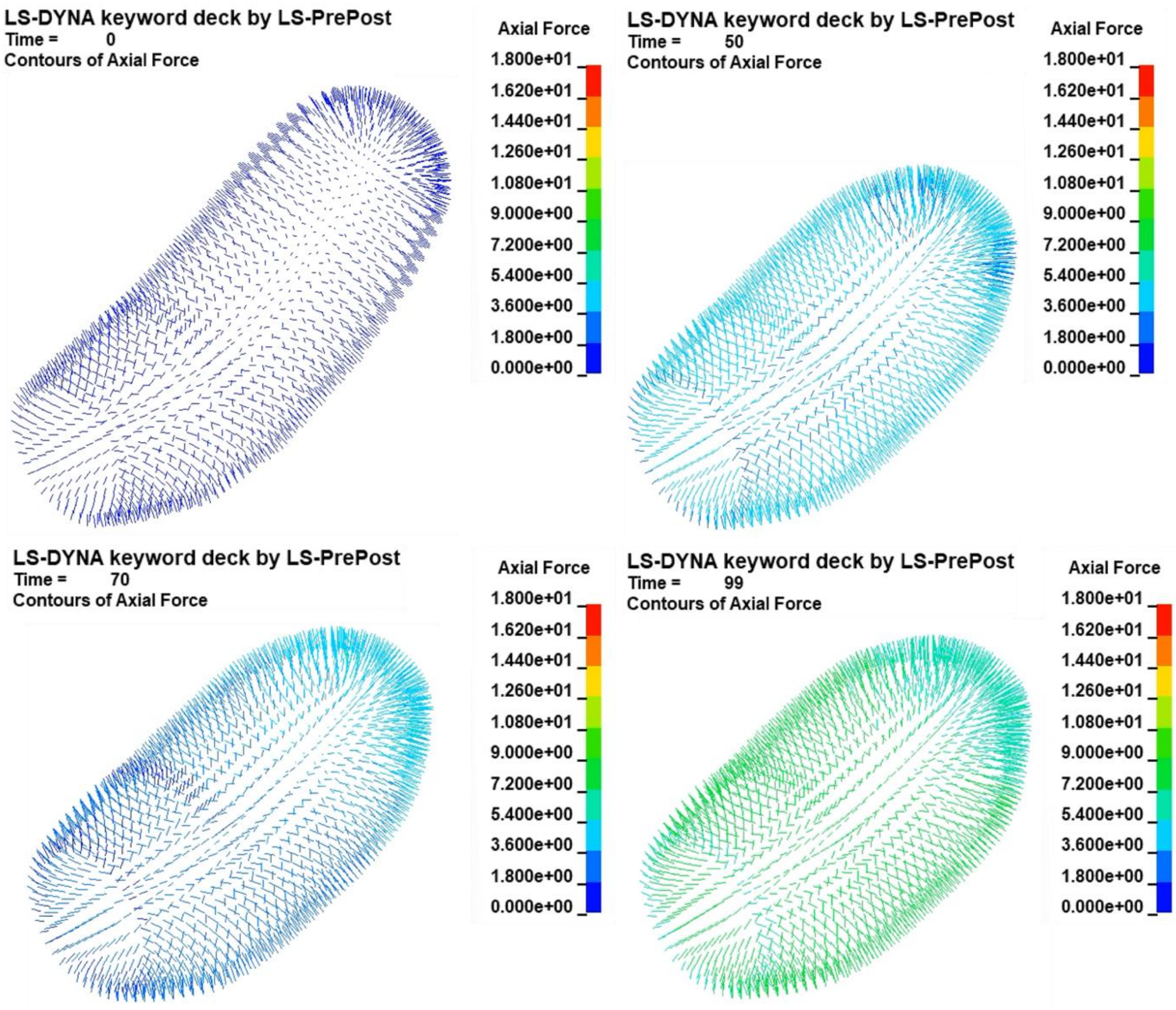

Figure 4.12, Axial force for the fibers in the normal direction.

The Von Mises stresses for the pelvic floor muscles are shown in Figure 4.13. At time = 30 s, the largest stress of the pelvic floor muscles was 0.03 MPa (Fig 4.13b). As the fetus continued to move forward, the stress within the pelvic floor muscles became much larger. At time = 50 s, the largest stress was 0.06 MPa (Fig 4.13c). The maximum Von Mises stress was 0.11 MPa at 98 s, occurring at the mid-point in the second cycle, right before the fetal head delivered (Fig 4.13d). The maximum principal stress was 0.12 MPa at an element in the center line of the pelvic floor muscles. To validate the simulation results of the pelvis structure, the values of the Von Mises stress and the maximum principal stress were compared with similar modelling work where the stresses of the pelvis floor muscles were analyzed when the fetal head passed through [5]. Specifically, in their work, the effects of the size of the fetal head on pelvic floor muscle stress were investigated [52]. The maximum Von Mises stress and maximum principal stress calculated by previous researchers were 0.149 MPa and 0.117 MPa, respectively, for the 80 mm fetal head case, located in the center line of the pelvic floor muscles [52]. In comparison with Xuan's work, the predicted values from the current model for Von Mises stress (0.11 MPa) and principal stress (0.12 MPa) of the pelvic floor muscles, as well as the locations where those stresses occurred, are very close.

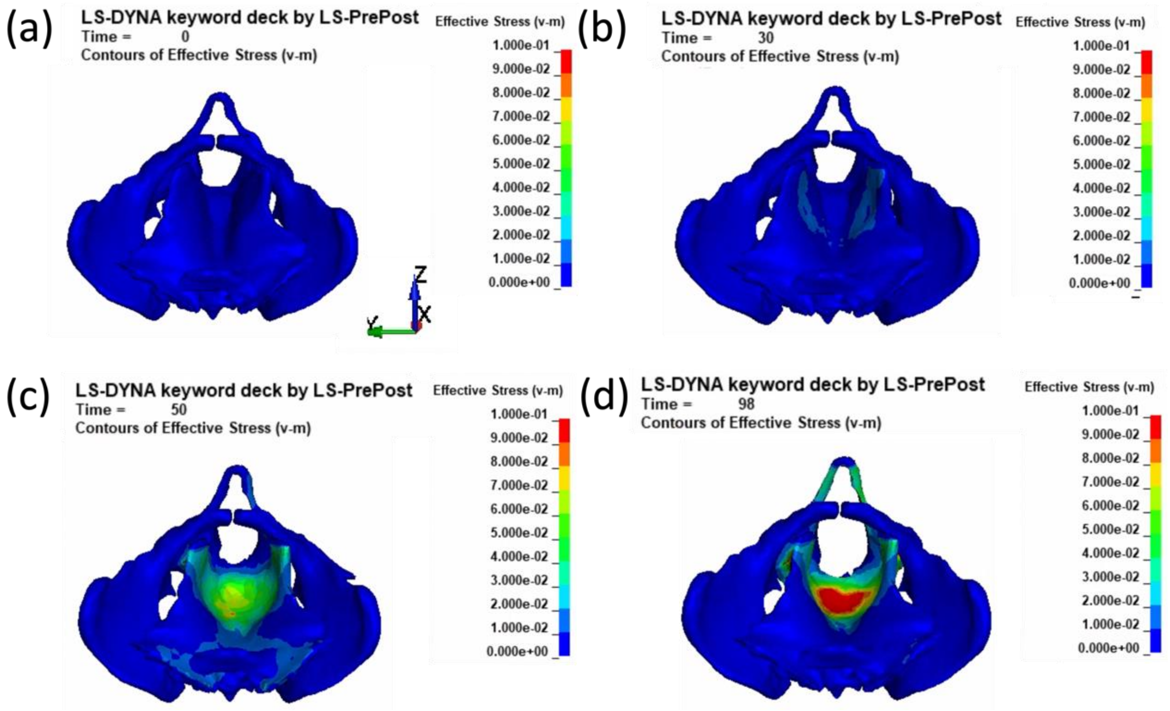

Figure 4.13, Stress nephogram of the pelvis muscle floor at times of 0 s (a), 30 s (b), 50 s (c), and 98 s (d).

The strain for the pelvic floor muscles is shown in Figure 4.14. There was no strain or stress within the bony pelvis structure as it was a rigid body. The strain in the pelvic floor muscles was zero until the fetus started to contact these structures. At time = 30 s, the largest strain of the pelvic floor muscles was 19.7% (Fig 4.14b). The strain within the pelvic floor muscles continued to increase as the fetus moved through. At time = 50 s, the largest strain was 78.4% (Fig 4.14c). The maximum Von Mises strain was 123.9% at 98 s, occurring at the mid-point in the second cycle, right before the fetal head was delivered (Fig 4.14d). The distribution of the strain was almost the same as that of the stress, which was concentrated in the midline of the pelvic floor muscles.

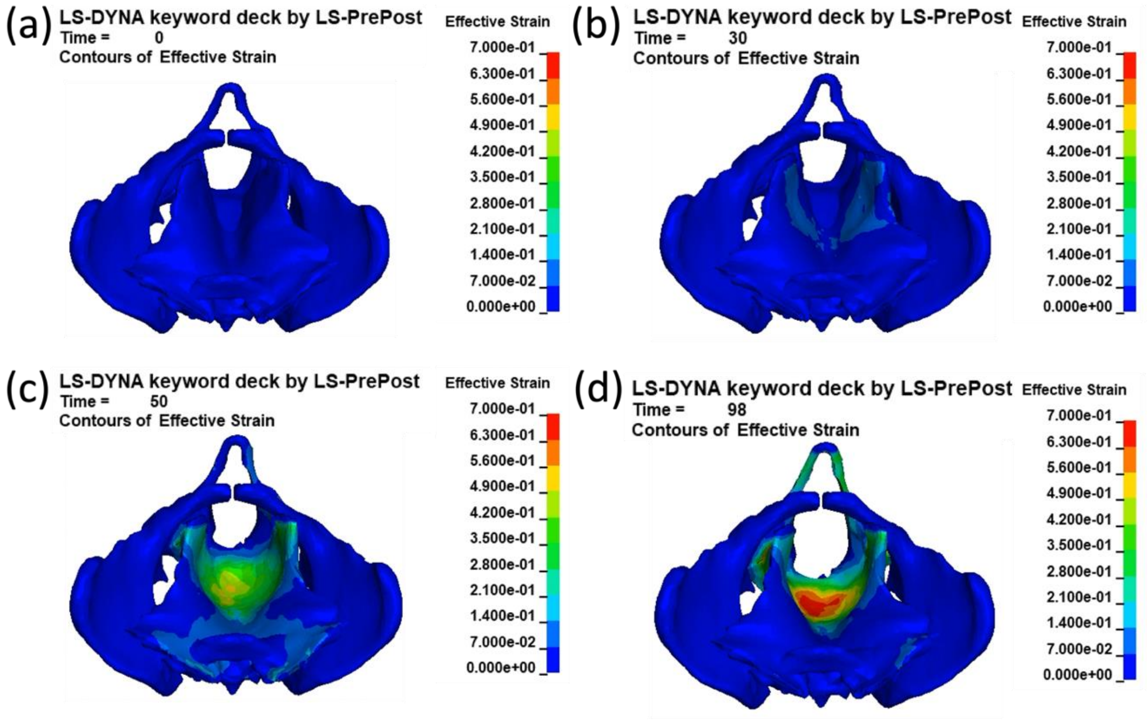

Figure 4.14, Strain nephogram of the pelvis muscle floor at times of 0 s (a), 30 s (b), 50 s (c), and 98 s (d).

The fetal displacement with time during the delivery process is shown in Figure 4.15. The contraction of the uterus pushed the fetus forward through the pelvic structures. The fetus naturally rotated in a clockwise direction in the sagittal plane of the pelvis as it moved through the birth canal. The outward displacement continued to increase until 50 s in the first contraction, then decreased slightly in the first recovery phase, and increased again in the second contraction cycle. The fetal head was delivered during the second contraction. The overall displacement of the fetus during the delivery process was about 320 mm. The delivery time of the fetus in the model was validated in comparison to clinical data. In clinical deliveries, the duration for the second stage of labor varies significantly – from 2 min to 200 min [118]. In this current version of the model, it took 100s for the fetus to deliver, which was close to that lower bound of 2 min. While this represents an extremely precipitous delivery – a second stage that includes only two contractions – the displacement of the fetus within the birth canal and pelvis are representative of the normal clinical movement. More importantly, by increasing the damping coefficient (DMP) value within the Hill model, the delivery process can be slowed down and the number of contractions and time of the second stage can be increased.

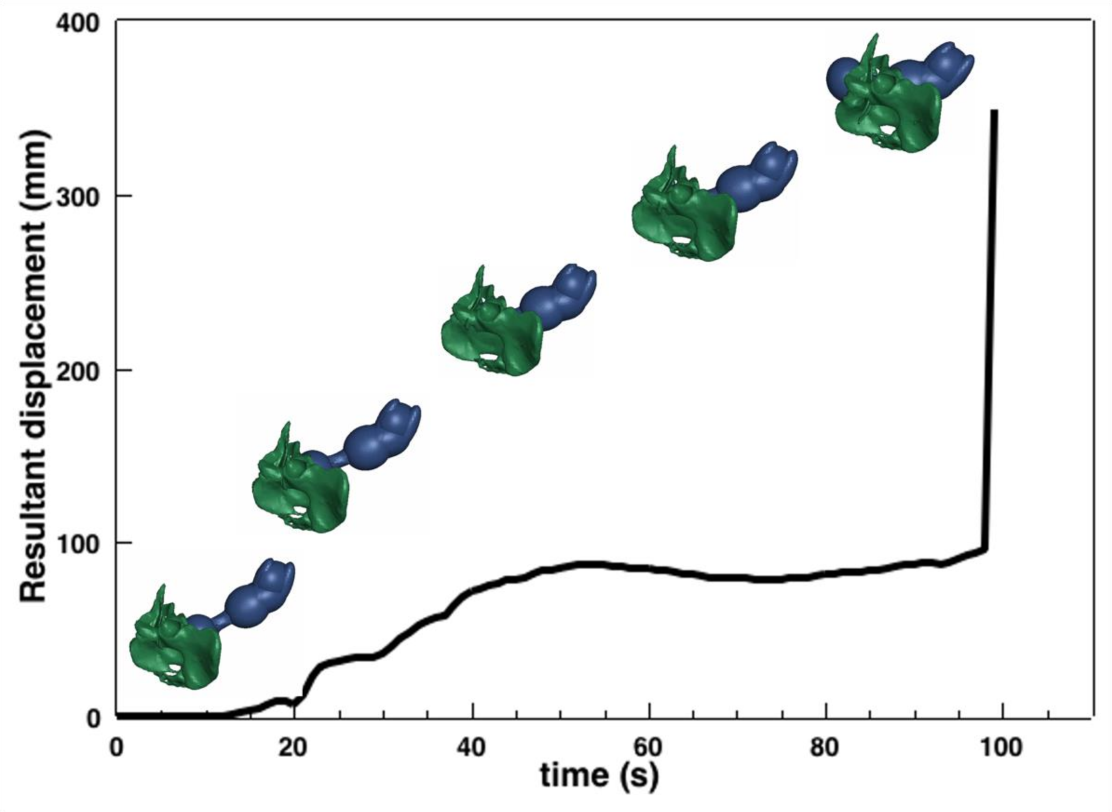

Figure 4.15, Displacement of fetus during the delivery process.

The stress experienced by the fetus during the delivery process is shown in Figure 4.16. The overall stress within the fetus increased until 50 s (Fig 4.16c), then decreased in the first recovery phase (Fig 4.16d) and finally continued to increase again in the second contraction cycle until the delivery of the head (Fig 4.16f). The stress was concentrated in the fetus' neck and was much larger than the stress predicted in the fetus' body. The highest value of the stress was 0.13 MPa, 0.85 MPa, 0.59 MPa, 0.93 MPa, and 1.12 MPa at time points of 30 s, 50 s, 70 s, 98 s and 99 s, respectively. Figure 4.16 also shows the rotation of the fetus during the delivery, and this is the rotation angle that was used as an index for validation. By comparing the initial and the last position of the fetus, the spine of the model fetus rotated 46 degrees within the mother's sagittal plane, which is quite close to the fetus' rotation angle of approximately 45 degrees during the cardinal movements of labor that span from the completion of internal rotation to the end of restitution [132]. The rotation in this model is solely the result of the interaction of the fetus with the bone and soft tissue structures of the pelvis – it was not prescribed.

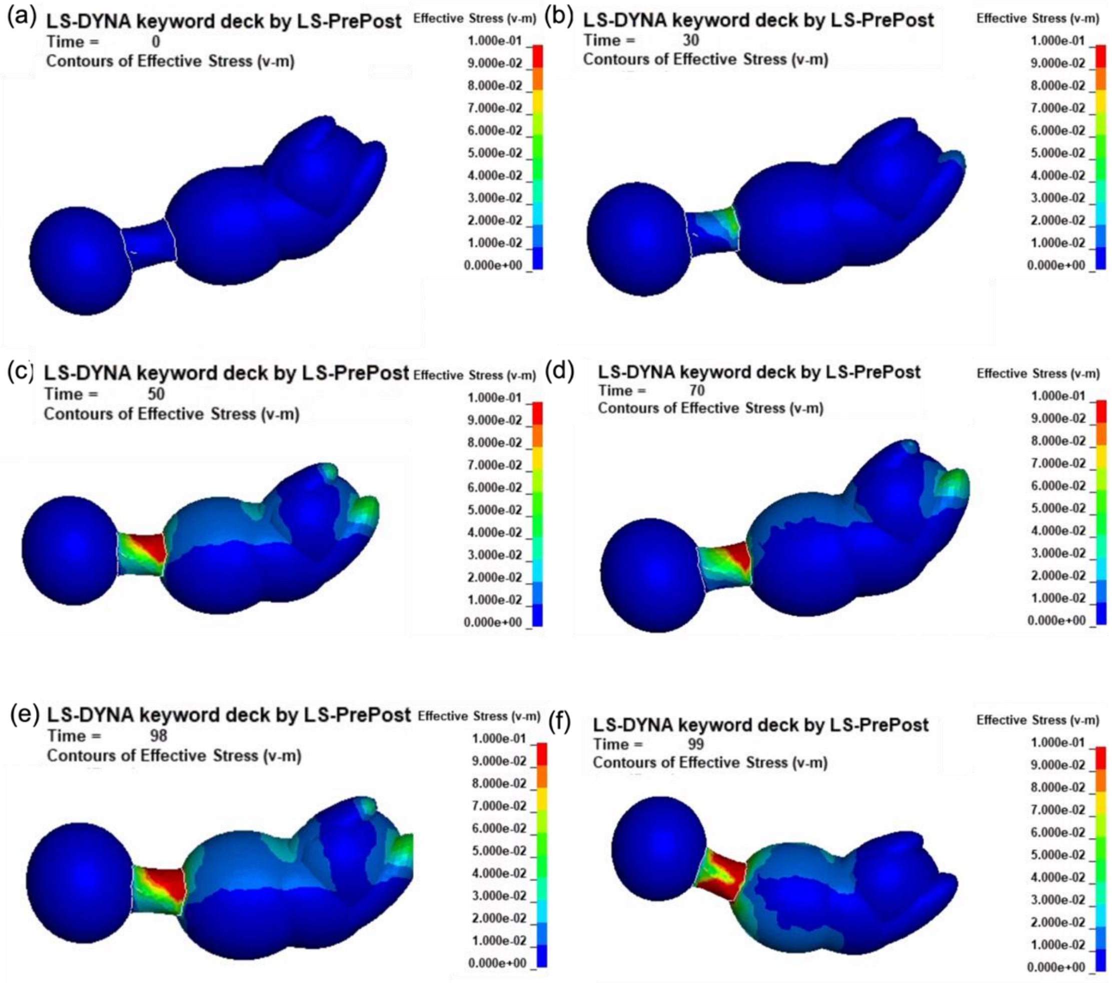

Figure 4.16, Stress nephogram of the fetus during the delivery process from 0 (a) to 99 (f) seconds.

The strain experienced by the fetus during the delivery process is shown in Figure 4.17. The distribution of the strain for the fetus was different from the distribution of the stress. The highest strain was 8.6%, 13.4%, 12.0%, 14.3%, and 19.3% at time points of 30 s, 50 s, 70 s, 98 s, and 99 s, respectively. The stress in the fetal neck was larger than the stress in the fetal body, while the strain in the fetal body was larger than the strain in the fetal neck. This is because the material properties of the neck and the body are different. The fetal body was modeled with nonlinear Neo Hookean hyperelastic material (C1=0.07 MPa), while the neck was modeled as a linear elastic material (E = 50 MPa). The stiffness of the neck, however, was higher than that of the body. As a result, even though the fetal body experienced smaller stress, the strain in the body was still larger than the strain in the neck.

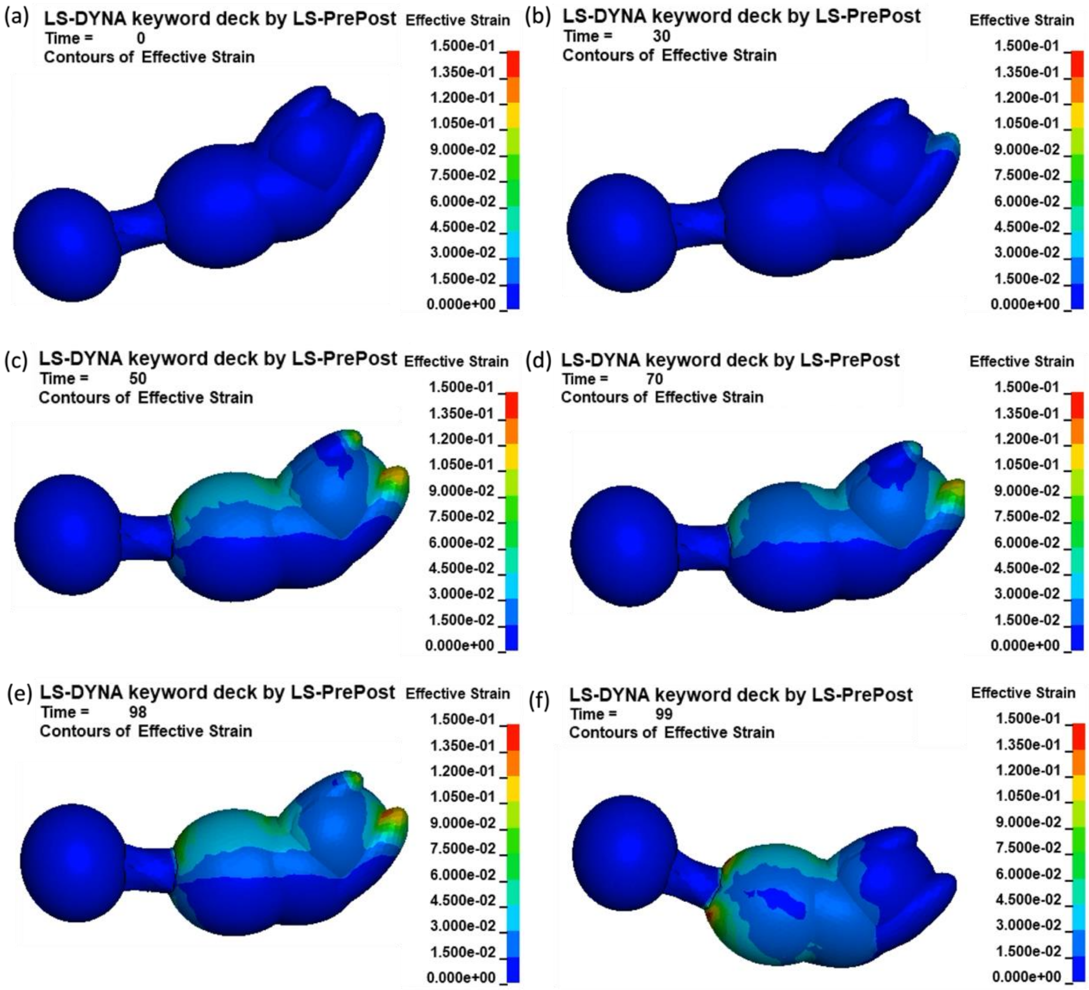

Figure 4.17, Strain nephogram of the fetus during the delivery process from 0 (a) to 99 (f) seconds.

The model was validated through comparisons with both experimental and simulation results in the literature. Specifically, the result that the fundus region of the uterus had the largest stress in the model matched experimental results that show that the fundus has a higher contraction intensity than the middle and lower parts of the uterus [23]. The values and location of maximum Von Mises and principal stress on the pelvic floor muscles also agreed well with other researchers' simulation results [52]. In addition, the duration of the labor, the displacement of the fetus during the delivery, and the rotation of the fetus were all within clinically observed ranges. The details of validation comparisons are summarized in Table 4.2 and are discussed in more detail in paragraphs of the Results section.

Table 4.2, Summaries of the validations.

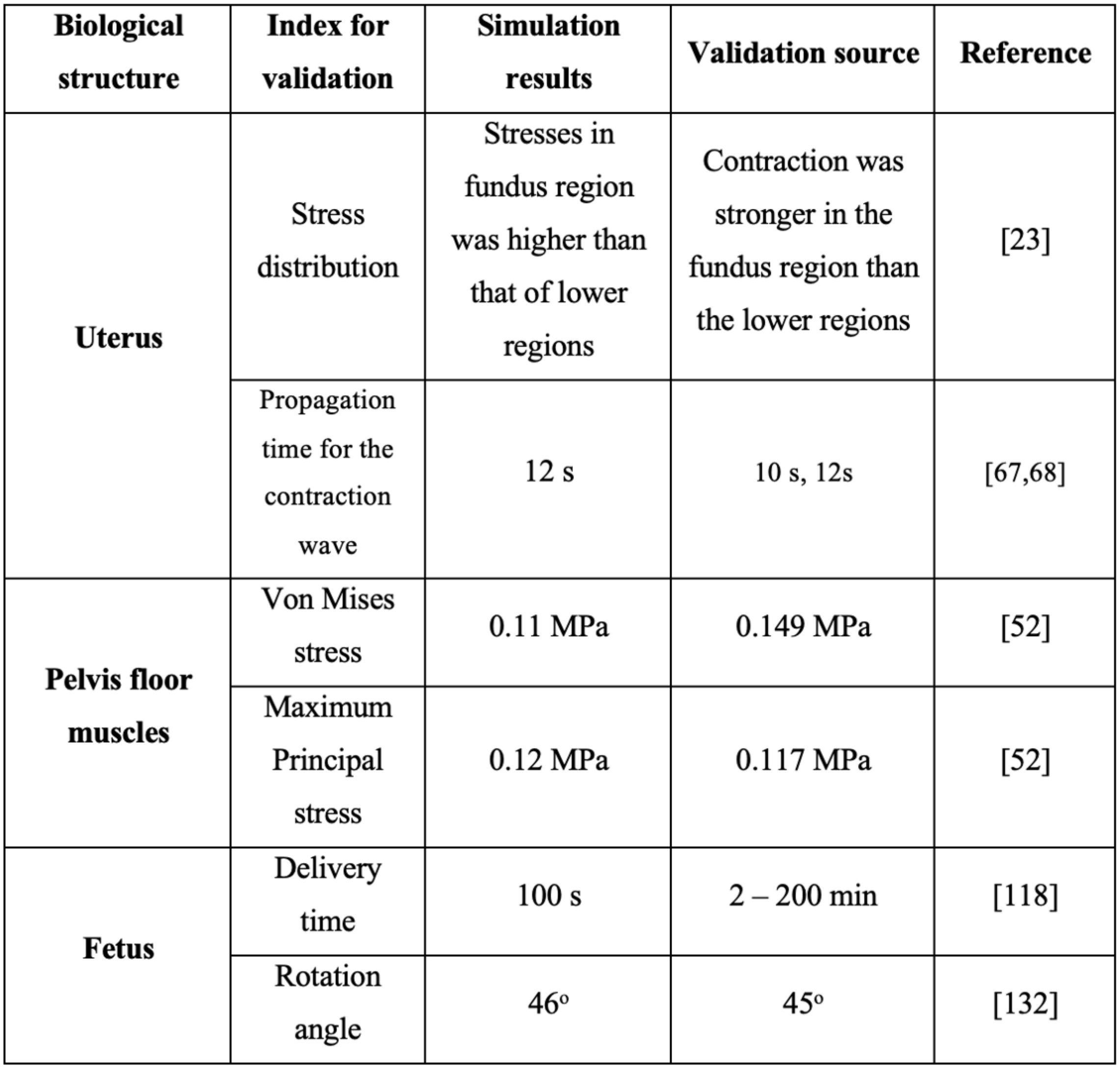

Biological structure	Index for validation	Simulation results	Validation source	Reference
Uterus	Stress distribution	Stresses in fundus region was higher than that of lower regions	Contraction was stronger in the fundus region than the lower regions	[23]
	Propagation time for the contraction wave	12 s	10 s, 12s	[67,68]
Pelvis floor muscles	Von Mises stress	0.11 MPa	0.149 MPa	[52]
	Maximum Principal stress	0.12 MPa	0.117 MPa	[52]
Fetus	Delivery time	100 s	2 – 200 min	[118]
	Rotation angle	46°	45°	[132]

4.4.2 Parametric Analysis

The results of the parametric analysis of the effects of fetal head size on stresses in the uterus, fetal neck and pelvic floor muscles are shown in Figure 4.18 and Table 4.3. Two diameters of the fetal head, 80 mm and 90 mm were chosen based on the normal size of a fetal head during labor, and this choice was supported by its alignment with other studies presented in the literature [52]. The Von Mises stress and maximum principal stress in the fetal neck increased significantly (48.2 % and 41.4 %) with the increase in the fetal head size from 80 mm to 90 mm. Both stresses in the pelvic floor muscles also increased slightly (Von Mises: +11.4 %; maximum principal: +27.3 %) with the increase in the head size. Conversely, the size of the fetal head had almost no impact on the stresses of the uterus. As the stress in the uterus is primarily created by the active contraction of the tissue, and not because of a reaction to the interaction of the uterus with the fetus, this last result meets expectations.

In Xuan's work, the increase in both the Von Mises stress and maximum principal stress within the pelvic floor muscles increased by a much greater degree (Von Mises: +33.3%; maximum principal: +58.3%) as the fetal head diameter increased from 80 to 90 mm [52], which is different from our work. One explanation for this difference is that, in Xuan's model, there was only a fetal head modeled as a rigid sphere. In contrast, a deformable fetal neck and body were modeled in the current work. The deformation and bending of the fetal neck and body during labor in the current model dissipated some of the energy needed to push and deliver the larger fetal head – thus reducing the energy transmitted to the pelvic floor muscles and reducing their stress. This is demonstrated through the significant increase seen in the stresses in the fetal neck, as shown in Figure 4.18, with the larger fetal head.

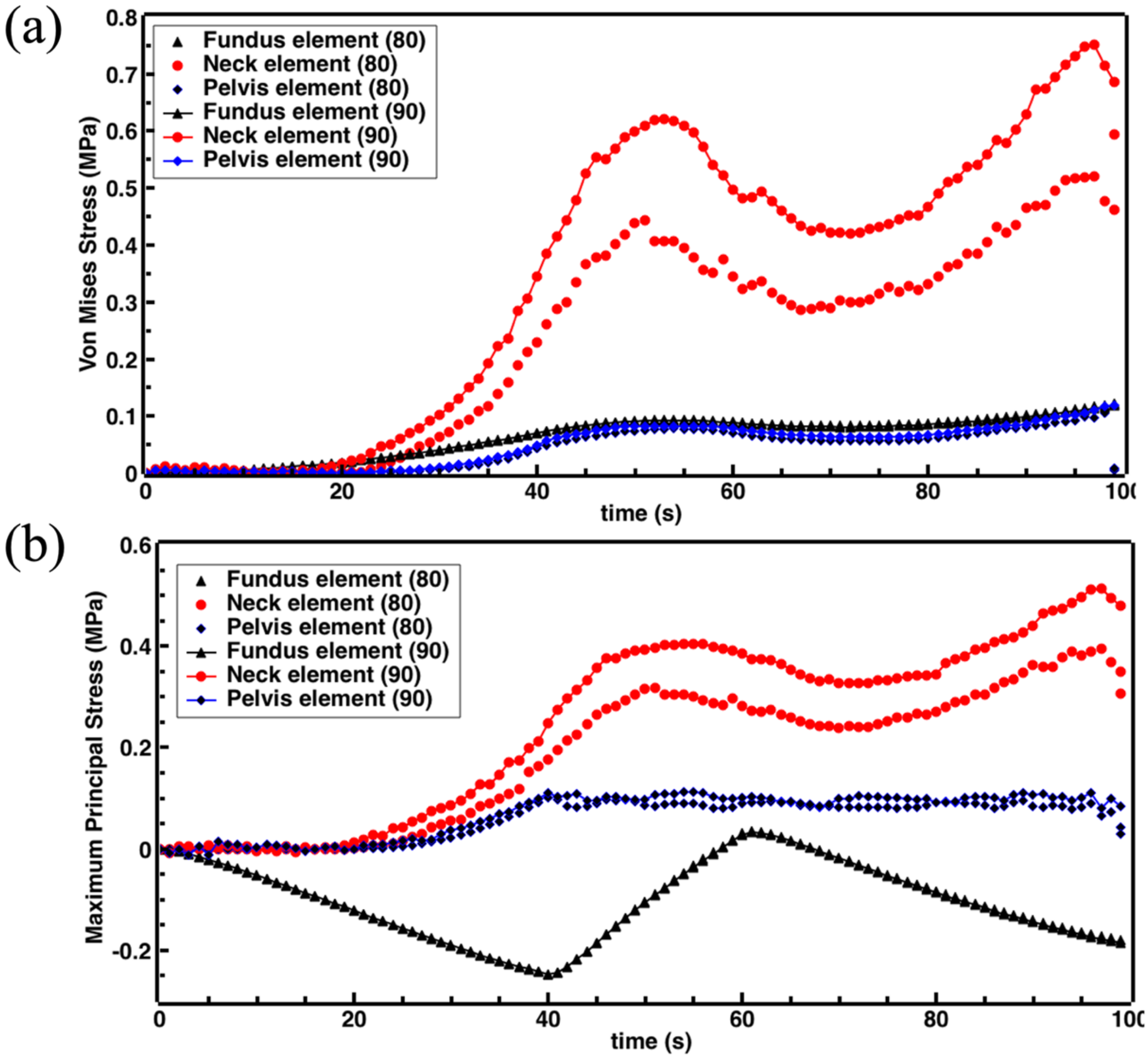

Figure 4.18, Effects of size of fetal head on Von Mises stress (a) and maximum principal stress (b) of the uterus, fetal neck, and pelvic floor muscles. Stress values were assessed in a single indicator element within each of the three anatomical structures.

The size of the fetal head also plays an important role in regulating the delivery time. Clinical research has already shown that a larger fetal head makes the delivery process more difficult and can cause prolonged labor [36,133]. This can be predicted and analyzed by the simulation model system. The fetal head with an 80 mm diameter was completely delivered at 99 s, while the fetal head with a 90 mm diameter was just partially delivered at this time, which means that a longer delivery time occurred. With the larger fetal head, the resistance force experienced by the fetus will be increased. Evidence for this is shown in the increased stresses that occur in the pelvic floor muscles for the larger fetal head. Therefore, it is more difficult for the fetus with the larger head to move through the birth canal. As a result, more uterine contraction cycles are required, so that the delivery time will be increased.

Table 4.3, Maximum stresses seen in indicator element for uterus, fetal neck, and pelvic floor muscles – comparing 80 mm and 90 mm fetal head sizes.

	80 mm Head				**90 mm Head**			
	Max Von Mises Stress [MPa]	**Time Point [s]**	**Max Principal Stress [MPa]**	**Time Point [s]**	**Max Von Mises Stress [MPa]**	**Time Point [s]**	**Max Principal Stress [MPa]**	**Time Point [s]**
Uterus	0.12	99	-0.24	40	0.12	99	-0.25	40
Pelvic Floor	0.11	98	0.09	96	0.12	99	0.11	96
Fetal Neck	0.6	99	0.4	97	0.75	97	0.51	97

4.5 Discussion

As always, there are limitations with the model described here – which do present opportunities for future research. First, the structures of the uterus, the bony pelvis, and the pelvic floor muscles are coupled tightly through connective tissues in a woman's body. However, in this model system, these structures were put in their relative positions by applying boundary conditions for each of them. This may affect the stress developed within the tissues – in particular the pelvic floor muscles, which deform significantly and will react to deformation in adjacent tissues. The incorporation of such connective tissues and surrounding organs, such as the vagina, the rectum, and the bladder, will negatively impact computational time due to the increase of the computation amount. The model as described in this paper already required 14 days for each run. If these structures are included, however, the forces resisting the movement of the fetus and the stresses experienced by the fetus will increase, and the stress value and distribution among the pelvis floor muscles will also be adjusted and more accurate. Most models investigating the mechanical behaviors of pelvis floor muscles have not considered such connective tissues, while they have also lacked the uterus and uterine active contraction [39,52,128]. In the previous studies, the movement of the fetus was imposed as a specific trajectory. The model in this study was able to push the fetus through the birth canal due to the uterine active contraction. Also, in the majority of previous models, only the fetal head was included, typically as a sphere or based on real skull geometry from MRI images [52,134,135], and only one contact between the fetal head and the pelvic floor muscles was defined. The model in this study introduced a whole fetus, including the head, neck, and body. The added biological structures of the uterus and fetal body, as well as defining and calculating responses for more contacts in this study, increased the number of needed computations and required longer computation time.

For the contractile fibers, the current model represented the main characteristics of fiber distribution within the uterus, as identified through experiments. For example, the fiber distribution for human uterine tissue showed strong anisotropy between different regions – with higher fiber content in the fundus region [23], longitudinal and circumferential directions as the two main fiber directions [94], and fibers that are inclined with respect to the uterine wall, which means they represent the three-dimensional fiber arrangement [19]. Although this model will allow for easy adjustment of the distribution of fibers within the different regions as the three fiber directions were modeled separately, the distribution of the fibers in this version of the model was still the same in the middle and lower parts of the uterus. More experimental data based on high-resolution images of the variation in orientation and statistics regarding fiber content will be needed to model the fibers more accurately in these regions.

The uterine active contraction in this model was described using the phenomenological Hill model, which has been used to model other smooth muscle tissues or organs in literature [74,136,137]. The Hill model has been shown to successfully match the macro-scale mechanical behavior of muscles found through phenomenological experiments. However, there are no underlying biological or chemical mechanisms at the cellular or subcellular level included in the phenomenological Hill model to describe the activation of muscle contraction. Therefore, it cannot be used to investigate the effects of cellular-level biochemical behaviors on the tissue and organ-level behaviors. A few efforts have been made to include the cross-bridge sliding [138,139] or calcium dynamics [64,66] within the Hill model in order to generate the active force and then incorporate that active component with a three-dimensional passive component of the muscle within the framework of continuum mechanics theory to develop a multi-scale model. This has not been attempted in the current project, but could be integrated in the future.

Finally, the intrauterine pressure is the hydrostatic pressure caused within the fluid inside of the uterus. It is unclear how important the intrauterine pressure is for the delivery process. Many women who experience spontaneous rupture of their membranes have a labor that progresses without delay or complication; however, there is some volume of fluid that remains within the uterus. Evidence for this comes both from the ability to measure intrauterine pressure with a catheter during labor after the membranes have ruptured and the gush of fluid that often accompanies the delivery of the infant's body. None of the current models of labor and delivery, whether computational or physical models, include this feature. This question can be explored in the future by including hydrostatic pressure within the model system.

4.6 Conclusion

In conclusion, an FEM model system was developed in LS-DYNA to simulate the uterine cyclic active contraction and delivery of a deformable fetus through the bony pelvis and pelvic floor muscles. In this model, the uterus was able to perform the large deformation, cyclic active contraction and propagation of the contraction wave needed to achieve delivery. During the childbirth process, the greatest stresses for the pelvic floor muscles happened in the contact area with the fetus head. For the fetus, the delivery displacement increased significantly and then decreased slightly with the rise and the decline of the activation level in different contractions, respectively. The fetal neck had much higher stress compared to the stress in the fetus' body. The larger fetal head was found to increase the stresses in the fetal neck significantly, while it had smaller effect on stresses in the pelvic floor muscles and a minimal effect on the uterus. This model matches the phenomenological activity of the uterus and the response of the fetus to that activity. This is the first model that has relied on force derived directly from uterine contractions to deliver a full fetal body through the maternal pelvis. The model system will be used in the future for analysis of tissue response linked to pelvic floor disorders and brachial plexus injury.

CHAPTER 5: Conclusions and Future Work

5.1 Conclusions

This current project resulted in numerous advances related to the computational modeling of smooth muscle contraction, uterine active contraction, and the integration of a model system including pelvic structures for performing a simulated delivery of a term fetus during the second stage of labor.

In Chapter Two, first, the one-dimensional contractile fibers using the Hill muscle material model and a three-dimensional passive portion of muscle tissue using elastic and hyperelastic material models were coupled successfully in LS-DYNA so that a computational model for a generalized muscle tissue was developed and its active contraction behaviors were investigated. The active contractile fibers caused the muscle tissue to contract in a case where no external loading force was applied on the muscle tissue, while the passive portion resisted such contraction process but supported the relaxation behaviors. These behaviors verified that the method of bonding between the contractile fibers and passive muscle portion can be implemented to model a muscle tissue's active contraction and relaxation behaviors. Through the parameter analysis, the PIS and DMP parameters in the Hill model were found to control the contraction capacity, and contraction and relaxation speed of a muscle tissue, respectively. The contraction behaviors of specific smooth muscle tissue were simulated and compared with experimental results. The simulation results closely matched the experimental results, which demonstrated that the phenomenological three-element Hill constitutive model in LS-DYNA is an appropriate option for modeling of active contraction behaviors of involuntary muscles. This model can now be assembled into a uterus to simulate uterine phenomenological active contraction so that their macro-scale biomechanical behaviors can be more accurately investigated in a way that saves the computation amount and time significantly.

In Chapter Three, first, the three-dimensional fibers, in longitudinal, circumferential, and normal directions, were created and bonded with the uterine passive muscle wall successfully so that a computational model of a uterus was developed in LS-DYNA. The effects of how each direction of fibers and the combination of different directions of fibers on the contraction pattern of the uterus were investigated. It was found that the longitudinal direction fibers caused the uterus to shorten in the longitudinal direction but extend in the circumferential direction; the circumferential direction fibers caused the uterus to be constrained in the circumferential direction but extend in the longitudinal direction; the normal direction fibers did not contribute to the deformation of the uterus much but affected the stress and strain distribution of the uterus. It was demonstrated that the fiber distribution inside the uterine wall can significantly affect the uterus contraction pattern. Second, the uterus model considered and represented several important mechanical properties of a pregnant uterus during labor, such as the anisotropy and heterogeneity of the fiber distribution, large deformation, cyclic active contraction, and propagation of the contraction wave needed to achieve fetal delivery. Similar to the muscle tissue, the contraction capacity and contraction speed were also determined by the PIS and DMP parameters in the Hill model. Finally, a computational model composed of a uterus and a rigid fetus was developed and the delivery of such a fetus caused by the contraction of the uterus was simulated. This is a significant advance compared to models in literature where the pregnant uterus either couldn’t contract actively, had very small deformation, required too long of a computational time, included two-dimensional and evenly distributed fibers, or did not include a fetus model. Such a uterus model was validated on the aspects of the stress distribution of the uterus, contraction wave propagation time period, and delivery time for the fetus. The developed computational model of the uterus provides the foundation for the integration of a complete model system including the pelvic structures.

In Chapter Four, a complete FEM model system composed of the uterus, the fetus, and the pelvic structures (bony pelvis and pelvis floor muscles) was established in LS-DYNA. Unlike the models simulating the movement of the fetus through the pelvic structures in literature where only the rigid fetal head or body was modeled, the fetus in this model was composed of three components: head, neck, and body. In addition, the fetal neck and body were deformable, and their stress and strain were calculated. It was found that the stress in the neck was much higher than that in the fetal body, which indicated that the neck of the fetus is at higher risk of injury during the childbirth process. The fetal delivery displacement increased significantly and then decreased slightly with the rise and the decline of the activation level in different contraction cycles, respectively, during labor. The movement of the fetus in this model was caused by the uterine contraction, as it is in reality, not by the force applied on the fetal body or prescribed motion curve as used in most models in the literature. For the pelvic structures, during the childbirth process, the greatest stresses for the pelvic floor muscles occurred in the contact area with the fetal head. The model system was validated based on available data and clinically observed phenomena, such as stress distribution within the uterus, time period for uterine contraction wave propagation, values of Von Mises stress and Principal stress of the pelvic floor muscles, and rotation, movement, and delivery time of the fetus. Through the parametric analysis, the larger fetal head was found to increase the stresses in the fetal neck significantly, while it had a smaller effect on stresses in the pelvic floor muscles and a minimal effect on the uterus. This model matches the phenomenological activity of the uterus and the response of the fetus to that activity. This is the first model that has relied on force derived directly from uterine active contractions to deliver a full fetal body through the maternal pelvis. The model system will be used for analyzing pelvic floor disorders and brachial plexus injuries in the future.

5.2 Future Work

Although huge advances in computational modeling of uterus active contraction and fetus delivery during the second stage labor has been made in the current project, there are always next steps to pursue to improve the computational model further. A few areas for future work have been listed and discussed.

5.2.1 Mechanisms of Uterine Active Contraction

To describe the smooth muscle tissue's active contraction behaviors, the first option is to use the phenomenological Hill model directly [74,136,137]. For example, Bates *et al.* [74] developed a two-dimensional computational model of an airway that was embedded into a uniform elastic lung parenchyma. The model was used to investigate how the force-velocity relation of the airway smooth muscle operated against the opposing forces caused by the parenchymal tethering and airway wall and their role in affecting the dynamics of bronchoconstriction. Their results showed that the dynamics of bronchoconstriction can be explained by using the classic Hill force-velocity relation for the airway and its interaction with the surrounding lung parenchyma and the airway wall. Recently, Piero *et al.* [136] developed a three-dimensional Finite Element Model to investigate the biomechanics of the abdominal wall, where the active contraction behaviors of the abdominal wall, which were not considered in previous studies, were described by the Hill model. The muscular active contraction was found to reduce the membrane force on fascial structures, which demonstrated that the membrane force was overestimated in the pure passive simulation models. The results suggested that it was necessary to include such muscular active contraction into the abdominal wall to describe the abdominal wall's mechanical behaviors more accurately.

In order to advance the model of uterine contraction so that cellular-level physiology and pathophysiology can be included, a multiscale model will be needed. There are two ways to incorporate the cellular-level biochemical mechanisms for active stress generation into the Hill model. The first way is to develop a theoretical model to explain the production of the active stress specifically for the uterine smooth muscle cell, which can be used as the active part in the Hill model. This modified Hill model could then be maintained as the one-dimensional model. The Hai-Murphy model could be considered for this role, but it should be modified as the specific mechanisms or variables are different for uterine smooth muscle cells. The new Hill model would need to be implemented into FEM software, such as LS-DYNA. The complete mechanical behavior of the uterus can still be modeled by coupling such a modified 1D Hill model representing the fibers and the 3D passive portion of a muscle tissue in FEM by sharing the nodes between the 1D truss beam elements and the 3D solid elements. A second way to create a multiscale model is to develop a 3D constitutive model that includes theories for the production of the active stress coupling of the actin-myosin system and for a constitutive law for the passive portion of a muscle organ under the framework of continuum mechanics. This new 3D constitutive model would also need to be implemented into an FEM software package. The first method could more conveniently consider the strong anisotropy of the fiber orientation and content inside of the uterine wall in different regions of the uterus. The second method would save the effort associated with generating the 1D beam elements and the coupling process with the 3D passive portion of the uterus. But the derivation of the 3D constitutive law and implementation of such a model into the FEM software could be more difficult, as well as being more inconvenient to consider the anisotropy of the fiber distribution.

5.2.2 Effects of the Intrauterine Pressure

The model system that we have established successfully performed the uterine active contraction which pushed the fetus to move through the uterus and pelvic structures, which is unlike most investigations in the literature where the movement of the fetus relied on either a force applied to the center of the fetus or constrained motion (without any consideration of the force). Aside from the uterine active contraction, the intrauterine pressure inside of the uterus also plays a role in regulating the movement of the fetus through the birth canal. Intrauterine pressure is the hydrostatic pressure within the amniotic fluid caused by the contraction of the uterus, which is usually measured by an intrauterine pressure catheter (IUPC) [140]. Measurement of the intrauterine pressure was initially intended to monitor the contraction activities of the uterus. The normal range of intrauterine pressure in the first and second stages of labor was summarized in Grimm's review [40]. Briefly, in the first stage, the intrauterine pressure is caused only by the contraction of the uterus, and the peak intrauterine pressure can vary between 10 to 50 mmHg or as high as 70 mmHg. In the second stage, the intrauterine peak pressure varies from 50 mmHg to 150 mmHg, while the basal pressure is about 10 to 20 mmHg. Transmission of force to the fetus likely occurs both due to contact of the contracting muscle with the fetal body and the increase in intrauterine pressure.

It also has been found that the intrauterine pressure is closely related to other forces acting during the fetus's movement through the birth canal and influences the labor process. For example, Mandel *et al.* [141] measured the intrauterine pressure in 22 women during labor. In the first group, patients pushed with their legs in stirrups. In the second group, patients pushed with their legs hyperflexed by 135^o (McRoberts' position). The results showed that the intrauterine pressure was doubled in the McRoberts' position and the pushing efficiency was increased by 32%. It was suggested by the study that the increase in intrauterine pressure contributed to an increase in the pushing force on the fetus. In addition, the relationship between the intrauterine pressure and the head-to-cervix force was reported by Allman *et al.* [142]. They measured the intrauterine pressure and the head-to-cervix force simultaneously by IUPC and a specifically designed force sensor, respectively. Based on the plotted scattergrams of the force and the pressure, these two variables showed a strong linear relationship. Rempen *et al.* [143] designed an instrument to measure the pressure acting on the fetal head and the intrauterine pressure in labor. They found that the pressure on the fetal head was linearly related to the intrauterine pressure. Also, the pressure on the fetus's head was about twice that of the intrauterine pressure. Overall, the intrauterine pressure is an important factor in regulating the labor process, as demonstrated in the literature, and therefore deserves more attention in a simulation model. However, the intrauterine pressure has not been simulated in any models of childbirth process to date. Simulating IUP would be the next step in developing a realistic simulation.

To include the intrauterine pressure in the developed model system, one way would be to apply the hydrostatic pressure to the inner wall of the uterus and the fetus's body using the relation of intrauterine pressure and time obtained from experiments. Another way would be to model the amniotic fluid inside of the uterus and conduct a simulation of the Fluid-Structure Interaction (FSI). The difference between these two ways is that the first way is much simpler, while the second way can not only provide the hydrostatic pressure on both the inner wall of the uterus and the fetus's body but also the boundary condition or restriction of movements on the fetal body. Therefore, the second way will provide a more realistic model of the intrauterine pressure, but at a much more expensive computational cost.

The common way to conduct the FSI simulation in LS-DYNA is to use the Arbitrary Lagrangian Eulerian (ALE) technique [144,145]. Such a technique has been applied to simulate many FSI problems in literature. Truong *et al.* [146] used different commercial software packages (LS-DYNA ALE, ANSYS CFX, and Star-CCM+/ABAQUS) for FSI simulation to investigate the effects of slamming on the ship or the offshore structure's flat-stiffened plates. The total vertical forces acting on the plates and the corresponding structural responses were analyzed in the study. The simulation results showed that the equivalent pressure decreased with the increase in impact velocity and increased if the impact structures were stiffer. Song *et al.* [147] used the ALE FEI method in LS-DYNA to calculate the contact force and the ship motions during a ship-ship collision. The contact force and energy dissipation were significantly affected by the ship's forward velocity. The ship with heavier mass was found to have a deeper penetration and a greater energy dissipation. Finally, the collision angle greatly contributed to the damage of the ship. with the worst case corresponding to a 120^{o} angle of impact. Hua *et al.* developed a simulation model using ALE in LS-DYNA to simulate the [144] fluid-solid interaction on water ditching of an airplane. The high pressure occurred first in the rear and then at the front of the airplane with the highest value of 20 MPa. Also, the front parts of the passenger cabins had higher acceleration than the rear parts. During labor, the amniotic fluid also strongly interacts with the uterine inner wall and the fetus. The ALE in LS-DYNA is believed to be a good way to investigate the effects of intrauterine pressure on the childbirth process accurately.

5.2.3 Neonatal Brachial Plexus Injury

Neonatal brachial plexus palsy occurs in about 1 to 4 per 1000 births [148] , often during complicated childbirth scenarios. Shoulder dystocia is the failure of the delivery of the fetus's shoulder and body after the fetal head's delivery. The over-stretch of the brachial plexus due to the damaging forces caused by both the endogenous (maternal) forces and the exogenous (clinical applied) forces is believed to be the main reason for the brachial plexus injury [149]. However, the studies investigating the mechanisms of brachial plexus palsy are still limited. Given the ethical reasons and the difficulties of measuring forces, tissue stress, and strain during the actual childbirth process, computational modeling serves as a great tool to overcome such limitations and quantitively investigate the effect of forces involved in the fetus delivery process.

A few studies that develop simulation models to investigate brachial plexus injury have been conducted. In 2003, Gonik *et al.* [150] developed a simulation model in MADYMO software including the fetus anatomy, maternal pelvis, and the brachial plexus to investigate the effects of both the endogenous and exogenous forces on the brachial plexus stretch during a shoulder dystocia scenario. The brachial plexus nerve was modeled as a spring and the change of its length was recorded during the simulation as the stretch of the nerve. In the results, the endogenous and exogenous forces were associated with a brachial plexus stretch of 15.7% and 14.0% in the case of lithotomy positioning, and 6.6% in the case of McRoberts positioning. It was also suggested that applied forces, fetal head position, and pelvic orientation can all affect the brachial plexus stretch. Based on this work, in 2010, Grimm *et al.* [151] investigated how clinician-applied maneuvers affect the delivery force and brachial plexus stretch in a shoulder dystocia event. It was found that all the maneuvers significantly reduced both the force required for the fetus delivery and the brachial plexus stretch compared to the lithotomy position. The posterior arm delivery had the greatest effect with a reduction of 71% of the brachial plexus stretch and a reduction of 80% of the delivery force.

However, there are a few limitations to these models. For example, the brachial plexus was modeled as a spring connecting the neck and the shoulder. A more realistic nerve model considering accurate anatomy of the structure should be modeled. Also, the spring in the model can only represent the nerve’s elastic mechanical characteristic, while the nerves have non-linear mechanical behaviors -- especially when the deformation is large. In addition, to simulate the damage or even the rupture occurring to the brachial plexus due to the over-stretch, the usual linear elastic or non-linear constitutive model, such as the Neo-Hookean or Mooney-Rivlin model, is insufficient and constitutive models for fracture propagation or rupture may provide more insight into the process. Also, these computational models have not modeled the full second stage of labor and the effect of uterine active contractions pushing on the fetus to make it move. Instead, the movement of the fetus in the model was caused by the loading force applied to the fetus. The model considered the maternal pelvis, but the pelvic floor muscles were not modeled, therefore the strong interaction between the fetus and the pelvis structures was not considered in this earlier work.

Future work will incorporate more of the anatomical tissues and structures for the fetal neck -- such as the nerves, vertebrae, intervertebral discs, muscle, and connective tissue – to assess the response of the fetal cervical structures more precisely to the forces experienced during labor and delivery. In addition, a more realistic geometry of the fetal head will be used to replace the spherical fetal head in the model.

5.2.4 Delivery of the Whole Fetus

Shoulder dystocia is an obstetric complication that occurs when the delivery of a fetal body is prevented as the fetus's anterior shoulder impacts with the mother's pubic bone after the vaginal delivery of the fetal head [152]. None of the simulation models that have previously been developed and published describing the uterine active contraction or the fetus delivery through the pelvis and vagina have simulated the complete delivery of a whole fetus from the uterus to the outside of a mother's body.

The current model system has successfully delivered the fetal head from the mother's body, while the deformable fetal neck and body have not delivered yet through the pelvic structures. The simulation model terminated due to an error caused by the rapid transition of the fetal head past the pelvic floor muscles. This jumping of the fetal head was believed to be caused mainly by the sudden release of the deformation energy stored in the pelvic floor muscles. The fetal head was modeled as a rigid body in the current simulation, which cannot deform and dissipate any of the energy used to push the fetus through the birth canal, also contributed to the jumping phenomenon. In reality, the fetal head -- including the overlapping bones of the skull -- also undergoes large deformations during the delivery through the birth canal. To weaken the jumping phenomenon in the simulation model so that the over-speed issue could be avoided in LS-DYNA and make the model continue to run after the delivery of the fetal head, the fetal head needs to be modeled as a deformable material, such as an elastic or hyperplastic material.

In addition, the structures of the uterus, bony pelvis, pelvic floor muscles, and vagina need to be modeled in a smoothly connected way, -- and it is vital to model the birth canal as a complete and smooth structure. To further improve biofidelity, the abdominal wall needs to be included in the model system, as the maternal pushing force acting on the abdominal wall was found to increase the intrauterine pressure and result in a higher delivery efficiency [141]. Finally, the supporting structures surrounding the birth canal may also play a role in regulating the fetal movement, such as adjusting the boundary condition of the fetus's movement and dissipating the energy associated with the delivery, which should ideally be considered and modeled as well.

The clinician-applied forces, which are usually applied through the clinician's hands, a vacuum extractor, or forceps [40], can be important for the overall delivery process of the fetus. The mean maximum traction force using instrumented forceps was measured as 154 N to 188 N [153]. The maximum traction force provided by a vacuum extractor varies with the size of the vacuum cup and ranges from 118 N to 308 N [40]. For the traction forces applied by hands, the average force was 17 N to 47 N for normal deliveries measured in Allen's study [154]. In the case of shoulder dystocia, such forces applied by the clinician in different ways were usually larger than that of the normal delivery. In order to simulate the full range of delivery processes through to the delivery of a whole infant body, the ability to apply such forces to the fetal head in the model would be an important component of matching the clinical scenarios.

5.2.5 Experiments to Enhance Model Development and Validation

The model system in this project was mostly developed based on the clinical and experimental data. However, such data on anatomy and physiology related to term pregnancy are still very limited. To enhance the model development of simulating the childbirth process during the second stage labor, there are a few aspects related to experimental efforts that could be helpful to fill some of the gaps. For example, the three-dimensional fibers built inside of the uterine wall in the model represented several important characteristics of fiber distribution based on experimental findings [19,23,94]. Specifically, fiber content was set higher in the fundus region; fibers were created in three dimensions; longitudinal direction fibers were the predominant ones; strong anisotropy of fiber distribution in different regions was considered. However, the distribution of the fibers kept constant in the middle and lower parts of the uterus in this version of the model, and the variation of the fiber distribution through different layers in uterine muscle wall thickness direction was not considered, due to the lack of experimental data. More experiments on high-resolution images of the variation in orientation and statistics regarding fiber content will be needed so that the fiber distribution can be more accurately modeled in different regions and layers on the uterus.

The commonly accepted explanation about the direction of the propagation wave for the pregnant uterus during labor has been that the propagation of both electrical and mechanical activities should start from the top region of the uterus and propagate in the downward direction to the rest of the uterus [23,155]. However, this conclusion has more recently become controversial with new findings from experiments. For example, Mikkelsen *et al* recorded the electrohysterography signals for the uterus during the labor contraction to determine the propagation velocity and direction [156]. They found that both downward and upward propagation of electrohysterography signals were recorded, and the downward and upward propagation occurred at the same time in the upper and lower part of the uterus, respectively, which suggested that the propagation of electrical and mechanical signals of the uterus during labor was multidirectional. Other researchers even believed that each cell of the uterus can be the pacemaker and the propagation of contraction or electrical signals for the uterus during labor could be chaotic [157].

The current set of published computational models simulating the propagation of the electrical activity in the uterus during the second stage of labor also have only simulated the downward direction of this triggering signal. For example, Cochran *et al* [67] developed a mathematical model including tissue mechanics and electrical activity to simulate the contraction of the pregnant uterus. The tissue mechanics were described with continuum mechanics and the electrical activity was described with the FitzHugh-Nagumo model. The geometry of the uterine wall was modeled as a half ellipsoid. The simulation results showed the propagation of the electrical signal initiated from a pacemaker in the fundus region and propagated to the lower part of the uterus. It took 10 seconds for such electrical activity to propagate to the whole uterus, which was close to the time (12 seconds) needed in our simulation model. Another similar computational model was developed by Yochum *et al* [68] in 2016, where the contraction of a pregnant uterus was described by a multiscale electro-mechanical model. The mechanical and electrical behaviors were simulated on a single cell level first, then on a two-dimensional tissue level, and a real three-dimensional uterus in the last step. In Yochum's model, the electrical activity was also initiated from the fundus region of the uterus and propagated to the lower part. Also, the propagation time for both the electrical and mechanical activities from the fundus to the whole uterus was about 12 seconds, which was almost the same as the current work and very close to Cochran's work.

The relaxation behavior of the uterus during labor has also recently generated some controversy. One perspective is that even though the uterine contraction started at different times due to the propagation of signals for the upper and lower part of the uterus, all regions of the uterus relax simultaneously at during each contraction cycle [23], which matched the uterine behaviors modeled in this study. Another perspective is now that there is a difference in relaxation pattern between women who successfully deliver vaginally and those who experience a delay in labor that results in a cesarean section. For women who deliver vaginally, it is hypothesized that the lower segment of the uterus starts to relax earlier than the upper portion. This contrasts with the phenomena observed in women who undergo cesarean delivery, where the upper portion of the uterus starts to relax earlier than the lower segments. This latter system matched with Cochran and Yochum's simulations [158]. To take this potential multidirectional propagation of the contraction and the relaxation behaviors in the pregnant uterus during labor into account, more experiments need to be conducted to provide more details about both physiological and pathophysiological variations.

BIBLIOGRAPHY

[1] Cunningham, F. G., Leveno, K. J., Bloom, S. L., Spong, C. Y., and Dashe, J. S., 2014, Williams Obstetrics, 24e, Mcgraw-hill New York, NY, USA.

[2] Kitzinger, S., 2003, The Complete Book of Pregnancy & Childbirth, Knopf.

[3] Satin, A. J., “Labor: Diagnosis and Management of the Latent Phase.”

[4] Baxter, J., 2007, “Care during the Latent Phase of Labour: Supporting Normal Birth,” Br J Midwifery, **15**(12), pp. 765–767.

[5] Cheng, Y. W., and Caughey, A. B., 2017, “Defining and Managing Normal and Abnormal Second Stage of Labor,” Obstet Gynecol Clin North Am, **44**(4), pp. 547–566.

[6] Huang, J., Zang, Y., Ren, L. H., Li, F. J., and Lu, H., 2019, “A Review and Comparison of Common Maternal Positions during the Second-Stage of Labor,” Int J Nurs Sci, **6**(4), pp. 460–467.

[7] Cohen, W. R., and Friedman, E. A., 2023, “The Second Stage of Labor,” Am J Obstet Gynecol.

[8] Myers, K. M., and Elad, D., 2017, “Biomechanics of the Human Uterus,” Wiley Interdiscip Rev Syst Biol Med, **9**(5), pp. 1–20.

[9] Evans, A. T., 2007, Manual of Obstetrics, Lippincott Williams & Wilkins.

[10] Cunningham, F. G., Leveno, K. J., Bloom, S. L., Dashe, J. S., Hoffman, B. L., Casey, B. M., and Spong, C. Y., 2021, Obstetrícia de Williams-25, McGraw Hill Brasil.

[11] Alrubaii, B. J., 2005, “Lack of Progress in Labour as a Reason for Cesarean,” Medical Journal of Babylon, **2**(1).

[12] Bakker, P. C. A. M., Van Rijsiwijk, S., and Van Geijn, H. P., 2007, “Uterine Activity Monitoring during Labor,” J Perinat Med, **35**(6), pp. 468–477.

[13] Zagami, S. E., Golmakani, N., Saadatjoo, S. A.-R., Ghomian, N., and Baghbani, B., 2015, “The Shape of Uterine Contractions and Labor Progress in the Spontaneous Active Labor,” Iran J Med Sci, **40**(2), p. 98.

[14] Ramsey, E. M., 1994, “Anatomy of the Human Uterus,” The uterus, pp. 18–40.

[15] Young, R., and Hession, R., 1999, “Three-Dimensional Structure of the Smooth Muscle in the Term-Pregnant Human Uterus,” Obstetrics & Gynecology, **93**(1), pp. 94–99.

[16] Weiss, S., Jaermann, T., Schmid, P., Staempfli, P., Boesiger, P., Niederer, P., Caduff, R., and Bajka, M., 2006, “Three-Dimensional Fiber Architecture of the Nonpregnant Human Uterus Determined Ex Vivo Using Magnetic Resonance Diffusion Tensor Imaging,” Anatomical Record - Part A Discoveries in Molecular, Cellular, and Evolutionary Biology, **288**(1), pp. 84–90.

[17] Fujimoto, K., Kido, A., Okada, T., Uchikoshi, M., and Togashi, K., 2013, “Diffusion Tensor Imaging (DTI) of the Normal Human Uterus in Vivo at 3 Tesla: Comparison of DTI Parameters in the Different Uterine Layers,” Journal of Magnetic Resonance Imaging, **38**(6), pp. 1494–1500.

[18] Goerttler, K., 1968, “Die Struktur Der Wand Des Menschlichen Uterus,” Arch Gynakol, **205**(4), pp. 334–342.

[19] McLean, J. P., Fang, S., Gallos, G., Myers, K. M., and Hendon, C. P., 2020, “Three-Dimensional Collagen Fiber Mapping and Tractography of Human Uterine Tissue Using OCT,” Biomed Opt Express, **11**(10), p. 5518.

[20] Wetzstein, R., and Renn, K. H., 1970, “Zur Anordnung Der Glatten Muskulatur Im Corpus Uteri Des Menschen,” Verh Anat Ges, **64**, pp. 461–468.

[21] Dubrauszky, V., Schwalm, H., and Fleischer, M., 1971, “Das Bindegewebsfasersystem Des Myometrium Während Der Geschlechtsreife, Der Menopause Und Der Gravidität,” Arch Gynakol, **210**(3), pp. 276–292.

[22] Vila Pouca, M. C. P., Ferreira, J. P. S., Oliveira, D. A., Parente, M. P. L., Mascarenhas, M. T., and Natal Jorge, R. M., 2019, Simulation of the Uterine Contractions and Foetus Expulsion Using a Chemo-Mechanical Constitutive Model.

[23] Caldeyro-Barcia, R., Alvarez, H., and Poseiro, J. J., 1955, “Normal and Abnormal Uterine Contractility in Labour,” Triangle, **2**(41).

[24] Webb, R. C., 2003, “Smooth Muscle Contraction and Relaxation,” Adv Physiol Educ, **27**(4), pp. 201–206.

[25] Biga, L. M., Dawson, S., Harwell, A., Hopkins, R., Kaufmann, J., LeMaster, M., Matern, P., Morrison-Graham, K., Quick, D., and Runyeon, J., 2020, “Anatomy & Physiology.”

[26] Widmaier, E. P., Raff, H., and Strang, K. T., 2010, “Muscle Vander’s Human Physiology: The Mechanisms of Body Function.”

[27] Bursztyn, L., Eytan, O., Jaffa, A. J., and Elad, D., 2007, “Mathematical Model of Excitation-Contraction in a Uterine Smooth Muscle Cell,” Am J Physiol Cell Physiol, **292**, pp. 1816–1829.

[28] Sanborn, B. M., 2001, “Hormones and Calcium: Mechanisms Controlling Uterine Smooth Muscle Contractile Activity,” Exp Physiol, **86**(2), pp. 223–237.

[29] Maggio, C. D., Jennings, S. R., Robichaux, J. L., Stapor, P. C., and Hyman, J. M., 2012, “A Modified Hai–Murphy Model of Uterine Smooth Muscle Contraction,” Bull Math Biol, **74**(1), pp. 143–158.

[30] Moore, K. L., and Dalley, A. F., 2018, Clinically Oriented Anatomy, Wolters kluwer india Pvt Ltd.

[31] VanPutte, C. L., Regan, J. L., Russo, A. F., Seeley, R. R., Stephens, T., and Tate, P., 2019, Seeley’s Anatomy & Physiology, University of Iowa.

[32] Paulo, M., Parente, L., and Teresa Da Quinta E Costa De Mascarenhas Saraiva, M., 2008, Biomechanics of the Pelvic Floor during Vaginal Delivery.

[33] Netter, F. H., 2014, Atlas of Human Anatomy, Professional Edition E-Book: Including NetterReference. Com Access with Full Downloadable Image Bank, Elsevier health sciences.

[34] Pavličev, M., Romero, R., and Mitteroecker, P., 2020, "Evolution of the Human Pelvis and Obstructed Labor: New Explanations of an Old Obstetrical Dilemma," Am J Obstet Gynecol, **222**(1), pp. 3–16.

[35] Hofmeyr, G. J., and Singata-Madliki, M., 2020, "The Second Stage of Labor," Best Pract Res Clin Obstet Gynaecol, **67**, pp. 53–64.

[36] Korhonen, U., Taipale, P., and Heinonen, S., 2014, "The Diagnostic Accuracy of Pelvic Measurements: Threshold Values and Fetal Size," Arch Gynecol Obstet, **290**(4), pp. 643–648.

[37] Kjeldsen, L. L., Blankholm, A. D., Jurik, A. G., Salvig, J. D., and Maimburg, R. D., 2021, "Pelvic Capacity in Pregnant Women, Identified Using Magnetic Resonance Imaging," Acta Obstet Gynecol Scand, **100**(8), pp. 1454–1462.

[38] Mihara, A., Kanchiku, T., Nishida, N., Tagawa, H., Ohgi, J., Suzuki, H., Imajo, Y., Funaba, M., Nakashima, D., and Chen, X., 2018, "Biomechanical Analysis of Brachial Plexus Injury: Availability of Three-Dimensional Finite Element Model of the Brachial Plexus," Exp Ther Med, **15**(2), pp. 1989–1993.

[39] Parente, M. P. L., Jorge, R. M. N., Mascarenhas, T., Fernandes, A. A., and Martins, J. A. C., 2008, "Deformation of the Pelvic Floor Muscles during a Vaginal Delivery," Int Urogynecol J, **19**, pp. 65–71.

[40] Grimm, M. J., 2021, "Forces Involved with Labor and Delivery—A Biomechanical Perspective," Ann Biomed Eng.

[41] Cunningham, F. G., Leveno, K. J., Bloom, S. L., Dashe, J. S., Hoffman, B. L., Casey, B. M., and Spong, C. Y., 2021, Obstetrícia de Williams-25, McGraw Hill Brasil.

[42] Zhu, B.-P., Grigorescu, V., Le, T., Lin, M., Copeland, G., Barone, M., and Turabelidze, G., 2006, "Labor Dystocia and Its Association with Interpregnancy Interval," Am J Obstet Gynecol, **195**(1), pp. 121–128.

[43] Alves De Oliveira, D., 2016, Modeling Damage Process in Pelvic Tissues during Vaginal Delivery.

[44] Lamrani, Y. A., Maâroufi, M., Kamaoui, I., Ammor, H., Houssaini, N. S., and Tizniti, S., 2011, "Neonatal Distal Femoral Epiphyseal Dislocation: An Ultrasound Diagnosis," Journal of Medical Ultrasonics, **38**(4), pp. 221–223.

[45] Andersen, J., Watt, J., Olson, J., and Van Aerde, J., 2006, "Perinatal Brachial Plexus Palsy," Paediatr Child Health, **11**(2), pp. 93–100.

[46] Sorantin, E., Brader, P., and Thimary, F., 2006, "Neonatal Trauma," Eur J Radiol, **60**(2), pp. 199–207.

[47] Eliahou, R., Simanovsky, N., Hiller, N., and Simanovsky, N., 2006, "Fracture-Separation of the Distal Femoral Epiphysis in a Premature Neonate," Journal of ultrasound in medicine, **25**(12), pp. 1603–1605.

[48] Sherr-Lurie, N., Bialik, G. M., Ganel, A., Schindler, A., and Givon, U., 2011, "Fractures of the Humerus in the Neonatal Period," IMAJ-Israel Medical Association Journal, **13**(6), p. 363.

[49] Hoyte, L., Damaser, M. S., Warfield, S. K., Chukkapalli, G., Majumdar, A., Choi, D. J., Trivedi, A., and Krysl, P., 2008, "Quantity and Distribution of Levator Ani Stretch during Simulated Vaginal Childbirth," Am J Obstet Gynecol, **199**(2), pp. 198.e1-198.e5.

[50] Parente, M. P. L., Natal Jorge, R. M., Mascarenhas, T., Fernandes, A. A., and Martins, J. A. C., 2009, "The Influence of the Material Properties on the Biomechanical Behavior of the Pelvic Floor Muscles during Vaginal Delivery," J Biomech, **42**(9), pp. 1301–1306.

[51] Lepage, J., Jayyosi, C., Lecomte-Grosbras, P., Brieu, M., Duriez, C., Cosson, M., and Rubod, C., 2015, "Biomechanical Pregnant Pelvic System Model and Numerical Simulation of Childbirth: Impact of Delivery on the Uterosacral Ligaments, Preliminary Results," Int Urogynecol J Pelvic Floor Dysfunct, **26**(4), pp. 497–504.

[52] Xuan, R., Yang, M., Gao, Y., Ren, S., Li, J., Yang, Z., Song, Y., Huang, X. H., Teo, E. C., Zhu, J., and Gu, Y., 2021, "A Simulation Analysis of Maternal Pelvic Floor Muscle," Int J Environ Res Public Health, **18**(20).

[53] Behr, M., Thollon, L., and Dramard, B. P., 2011, "A Pregnant Woman Model to Study Injury Mechanisms in Car Crashes," (May 2011).

[54] Sharp, G. C., Saunders, P. T. K., and Norman, J. E., 2013, "Computer Models to Study Uterine Activation at Labour," Mol Hum Reprod, **19**(11), pp. 711–717.

[55] Lepage, J., Jayyosi, C., Lecomte-Grosbras, P., Brieu, M., Duriez, C., Cosson, M., and Rubod, C., 2015, "Biomechanical Pregnant Pelvic System Model and Numerical Simulation of Childbirth: Impact of Delivery on the Uterosacral Ligaments, Preliminary Results," Int Urogynecol J Pelvic Floor Dysfunct, **26**(4), pp. 497–504.

[56] Zara, F., and Dupuis, O., 2017, "Uterus – Biomechanical Modeling of Uterus. Application to a Childbirth Simulation," Biomechanics of Living Organs: Hyperelastic Constitutive Laws for Finite Element Modeling, pp. 325–346.

[57] Aspinall, V., Cappello, M., and Phillips, C., 2020, Muscular System., CABI.

[58] Zatsiorsky, V. M., and Prilutsky, B. I., 2012, Biomechanics of Skeletal Muscles, Human Kinetics.

[59] Ripa, R., George, T., and Sattar, Y., 2021, "Physiology, Cardiac Muscle," StatPearls [Internet].

[60] Buttin, R., Zara, F., Shariat, B., Redarce, T., Buttin, R., Zara, F., Shariat, B., Redarce, T., Biomechanical, G. G., Buttin, R., Zara, F., Shariat, B., Redarce, T., and Grang, G., 2017, "Biomechanical Simulation of the Fetal Descent without Imposed Theoretical Trajectory To Cite This Version : HAL Id : Hal-00841386."

[61] Yochum, M., Laforêt, J., and Marque, C., 2016, "An Electro-Mechanical Multiscale Model of Uterine Pregnancy Contraction," Comput Biol Med, **77**(February 2018), pp. 182–194.

[62] Xu, Y., Liu, H., Hao, D., Taggart, M., and Zheng, D., 2020, "Uterus Modeling from Cell to Organ Level: Towards Better Understanding of Physiological Basis of Uterine Activity," IEEE Rev Biomed Eng.

[63] Lin, Y., Zhang, M., La Rosa, P. S., Wilson, J. D., and Nehorai, A., 2019, "Electro-Mechanical Ionic Channel Modeling for Uterine Contractions and Oxytocin Effect during Pregnancy," Sensors, **19**(22), p. 4898.

[64] Stålhand, J., Klarbring, A., and Holzapfel, G. A., 2011, "A Mechanochemical 3D Continuum Model for Smooth Muscle Contraction under Finite Strains," J Theor Biol, **268**(1), pp. 120–130.

[65] Liu, T., 2014, "A Constitutive Model for Cytoskeletal Contractility of Smooth Muscle Cells," Proceedings of the Royal Society A: Mathematical, Physical and Engineering Sciences, **470**(2164).

[66] Murtada, S. Il, Kroon, M., and Holzapfel, G. A., 2010, "A Calcium-Driven Mechanochemical Model for Prediction of Force Generation in Smooth Muscle," Biomech Model Mechanobiol, **9**(6), pp. 749–762.

[67] Cochran, A. L., and Gao, Y., 2015, "A Model and Simulation of Uterine Contractions," Mathematics and Mechanics of Solids, **20**(5), pp. 540–564.

[68] Yochum, M., Laforet, J., and Marque, C., 2016, "An Electro-Mechanical Multiscale Model of Uterine Pregnancy Contraction," Comput Biol Med, **77**, pp. 182–194.

[69] Hill, A. V., 1938, "The Heat of Shortening and the Dynamic Constants of Muscle," Proceedings of the Royal Society of London. Series B-Biological Sciences, **126**(843), pp. 136–195.

[70] Winters, J. M., and Stark, L., 1988, ESTIMATED MECHANICAL PROPERTIES OF SYNERGISTIC MUSCLES INVOLVED IN MOVEMENTS OF A VARIETY OF HUMAN JOINTS.

[71] Mo, F., Li, F., Behr, M., Xiao, Z., Zhang, G., and Du, X., 2018, "A Lower Limb-Pelvis Finite Element Model with 3D Active Muscles," Ann Biomed Eng, **46**(1), pp. 86–96.

[72] Hedenstierna, S., and Halldin, P., 2008, "How Does a Three-Dimensional Continuum Muscle Model Affect the Kinematics and Muscle Strains of a Finite Element Neck Model Compared to a Discrete Muscle Model in Rear-End, Frontal, and Lateral Impacts," Spine (Phila Pa 1976), **33**(8), pp. 236–245.

[73] Iwamoto, M., Nakahira, Y., Kimpara, H., and Sugiyama, T., 2009, "Development of a Human FE Model with 3-D Geometry of Muscles and Lateral Impact Analysis for the Arm with Muscle Activity," SAE Technical Papers, **4970**.

[74] Bates, J. H. T., and Lauzon, A.-M., 1912, "Parenchymal Tethering, Airway Wall Stiffness, and the Dynamics of Bronchoconstriction," J Appl Physiol, **102**.

[75] Murphy, R. A., 1988, "Muscle Cells of Hollow Organs," Physiology, **3**(3), pp. 124–128.

[76] Östh, J., 2014, Muscle Responses of Car Occupants: Numerical Modeling and Volunteer Experiments under Pre-Crash Braking Conditions, Chalmers Tekniska Hogskola (Sweden).

[77] Kearney, S. P., Khan, A., Dai, Z., and Royston, T. J., 2015, "Dynamic Viscoelastic Models of Human Skin Using Optical Elastography," Phys Med Biol, **60**(17), p. 6975.

[78] Pearsall, G. W., and Roberts, V. L., 1978, "Passive Mechanical Properties of Uterine Muscle (Myometrium) Tested in Vitro," J Biomech, **11**(4).

[79] Seow, C. Y., and Stephens, N. L., Changes of Tracheal Smooth Muscle Stiffness during an Isotonic Contraction.

[80] Li, F., Li, H., Hu, W., Su, S., and Wang, B., 2016, "SIMULATION of MUSCLE ACTIVATION with COUPLED NONLINEAR FE MODELS," J Mech Med Biol, **16**(6).

[81] Codd, S. L., Lambert, R. K., Alley, M. R., and Pack, R. J., 1994, "Tensile Stiffness of Ovine Tracheal Wall," J Appl Physiol, **76**(6), pp. 2627–2635.

[82] Lechosa Urquijo, E., Blaya Haro, F., D'Amato, R., and Juanes Méndez, J. A., 2020, "Finite Element Model of an Elbow under Load, Muscle Effort Analysis When Modeled Using 1D Rod Element," Eighth International Conference on Technological Ecosystems for Enhancing Multiculturality, pp. 475–482.

[83] Dao, T. T., and Tho, M. C. H. B., 2018, "A Systematic Review of Continuum Modeling of Skeletal Muscles: Current Trends, Limitations, and Recommendations," Appl Bionics Biomech, **2018**.

[84] Kerckhoffs, R. C. P., Healy, S. N., Usyk, T. P., and McCULLOCH, A. D., 2006, "Computational Methods for Cardiac Electromechanics," Proceedings of the IEEE, **94**(4), pp. 769–783.

[85] Fang, S., McLean, J., Shi, L., Vink, J. S. Y., Hendon, C. P., and Myers, K. M., 2021, "Anisotropic Mechanical Properties of the Human Uterus Measured by Spherical Indentation," Ann Biomed Eng, **49**(8), pp. 1923–1942.

[86] Li, Y., Fortner, L., and Kong, F., 2019, "Development of a Gastric Simulation Model (GSM) Incorporating Gastric Geometry and Peristalsis for Food Digestion Study," Food Research International, **125**, p. 108598.

[87] Nikas, G., 1999, "Cell-Surface Morphological Events Relevant to Human Implantation," Human Reproduction, **14**(suppl_2), pp. 37–44.

[88] Yosibash, Z., and Priel, E., 2012, "Artery Active Mechanical Response: High Order Finite Element Implementation and Investigation," Comput Methods Appl Mech Eng, **237**, pp. 51–66.

[89] Buttin, R., Zara, F., Shariat, B., and Redarce, T., 2009, "A Biomechanical Model of the Female Reproductive System and the Fetus for the Realization of a Childbirth Virtual Simulator," Proceedings of the 31st Annual International Conference of the IEEE Engineering in Medicine and Biology Society: Engineering the Future of Biomedicine, EMBC 2009, pp. 5263–5266.

[90] Yao, W., Gan, Y., Myers, K. M., Vink, J. Y., Wapner, R. J., and Hendon, C. P., 2016, "Collagen Fiber Orientation and Dispersion in the Upper Cervix of Non-Pregnant and Pregnant Women," PLoS One, **11**(11), p. e0166709.

[91] Niederer, P., Weiss, S., Caduff, R., Bajka, M., Szekély, G., and Harders, M., 2009, "Uterus Models for Use in Virtual Reality Hysteroscopy Simulators," European Journal of Obstetrics and Gynecology and Reproductive Biology, **144**(SUPPL 1).

[92] Dubrauszky, V., Schwalm, H., and Fleischer, M., 1971, "The Fibre System of Connective Tissue in the Childbearing Age, Menopause, and Pregnancy," Arch Gynakol, **210**(3), pp. 276–292.

[93] Pino, J. H., 2017, "Arrangement of Muscle Fibers in the Myometrium of the Human Uterus: A Mesoscopic Study," MOJ Anat Physiol, **4**(2).

[94] Fiocchi, F., Nocetti, L., Siopis, E., Currà, S., Costi, T., Ligabue, G., and Torricelli, P., 2012, "In Vivo 3T MR Diffusion Tensor Imaging for Detection of the Fibre Architecture of the Human Uterus: A Feasibility and Quantitative Study," British Journal of Radiology, **85**(1019).

[95] Fang, S., McLean, J., Shi, L., Vink, J. S. Y., Hendon, C. P., and Myers, K. M., 2021, "Anisotropic Mechanical Properties of the Human Uterus Measured by Spherical Indentation," Ann Biomed Eng, **49**(8), pp. 1923–1942.

[96] Vila Pouca, M. C. P., Ferreira, J. P. S., Oliveira, D. A., Parente, M. P. L., Mascarenhas, M. T., and Natal Jorge, R. M., 2019, "Simulation of the Uterine Contractions and Foetus Expulsion Using a Chemo-Mechanical Constitutive Model," Biomech Model Mechanobiol, **18**(3), pp. 829–843.

[97] Zhang, W., and Chen, J., 2020, "Diffusion Tensor Imaging (DTI) of the Cesarean-Scarred Uterus in Vivo at 3T: Comparison Study of DTI Parameters Between Nonpregnant and Pregnant Cases," Journal of Magnetic Resonance Imaging, **51**(1), pp. 124–130.

[98] He, Y., Ding, N., Li, Y., Li, Z., Xiang, Y., Jin, Z., and Xue, H., 2015, "3-T Diffusion Tensor Imaging (DTI) of Normal Uterus in Young and Middle-Aged Females during the Menstrual Cycle: Evaluation of the Cyclic Changes of Fractional Anisotropy (FA) and Apparent Diffusion Coefficient (ADC) Values," British Journal of Radiology, **88**(1049).

[99] Smith, R., Imtiaz, M., Banney, D., Paul, J. W., and Young, R. C., 2015, "Why the Heart Is like an Orchestra and the Uterus Is like a Soccer Crowd," Am J Obstet Gynecol, **213**(2), pp. 181–185.

[100] Steer, P. J., Little, D. J., Lewis, N. L., Kelly, M. C. M. E., and Beard, R. W., 1975, "UTERINE ACTIVITY IN LNDUCED LABOUR," BJOG, **82**(6), pp. 433–441.

[101] Yao, W., Yoshida, K., Fernandez, M., Vink, J., Wapner, R. J., Ananth, C. V., Oyen, M. L., and Myers, K. M., 2014, "Measuring the Compressive Viscoelastic Mechanical Properties of Human Cervical Tissue Using Indentation," J Mech Behav Biomed Mater, **34**, pp. 18–26.

[102] Fodera, D. M., Russell, S. R., Lund-Jackson, J. L., Fang, S., Chen, X., Vink, J.-S. Y., Oyen, M. L., and Myers, K. M., 2023, "Material Properties of Nonpregnant and Pregnant Human Uterine Layers," J Mech Behav Biomed Mater, p. 106348.

[103] Myers, K. M., Socrate, S., Paskaleva, A., and House, M., 2010, "A Study of the Anisotropy and Tension/Compression Behavior of Human Cervical Tissue," J Biomech Eng, **132**(2).

[104] Shi, L., and Myers, K., 2023, "A Finite Porous-Viscoelastic Model Capturing Mechanical Behavior of Human Cervix under Multi-Step Spherical Indentation."

[105] Shi, L., Hu, L., Lee, N., Fang, S., and Myers, K., 2022, "Three-Dimensional Anisotropic Hyperelastic Constitutive Model Describing the Mechanical Response of Human and Mouse Cervix," Acta Biomater, **150**, pp. 277–294.

[106] Westervelt, A. R., Fernandez, M., House, M., Vink, J., Nhan-Chang, C. L., Wapner, R., and Myers, K. M., 2017, “A Parameterized Ultrasound-Based Finite Element Analysis of the Mechanical Environment of Pregnancy,” J Biomech Eng, **139**(5).

[107] Westervelt, A. R., and Myers, K. M., 2017, “Computer Modeling Tools to Understand the Causes of Preterm Birth,” Semin Perinatol, **41**(8), pp. 485–492.

[108] Scott, A. K., Louwagie, E. M., Myers, K. M., and Oyen, M. L., “Biomechanical Modeling of Cesarean Section Scars and Scar Defects.”

[109] Koh, C. T., and Oyen, M. L., 2015, “Toughening in Electrospun Fibrous Scaffolds,” APL Mater, **3**(1).

[110] Clark, A. R., Yoshida, K., and Oyen, M. L., 2022, “Computational Modeling in Pregnancy Biomechanics Research,” J Mech Behav Biomed Mater, **128**.

[111] Parente, M. P. L., Natal Jorge, R. M., Mascarenhas, T., Fernandes, A. A., and Martins, J. A. C., 2009, “The Influence of the Material Properties on the Biomechanical Behavior of the Pelvic Floor Muscles during Vaginal Delivery,” J Biomech, **42**(9), pp. 1301–1306.

[112] Yochum, M., Laforêt, J., and Marque, C., 2016, “An Electro-Mechanical Multiscale Model of Uterine Pregnancy Contraction,” Comput Biol Med, **77**, pp. 182–194.

[113] Bamberg, C., Rademacher, G., Güttler, F., Teichgräber, U., Cremer, M., Bührer, C., Spies, C., Hinkson, L., Henrich, W., and Kalache, K. D., 2012, “Human Birth Observed in Real-Time Open Magnetic Resonance Imaging,” Am J Obstet Gynecol, **206**(6), pp. 505-e1.

[114] Das Bindegewebsfasersystem Des Myometrium Wahrend Der Geschlechtsreife, Der Menopause Und Der Gravidit~it.

[115] Diomidova, V. N., and Zakharova, O. V., 2017, “ELASTOGRAPHY AND SHEAR WAVE ELASTOMETRY-BASED VALUES OF YOUNG’S MODULUS OF ENDOMETRIUM IN HEALTHY WOMEN OF REPRODUCTIVE AGE,” RAD Association Journal, **2**(3).

[116] Dubrauszky, V., Schwalm, H., and Fleischer, M., 1971, “The Fibre System of Connective Tissue in the Childbearing Age, Menopause, and Pregnancy,” Arch Gynakol, **210**(3), pp. 276–292.

[117] Östh, J., Brolin, K., and Bråse, D., 2015, “A Human Body Model With Active Muscles for Simulation of Pretensioned Restraints in Autonomous Braking Interventions,” Traffic Inj Prev, **16**(3), pp. 304–313.

[118] Abalos, E., Oladapo, O. T., Chamillard, M., Díaz, V., Pasquale, J., Bonet, M., Souza, J. P., and Gülmezoglu, A. M., 2018, “Duration of Spontaneous Labour in ‘Low-Risk’ Women with ‘Normal’ Perinatal Outcomes: A Systematic Review,” European Journal of Obstetrics and Gynecology and Reproductive Biology, **223**, pp. 123–132.

[119]Acker, D. B., Sachs, B. P., and Friedman, E. A., 1985, “Risk Factors for Shoulder Dystocia.,” Obstetrics and gynecology, **66**(6), pp. 762–768.

[120] Doumouchtsis, S. K., and Arulkumaran, S., 2009, “Are All Brachial Plexus Injuries Caused by Shoulder Dystocia?,” Obstet Gynecol Surv, **64**(9), pp. 615–623.

[121] Mitanchez, D., 2010, "Foetal and Neonatal Complications in Gestational Diabetes: Perinatal Mortality, Congenital Malformations, Macrosomia, Shoulder Dystocia, Birth Injuries, Neonatal Complications.," Diabetes Metab, **36**(6 Pt 2), pp. 617–627.

[122] Lien, K.-C., Morgan, D. M., Delancey, J. O. L., and Ashton-Miller, J. A., 2005, "Pudendal Nerve Stretch during Vaginal Birth: A 3D Computer Simulation," Am J Obstet Gynecol, **192**(5), pp. 1669–1676.

[123] Olsen, A. L., Smith, V. J., Bergstrom, J. O., Colling, J. C., and Clark, A. L., 1997, "Epidemiology of Surgically Managed Pelvic Organ Prolapse and Urinary Incontinence," Obstetrics & Gynecology, **89**(4), pp. 501–506.

[124] Dimpfl, T., Jaeger, C. H., Mueller-Felber, W., Anthuber, C., Hirsch, A., Brandmaier, R., and Schuessler, B., 1998, "Myogenic Changes of the Levator Ani Muscle in Premenopausal Women: The Impact of Vaginal Delivery and Age," Neurourology and Urodynamics: Official Journal of the International Continence Society, **17**(3), pp. 197–205.

[125] Parente, M. P. L., Jorge, R. M. N., Mascarenhas, T., Fernandes, A. A., and Martins, J. A. C., 2009, "The Influence of the Material Properties on the Biomechanical Behavior of the Pelvic Floor Muscles during Vaginal Delivery," J Biomech, **42**(9), pp. 1301–1306.

[126] Chen, S., and Grimm, M. J., 2020, "Childbirth Computational Models: Characteristics and Applications," J Biomech Eng, (4196747), pp. 1–62.

[127] Teixeira Da Silva, M. E., 2017, FACULDADE DE ENGENHARIA DA UNIVERSIDADE DO PORTO Evaluating the Mechanical Properties of Biological Soft Tissues Using Inverse Methods: Application to the Pelvic Floor Muscles.

[128] Silva, M. E. T., Oliveira, D. A., Roza, T. H., Brandão, S., Parente, M. P. L., Mascarenhas, T., and Natal Jorge, R. M., 2015, "Study on the Influence of the Fetus Head Molding on the Biomechanical Behavior of the Pelvic Floor Muscles, during Vaginal Delivery," J Biomech, **48**(9), pp. 1600–1605.

[129] Routzong, M. R., Moalli, P. A., Rostaminia, G., and Abramowitch, S. D., 2023, "Morphological Variation in the Pelvic Floor Muscle Complex of Nulliparous, Pregnant, and Parous Women," Ann Biomed Eng, pp. 1–10.

[130] Chen, S., Routzong, M. R., Abramowitch, S. D., and Grimm, M. J., 2023, "A Computational Procedure to Derive the Curve of Carus for Childbirth Computational Modeling," J Biomech Eng, **145**(1), p. 011002.

[131] Buttin, R., Zara, F., Shariat, B., Redarce, T., and Grangé, G., 2013, "Biomechanical Simulation of the Fetal Descent without Imposed Theoretical Trajectory," Comput Methods Programs Biomed, **111**(2), pp. 389–401.

[132] Ghi, T., Farina, A., Pedrazzi, A., Rizzo, N., Pelusi, G., and Pilu, G., 2009, "Diagnosis of Station and Rotation of the Fetal Head in the Second Stage of Labor with Intrapartum Translabial Ultrasound," Ultrasound in Obstetrics and Gynecology, **33**(3), pp. 331–336.

[133] Elvander, C., Högberg, U., and Ekeus, C., 2012, "The Influence of Fetal Head Circumference on Labor Outcome: A Population-based Register Study," Acta Obstet Gynecol Scand, **91**(4), pp. 470–475.

[134] Da Silva, M. E. T., Parente, M. P. L., and Jorge, R. M. N., 2013, “Biomechanical Study of a Fetus during a Vaginal Delivery,” 3rd Portuguese Bioengineering Meeting, ENBENG 2013 - Book of Proceedings.

[135] Li, X., Kruger, J. A., Chung, J.-H., Nash, M. P., and Nielsen, P. M. F., 2008, LNCS 5242 - Modelling Childbirth: Comparing Athlete and Non-Athlete Pelvic Floor Mechanics.

[136] Pavan, P. G., Todros, S., Pachera, P., Pianigiani, S., and Natali, A. N., 2019, “The Effects of the Muscular Contraction on the Abdominal Biomechanics: A Numerical Investigation,” Comput Methods Biomech Biomed Engin, **22**(2), pp. 139–148.

[137] Blanc, F. X., Coirault, C., Salmeron, S., Chemla, D., and Lecarpentier, Y., 2003, “Mechanics and Crossbridge Kinetics of Tracheal Smooth Muscle in Two Inbred Rat Strains,” European Respiratory Journal, **22**(2), pp. 227–234.

[138] Klotz, T., Bleiler, C., and Röhrle, O., 2021, “A Physiology-Guided Classification of Active-Stress and Active-Strain Approaches for Continuum-Mechanical Modeling of Skeletal Muscle Tissue,” Front Physiol, **12**.

[139] Göktepe, S., Menzel, A., and Kuhl, E., 2014, “The Generalized Hill Model: A Kinematic Approach towards Active Muscle Contraction,” J Mech Phys Solids, **72**(1), pp. 20–39.

[140] Smith, R. P., 1984, “A Brief History of Intrauterine Pressure Measurement,” Acta Obstet Gynecol Scand, **63**(129 S), pp. 1–24.

[141] Mandel, W., Singer, M. J., Gudmunson, H. R., Meister, L., and Modern, F., 1991, Use of McRoberts’ Position during Delivery and Increase in Pushing Efficiency.

[142] Allman, A. C. J., Genevier, E. S. G., Johnson, M. R., and Steer, P. J., 1996, “Head-to-Cervix Force: An Important Physiological Variable in Labour. 1. The Temporal Relation between Head-to-Cervix Force and Intrauterine Pressure during Labour,” BJOG, **103**(8), pp. 763–768.

[143] Rempen, A., and Kraus, M., 1991, Measurement of Head Compression during Labor: Preliminary Results.

[144] Hua, C., Fang, C., and Cheng, J., 2011, “Simulation of Fluid-Solid Interaction on Water Ditching of an Airplane by ALE Method,” Journal of Hydrodynamics, **23**(5), pp. 637–642.

[145] Ma, J., and Usman, M., 8 Th International LS-DYNA Users Conference Fluid/Structure Modeling of Fuel Sloshing Phenomena Considering Solid-Fluid Interaction.

[146] Truong, D. D., Jang, B. S., Janson, C. E., Ringsberg, J. W., Yamada, Y., Takamoto, K., Kawamura, Y., and Ju, H. B., 2021, “Benchmark Study on Slamming Response of Flat-Stiffened Plates Considering Fluid-Structure Interaction,” Marine Structures, **79**.

[147] Song, M., Ma, J., and Huang, Y., 2017, “Fluid-Structure Interaction Analysis of Ship-Ship Collisions,” Marine Structures, **55**, pp. 121–136.

[148] Orozco, V., Magee, R., Balasubramanian, S., and Singh, A., 2021, “A Systematic Review of the Tensile Biomechanical Properties of the Neonatal Brachial Plexus,” J Biomech Eng, **143**(11).

[149] Singh, A., 2019, “Available Computational and Physical Models to Understand the Mechanisms of Neonatal Brachial Plexus Injury During Shoulder Dystocia,” Open Access J Neurol Neurosurg, **9**(4).

[150] Gonik, B., Zhang, N., and Grimm, M. J., 2003, “Prediction of Brachial Plexus Stretching during Shoulder Dystocia Using a Computer Simulation Model,” Am J Obstet Gynecol, **189**(4), pp. 1168–1172.

[151] Grimm, M. J., Costello, R. E., and Gonik, B., 2010, “Effect of Clinician-Applied Maneuvers on Brachial Plexus Stretch during a Shoulder Dystocia Event: Investigation Using a Computer Simulation Model,” Am J Obstet Gynecol, **203**(4), pp. 339.e1-339.e5.

[152] Gherman, R. B., Chauhan, S. P., Clark, S. L., Gonik, B., Grimm, M. J., Grobman, W. A., Ouzounian, J. G., Yang, L. J., Goldsmith, J. P., and Senikas, V., 2014, “Neonatal Brachial Plexus Palsy,” Obstetrics and gynecology, **123**(4), pp. 902–904.

[153] Moolgaoker, A. S., AHAMED, S. O. S., and PAYNE, P. R., 1979, “A Comparison of Different Methods of Instrumental Delivery Based on Electronic Measurements of Compression and Traction,” Obstetrics & Gynecology, **54**(3), pp. 299–309.

[154] Allen, R., Sorab, J., and Gonik, B., 1991, “Risk Factors for Shoulder Dystocia: An Engineering Study of Clinician-Applied Forces.,” Obstetrics and gynecology, **77**(3), pp. 352–355.

[155] Reynolds, S. R. M., Hellman, L. M., and Bruns, P., 1948, “Patterns of Uterine Contractility in Women during Pregnancy,” Obstet Gynecol Surv, **3**(5), pp. 629–646.

[156] Mikkelsen, E., Johansen, P., Fuglsang-Frederiksen, A., and Uldbjerg, N., 2013, “Electrohysterography of Labor Contractions: Propagation Velocity and Direction,” Acta Obstet Gynecol Scand, **92**(9), pp. 1070–1078.

[157] Lammers, W. J. E. P., 2013, “The Electrical Activities of the Uterus during Pregnancy,” Reproductive Sciences, **20**(2), pp. 182–189.

[158] Buhimschi, C. S., 2009, “Spatiotemporal Electromyography during Human Labor to Monitor Propagation of the Uterine Contraction Wave and Diagnose Dystocia,” Am J Obstet Gynecol, **200**(1), pp. 1–3.